T H E   U N I V E R S I T Y   O F   M I C H I G A N

COLLEGE OF LITERATURE, SCIENCE, AND THE ARTS

Department of Physics

Technical Report 032150-1-T

A CRYOGENIC SHOCK TUBE:

LOW TEMPERATURE SHOCK WAVES IN MOLECULAR HYDROGEN

Marvel John Yoder

Otto Laporte, Project Supervisor

ORA Project 032150

June 1971

ACKNOWLEDGEMENTS

I am grateful for the guidance of Professor Otto Laporte. I appreciated his bold and innovative suggestions and his patience in allowing me to persue my special interests in rotational relaxation.

I would like to thank Professor T. Michael Sanders for assuming chairmanship of my doctoral committee after Professor Laporte's untimely death. The evaluation and criticism by Professor Edward Lady, Professor T. Michael Sanders, and Dr. Stephan Whitmore of several preliminary shock tube designs was very helpful. I would also like to thank Professor P. C. T. de Boer of Cornell for a valuable discussion with him of some of the experimental results.

The friendship of my colleague Dr. Yong Wook Kim was appreciated. His suggestions and criticisms concerning the cryogenic shock tube design and experimental procedures were very helpful. The assistance of John Brimm, Michael Macksey, Graham Smith, Jeff Cereni, and James Dell in carrying out this experiment and evaluating the data is gratefully acknowledged.

TABLE OF CONTENTS

LIST OF TABLES

LIST OF FIGURES

ABSTRACT

A cryogenic shock tube has been constructed for the purpose of producing shock waves with initial temperatures as low as 30 $^{\circ}$K. It consists of a four foot long stainless steel driver section and an eight foot long aluminum expansion section which are suspended inside a horizontal cylindrical dewar using nylon rods. The sections are cooled with liquid nitrogen or liquid helium. This shock tube has been applied to the study of low temperature shock waves in molecular hydrogen and parahydrogen.

The Rankine-Hugoniot shock equation, which determines the density ratio across the shock as a function of pressure ratio or shock speed, behaves nonclassically for normal hydrogen and parahydrogen. This is due to the change in the number of degrees of freedom across the shock caused by the excitation of the rotational energy states. The predicted Rankine-Hugoniot curves have been experimentally measured and confirmed. This was done by simultaneous measurement of the shock speed and the density ratio; the latter by means of a Mach-Zehnder interferometer with a laser light source. Pressure measurements also were made using a quartz piezoelectric transducer.

Rotational relaxation times have been measured for normal hydrogen and parahydrogen. This has been accomplished using a high sensitivity schlieren optical system with a laser light source and a photomultiplier recording system. Laboratory relaxation times of order 0.1 microseconds are measured with a spatial resolution of 0.1 millimeters. Measurements are made over a temperature range of 140 $^{\circ}$K to 450 $^{\circ}$K. Relaxation times are in agreement with results obtained by other methods for those values of temperature where comparison is possible.

CHAPTER I

INTRODUCTION

1. Elementary Shock Theory

The shock tube in its basic form consists of a tube divided into two parts by a breakable diaphragm (see Fig. 1a). A test gas at some low pressure, usually 1.0 to 100 torr, is contained in one of the chambers. This chamber is called the expansion section. The other chamber is called the driver section and is filled with gas to a high pressure, usually 100 to 2000 psi, until the scored aluminum diaphragm between the two chambers bursts. The high pressure gas expands rapidly into the expansion section. The interface between the two gases behaves as if there were a rigid massless piston constantly separating them but being free to move down the tube. This fictitious piston simplifies the understanding of shock wave formation without leading to any physically incorrect conclusions. The "piston" compresses and pushes the expansion section gases ahead of it. It moves at a constant supersonic speed. The gas in a region near the "piston" must come to rest with respect to it. The pressure and temperature of this gas are uniform due to the fact that all the gas has undergone the same type of compression process in reaching its final state. Far ahead of the "piston" the gas has not had time to receive information of these sudden events and thus remains in its initial state (P_o, T_o). The pressure profile in the

Figure 1. Pressure profiles in the shock tube at various times

transition region between these two uniform states can best
be deduced by first assuming that the transition is gradual
and stationary as shown in Fig. 1b. It is helpful to choose
a system of reference that is at rest with respect to this
transition region. Any pressure increment, ΔP_i, in a region,
Δx_i, at the position x_i along the shock tube is, of course,
propagated at the local speed of sound. This speed is
proportional to the square root of the absolute temperature.
Thus a disturbance is propagated faster in a region where
the gas is at a higher temperature. Now consider two points,
x_3 and x_4, within the assumed transition region. Since the
gas at x_3 has been compressed more than that at x_4 it is
hotter and the disturbance ΔP_3 is propagated faster than
the disturbance ΔP_4. Therefore the proposed form of the
transition region is not gradual and stationary but tends to
steepen. This steepening must continue until a step discon-
tinuity is formed as shown in Fig. 1c. This discontinuity
is called a shock wave. A more detailed and complete
description is given by Laporte[1].

Behind the "piston", in the gas which was originally
in the driver section, there are again two regions of
uniform conditions - one near the "piston" and one near
the end wall of the driver. In this case, however, there
is no discontinuity in the transition region. An expansion
wave travels into the driver section. The head of this
expansion wave moves at the local speed of sound. The
point at which the pressure in the transition region becomes
constant and equal to the pressure of the shocked gas is

called the expansion foot. It moves either up or downstream
depending on whether the driver gas has a higher or a lower
sound speed than the expansion section gas. In either case
the transition becomes more and more gradual - very unlike
the shock wave.

At this point in the discussion the fiction of the
rigid piston is no longer necessary for understanding the
shock tube flows. If the "piston" is now mentally removed
there is no reason to believe that the shock tube flow will
be affected, since there are no pressure gradients across
the interface. To be sure, there is diffusion of one gas
into the other, but this is an extremely slow process on the
scale of the shock wave duration of five to ten milliseconds.
The discussion is complete except for a rigorous justification
of the origonal piston assumption. The initial flows are
described more fully in many textbooks on hydrodynamics[2].

To describe the flow which occurs after the shock
reaches the end wall of the shock tube, it is helpful to
change to a frame of reference which is at rest with respect
to the gas that has already passed through the incident shock.
At the instant that the shock strikes the end wall the events
are viewed from the new reference frame. In this frame the
end wall behaves as if it were a real piston advancing with
supersonic speed into a gas at rest. This is the same
situation as described previously. Thus a shock wave must
be formed at the endwall and travel into the already shocked
gas. This is called the reflected shock wave.

Yet another reflection occurs when the reflected shock reaches the interface (sometimes called the contact surface) and again when this shock reaches the end wall once more... etc. A three dimensional unified depiction of these events can be seen in figure 2.

2. The Shock Tube as a Scientific Instrument

The most obvious application of the shock tube is that of generating supersonic flows. If a model is suspended in the tube it is possible to observe its interaction with the shock. After the shock passes over the model the behavior of the supersonic flow around the model can be studied. This use of the shock tube was initiated by Geiger and Mautz[4]. Many such experiments have been carried out in a number of laboratories.

Shock waves are of great interest in spectroscopy. If driver gases having high sound speeds are used (e.g. hydrogen or helium) and expansion section gases having low sound speeds (e.g. argon, air, xenon) are used, very strong shocks can be generated.[5,6] Mach numbers of twenty or more are not unusual. This results in very large pressure ratios across the shock of three hundred or more. This large compression causes a substantial heating of the gas. The temperature

Figure 2. x-t-P diagram[3]

of the singly shocked gas can reach 10 000 $^{\circ}$K or more. When
this gas is again compressed by the reflected shock the
temperature is again increased reaching 20 000 $^{\circ}$K or more.
The cylinder of shock-heated gas contained between the shock
front and the interface is homogeneous and there are usually
no cool boundary layers to absorb the emmitted light. In
both of these features the shock tube is far superior to other
widely used spectroscopic sources such as flames or arcs.

The shock-heated gas is in a state of local thermodynamic
equilibrium (L.T.E.) in the sense that there is a Boltzmann
distribution over the excited atomic and molecular states
and an equipartition of energy among the degrees of freedom
of the system. This important property allows one to deter-
mine the relative populations of every excited energy state
at each temperature. The temperature and density of emmitters
can be calculated from the initial conditions by use of the
shock equations. This allows the absolute transition prob-
abilities between states to be deduced from measurements of
spectral line intensities. The shock tube provides the most
accurate method available for the determination of transition
probabilities (gf values) for optical frequencies.[7-9]

Behind very strong shocks the equilibrium conditions
may be such that the gas is highly ionized. Electron densities
approaching 10^{18} electrons/cm^3 are attainable with conven-
tional pressure-driven shock tubes. In these highly ionized
gases each energy state is subject to Stark splitting due to
the microscopic electric fields of the ions and electrons.

This results in a broadening of the spectral lines. Spectral line broadening has been measured for a number of lines.[10-12]

Another area of interest in shock tube applications is the study of the approach to the equilibrium state. The shock is a step discontinuity in the sense that a Maxwellian distribution of velocities is attained within several mean free paths of the initial disturbance. However, often there are other degrees of freedom of the system -- rotational, vibrational, and electronic. Additionally, complete thermodynamic equilibrium may require the molecules to dissociate or the atoms to ionize. All these processes are slow compared to the shock process. The monitoring of the changes in the thermodynamic state behind the shock provides a method of studying the time necessary for the attainment of equilibrium for these internal degrees of freedom (see Fig. 3). This approach to equilibrium occurs within a thermal bath at a known translational temperature which decreases as the internal degrees of freedom are excited. The shock tube thus provides an excellent method of studying molecular collision processes.[13]

3. Outline of the Experiment and its Goals

The internal energy structure of a gas makes itself known through its effects on the pressure, density, and temperature ratios across the shock. For example, these
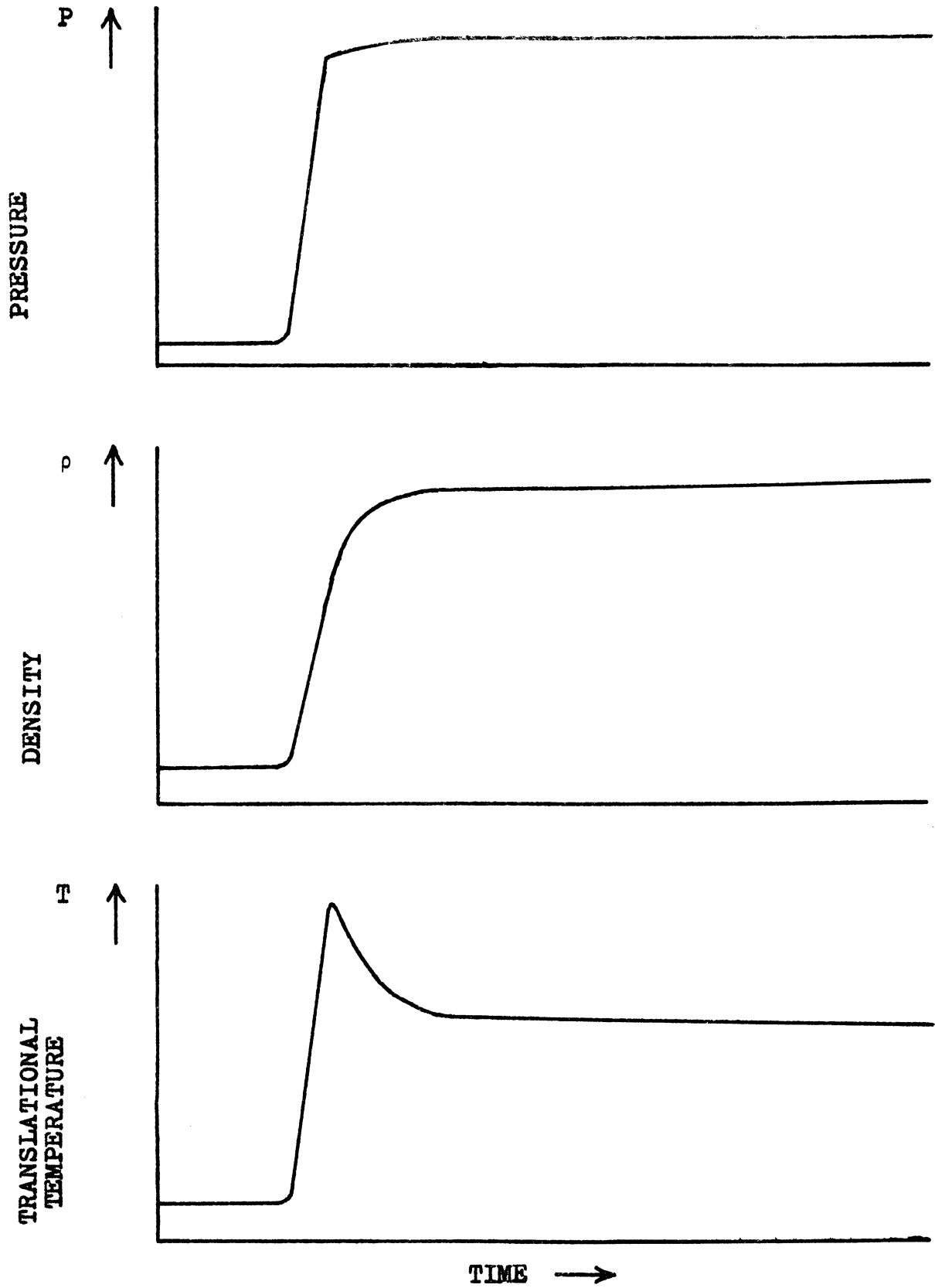
Figure 3. Shock profiles in a relaxing gas at a
fixed position x along the shock tube axis

ratios for a classical monatomic gas are quite different
from those for a classical diatomic gas. In this experiment
the effects of the rotational degrees of freedom on these
ratios are studied for hydrogen at initial temperatures of
$30^{\circ}K$ to $100^{\circ}K$. At room temperature and above, many rotational
states are populated and hydrogen behaves as a classical
diatomic gas. At lower temperatures, however, the spacing
of the rotational energy levels strongly affects its thermo-
dynamic behavior. When the temperature is sufficiently low
that all the molecules reside in their lowest rotational
eigenstates, hydrogen is indistinguishable from a classical
monatomic gas.

Low strength shocks in low temperature hydrogen heat
it very little, and all the molecules remain in the lowest
available rotational states. The gas behaves monatomically.
High strength shocks heat the gas sufficiently that a large
number of rotational states are populated. The density and
pressure ratios across the shock are the same as those for
a diatomic gas. All intermediate variations are possible.
A quantitative calculation of these effects is made in
Chapter II.

For any specific shock velocity the nonclassical behavior
of hydrogen shows up in the pressure, density, and temperature
ratios attained across the shock. Experiments are carried
out to test the predictions of the shock calculations. Final
densities and pressures are measured directly using a Mach-
Zehnder interferometer and a quartz piezoelectric pressure
transducer. These methods are described in Chapter III and

the results are given in Chapter IV.

Although relaxation times have been extensively measured for shocks with dissociational, ionizational, and vibrational excitation modes, very little information is available concerning rotational relaxation times. Usually these times are so short that they are indistinguishable from the time necessary to achieve a Maxwellian distribution of the particle velocities. This is due to the fact that the separation between adjacent energy levels is usually $\ll kT$, the energy of translation. Only in molecules with very low moments of inertia are the rotational energies sufficiently separated so that their spacing is $\gtrsim kT$, and thus an appreciably long time is necessary for rotational relaxation. Even for the most favorable molecule, hydrogen, these times are still very short and difficult to measure. In this experiment a sensitive schlieren optical system using a laser light source is used to measure very small density gradients, thereby allowing the use of low density test gas. This in turn gives rise to laboratory relaxation times sufficiently long to be observable. The measurement technique is described in Chapter III and the results given in Chapter V.

CHAPTER II

SHOCK CALCULATIONS AND PREDICTIONS

1. Quantitative Hydrodynamic Calculation

In order to calculate the state of the gas behind the shock it is convenient to adopt a reference system that is at rest with respect to the shock front itself. One sees a gas having a density ρ_0 and a pressure P_0, entering the shock front at some velocity, v_0. It leaves the shock front with a different velocity, v_1, density, ρ_1, and pressure, P_1.
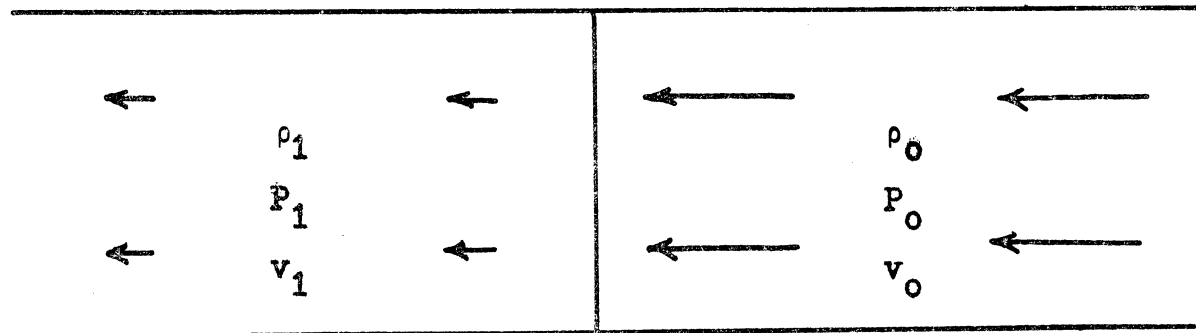
Figure 4. Fluid flows viewed from a reference system which is fixed with respect to the shock

Mass, momentum, and energy must be conserved in the flow across the shock. These are the only physical laws necessary to determine the final state of the gas.

The mass of the gas must be conserved in the flow across the shock, so the application of this first conservation relation yields

$$\begin{matrix}\text{mass flow/second} \\ \text{into the shock}\end{matrix} = \begin{matrix}\text{mass flow/second} \\ \text{out of the shock}\end{matrix}$$

$$\rho_o \, v_o \, A = \rho_o \, v_1 \, A. \tag{1}$$

(A) is the shock tube cross-sectional area.

If a volume of gas is followed as it flows through the shock in unit time, the net change in momentum must be equal to the applied force due to the pressure difference.

$$\text{change in momentum per second} = \text{applied force}$$

$$(\rho_1 v_1 A)v_1 - (\rho_o v_o A)v_o = (P_1 - P_o)A \tag{2}$$

Energy conservation requires that the change in kinetic energy plus the work done by the pressure forces must be equal to the change of the internal energy of the gas flowing through the shock.

$$\begin{matrix}\text{change} \\ \text{in K. E.}\end{matrix} + \begin{matrix}\text{work done by} \\ \text{pressure forces}\end{matrix} = \begin{matrix}\text{change in} \\ \text{internal energy}\end{matrix}$$

$$\begin{aligned}\tfrac{1}{2}(\rho_1 v_1 A)v_1^2 - \tfrac{1}{2}(\rho_o v_o A)v_o^2 + P_1 v_1 A - P_o v_o A = \\ (\rho_1 v_1 A)e_1 - (\rho_o v_o A)e_o\end{aligned} \tag{3}$$

$e(\rho,P)$ is the internal energy per unit mass of the gas.

These three conservation equations can be rearranged into the form

$$\rho_o \, u = \rho_1 \, v_1 \qquad (4)$$

$$\rho_o \, u^2 + P_o = \rho_1 \, v_1^2 + P_1 \qquad (5)$$

$$\tfrac{1}{2} u^2 + P_o/\rho_o + e_o = \tfrac{1}{2} v_1^2 + P_1/\rho_1 + e_1, \qquad (6)$$

where u is identical to v_o and is the shock speed measured in the laboratory coordinate system.

There are three algebraic equations with three unknowns, v_1, ρ_1, and P_1; thus the final state of the gas is calculable provided that the initial state of the gas is known and the shock speed is measured. These are non-linear equations and usually have to be solved numerically. $e(\rho, P)$ must be known before the calculation can be carried out. This function depends on the specific gas under consideration. Its determination is a thermodynamic, not hydrodynamic, task and will be dealt with in Section 3.

2. The Shock as a Thermodynamic Process

v_1 can be eliminated from the conservation equations, yielding

$$\rho_o \, (1 - \rho_o/\rho_1) \, u^2 = P_1 - P_o \qquad (7)$$

$$\tfrac{1}{2} u^2 - \tfrac{1}{2} \rho_o^2/\rho_1^2 + (P_o/\rho_o - P_1/\rho_1) = e_1 - e_o \qquad (8)$$

Elimination of u between these two equations yields

$$\frac{P_1 + P_0}{2} \left[\frac{1}{\rho_0} - \frac{1}{\rho_1} \right] = e_1 - e_0. \tag{9}$$

This is usually called the Rankine-Hugoniot equation. The equation traces the thermodynamic path of a small volume of gas as it undergoes the "shock process". Weak shocks carry the system only a short distance from (P_0, ρ_0) to the new point, (P_1, ρ_1) in (P, ρ) space. Stronger shocks carry the system further and further from its initial state. Thus a curve is traced for the system undergoing this "process". It may be compared to the curves traced out by systems undergoing other well-defined thermodynamic processes, such as adiabatic or isothermal processes.

As an illustration, consider the "shock process" for an ideal gas having a fixed number of degrees of freedom, f.

$$\rho e \doteq E = \frac{\text{internal energy per}}{\text{unit volume of gas}} = \frac{f}{2} nkT \tag{10}$$

where n is the number of molecules per unit volume and k is Boltzmann's constant. The Rankine-Hugoniot equation becomes

$$\frac{P_1 + P_0}{2} \left[\frac{1}{\rho_0} - \frac{1}{\rho_1} \right] = \frac{f}{2} n k \left[\frac{T_1}{\rho_1} - \frac{T_0}{\rho_0} \right]. \tag{11}$$

If the ideal gas equation of state $P = nkT$ is used, one finds

$$\frac{P_1 + P_0}{2} \left[\frac{1}{\rho_0} - \frac{1}{\rho} \right] = \frac{f}{2} \left[\frac{P_1}{\rho_1} - \frac{P_0}{\rho_0} \right]. \tag{12}$$

The preceding equation may be rearranged to yield

Shock Process
$$\frac{\rho_1}{\rho_0} = \frac{(1 + f) P_1/P_0 + 1}{P_1/P_0 + (1 + f)} . \tag{12}$$

The corresponding expressions for adiabatic and isothermal processes are

Adiabatic Process
$$P_0 V_0^\gamma = P_1 V_1^\gamma \quad \text{or} \quad \frac{\rho_1}{\rho_0} = \left[\frac{P_1}{P_0}\right]^{\frac{f+2}{f}} \tag{13}$$

Isothermal Process
$$P_0 V_0 = P_1 V_1 \quad \text{or} \quad \frac{\rho_1}{\rho_0} = \frac{P_1}{P_0} \tag{14}$$

where γ is defined as the quantity $(f+2)/f$.

These equations can be plotted on a (P, ρ) diagram in order to compare these processes. The initial state must first be specified. For each process a whole family of curves is generated by the choice of different initial conditions. It is, however, more instructive to make comparisons by using the universal curve obtained by plotting ρ_1/ρ_0 as a function of P_1/P_0. The curves for all three processes are shown in Fig. 5 for both monatomic and diatomic gases.

The density ratio in a shock process rises very slowly as a function of the pressure ratio. It approaches an asymptotic limit of 4 for an ideal monatomic gas and 6 for
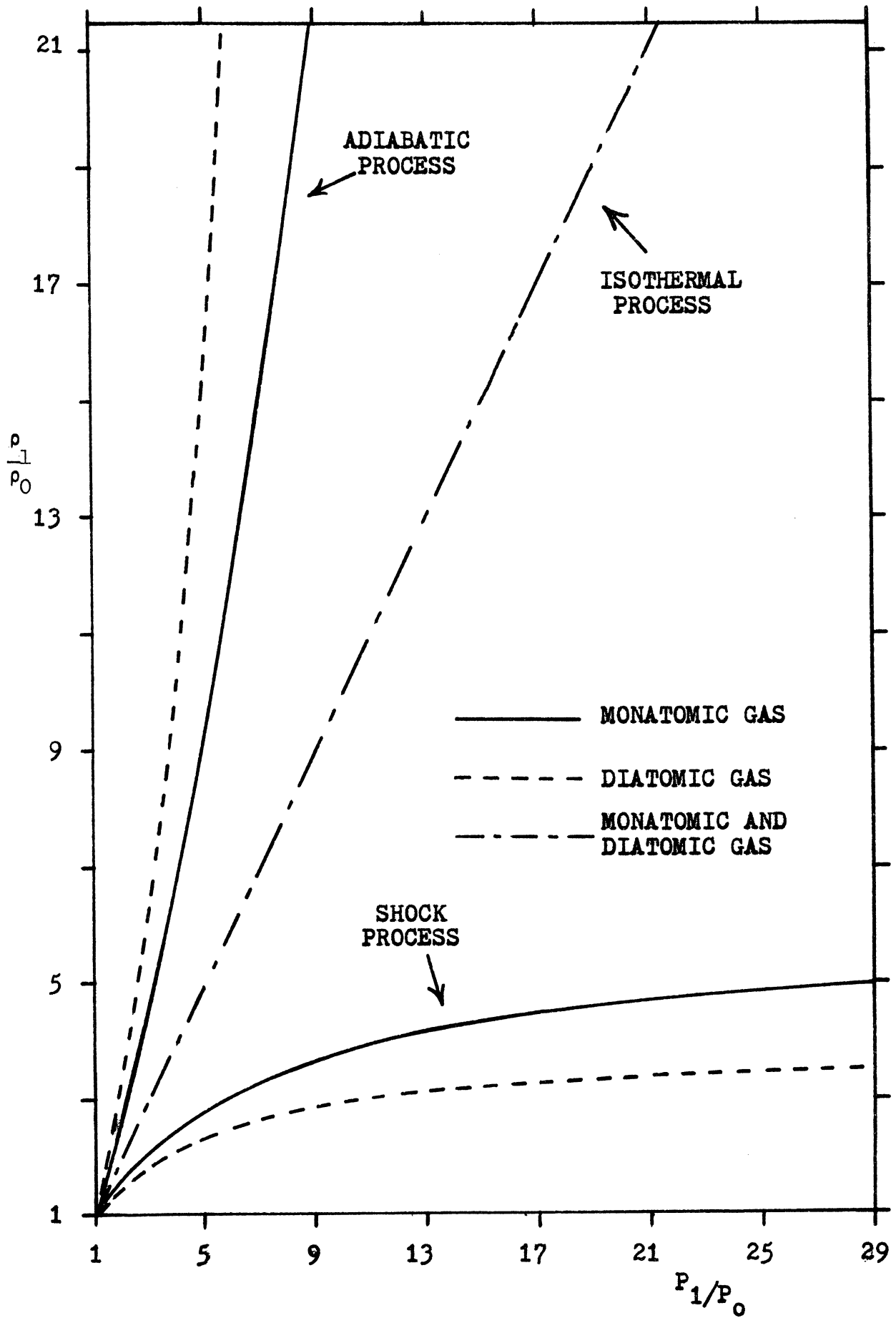
Figure 5. Comparisons of several thermodynamic processes

an ideal diatomic gas. There is, however, no upper limit on the density ratio attainable for the other processes. This difference in behavior strongly influences the final temperatures of the gases. For any pressure ratio the density of a shocked gas is always much lower than that of an adiabatically or isothermally compressed gas. Since the ideal gas equation must be obeyed, the temperature of the shocked gas must be much higher than that obtained for either of the other processes having the same pressure ratio. A pressure ratio of 200 in a room temperature gas results in a final temperature of $1333^{o}K$ in an adiabatically compressed gas, while the same pressure ratio in a shock-compressed gas gives a final temperature of 11 $690^{o}K$.

The shock must of course be an irreversible process. The physical reason is not obvious from the derivation given for the shock equations. Consideration was made only of a volume of gas before and after it passed through the shock front. No attempt was made to treat the processes going on within the shock itself. In this region, viscosity and heat conduction terms cannot be ignored in the flow equations. This viscosity, coupled with the very large gradients of the flow parameters, is what actually "causes" the heating and the irreversibility of the process.

3. Effects of the Internal Degrees of Freedom

In order to complete the shock calculation, $e(P,\rho)$ must be known for the gas under consideration. The previous calculation for ideal gases is inadequate since energy is taken up in the excited energy states of the gas. These effects will now be considered in detail for a diatomic gas.

In shock tube research, gases at low pressures and/or high temperatures are used. Van der Waals forces need not be taken into account. This is also true for low temperature hydrogen as can be seen from the National Bureau of Standards data[15] given in Table I. The equation of state of the gas may then be written as*

$$P = \rho RT/M \qquad \text{or} \qquad PV = NkT \qquad \text{or} \qquad P = nkT \qquad (15)$$

where R is the gas constant per mole, M is the molecular weight of the gas, and N is the total number of molecules.

The internal energy of a gas consists of the translational energy and the energy contained in the rotational, vibrational, and the electronically excited states. The additional complications which arise if dissociation or ionization occurs are straightforward but complex. These cases will

---

*It is interesting to note that PV = NkT is adequate to describe even dissociating and ionizing gases provided that N is regarded as a new variable which is determined by statistical mechanical considerations.

density in units of amagats[*]

T \ ρ	1	2	3	
16	.9909	.9818	.9728	
20	.9933	.9867	.9802	
25	.995	.990	.985	
30	.9964	.9928	.9892	
35	.997	.994	.992	
40	.9977	.9955	.993	
50	.998	.997	.996	
60	.9990	.9980	.9970	(z)
70	.9993	.9987	.9980	
80	.9996	.9992	.9988	
100	.9999	.9998	.9997	
150	1.0003	1.0006	1.0009	
200	1.0005	1.0010	1.0015	
250	1.0006	1.0016	1.0018	
300	1.0006	1.0013	1.0019	
400	1.0007	1.0014	1.0021	
600	1.0007	1.0015	1.0022	

$$Z = PV/RT$$

Table I. Hydrogen equation of state[15]

[*]See page 78

be ignored in this discussion. O. Laporte[14] has written a complete description of these more complicated situations.

An expression for the internal energy of an ideal gas considering the excited molecular states can be written

$$E = \frac{3}{2}nkT + n \frac{\sum_j \epsilon_j g_j e^{-\epsilon_j/kT}}{\sum_j g_j e^{-\epsilon_j/kT}} \tag{16}$$

where,

E = ρe = energy per unit volume

ϵ_j = energy of the jth excited state

g_j = degeneracy of the jth excited state.

To a good approximation the rotational and vibrational motions can be considered as independent. The vibrational energy eigenvalues are almost identical to those for a quantum mechanical harmonic oscillator.

$$\epsilon_v = (v + \tfrac{1}{2}) h\nu \tag{17}$$

where,

v = 0, 1, 2, 3, 4, ...

h = Planck's constant

ν = frequency of vibration associated with the molecule

The rotational motion can be closely described by a quantum mechanical rigid rotator. The energy eigenvalues are

$$\epsilon_R = j(j+1) \, \hbar^2/2I$$

where,

$$j = 0, 1, 2, 3, 4, \ldots$$

$$\hbar = h / 2\pi$$

$$I = \text{moment of inertia of the molecule.}$$

There is a degeneracy for each eigenstate of

$$g_j = 2j + 1. \tag{19}$$

The energy spacing between the rotational states is always very much smaller than that between the vibrational states.

Each energy state is given by the sum of two terms

$$\epsilon(v,j) = \epsilon_V(v) + \epsilon_R(j). \tag{20}$$

The expression for the internal energy of the gas (Eq. 16) becomes

$$\frac{E}{n} = \frac{3}{2}kT + \frac{\sum\limits_{v=0}^{\infty} \sum\limits_{j=0}^{\infty} (2j+1) \; \epsilon(v,j) \; e^{-\epsilon(v,j)/kT}}{\sum\limits_{v=0}^{\infty} \sum\limits_{j=0}^{\infty} (2j+1) \; e^{-\epsilon(v,j)/kT}} \tag{21}$$

Substitution of Eq. 20 into Eq. 21, with rearrangement and cancellation of terms, leads to

$$\frac{E}{n} = \frac{3}{2}kT + \frac{\sum\limits_{j=0}^{\infty} \epsilon_V(v) \; e^{-\epsilon_V(v)/kT}}{\sum\limits_{v=0}^{\infty} e^{-\epsilon_V(v)/kT}} + \frac{\sum\limits_{j=0}^{\infty} (2j+1) \; \epsilon_R(j) \; e^{-\frac{\epsilon_R(j)}{kT}}}{\sum\limits_{j=0}^{\infty} (2j+1) \; e^{-\epsilon_R(j)/kt}} \tag{22}$$

The rotational and vibrational contributions appear separately.

Since $\epsilon_V = (v+\tfrac{1}{2})\, h\nu$ the vibrational term can be summed, resulting in the form

$$\frac{E}{n} = \frac{3}{2}kT + \frac{h\nu}{e^{h\nu/kT} + 1} + \frac{\displaystyle\sum_{j=0}^{\infty} (2j+1)\, \epsilon_R(j)\, e^{-\epsilon_R(j)/kT}}{\displaystyle\sum_{j=0}^{\infty} (2j+1)\, e^{-\epsilon_R(j)/kT}} \qquad (23)$$

where the zero point energy has been ignored.

There are two limiting cases which often allow one or both of the above terms either to be ignored completely or to be written in a simpler form. One limit is that for which the temperature is so low that only the ground state for a particular degree of freedom is occupied. In this limit, the corresponding term in Eq. 23 approaches zero. The second limiting case is that for which the temperature is so high that a large number of states are occupied. This allows the classical limit of $\tfrac{1}{2}kT$ to be used for the contribution of each degree of freedom to the internal energy of the gas. In neither of these two limits does the discrete energy structure of the gas make itself known.

In order to recognize more easily whether a given degree of freedom may be ignored or treated classically, it is convenient to define a characteristic temperature for each gas as

$$\theta_R = \hbar^2/2Ik \qquad \text{and} \qquad \theta_V = h\nu\,/k \qquad (24)$$

θ is sometimes called the Einstein temperature. Whenever $T \ll \theta$, the degree of freedom can be ignored. Whenever $T \gg \theta$,

the degree of freedom can be treated classically. Values of θ_R and θ_V for several gases are given in Table II.

As can be seen from Table II, for almost all diatomic gases at room temperature or above, $\theta_R \ll T$, and the rotational degrees of freedom may be treated classically. Equipartition of energy demands that the same amount of energy reside in each degree of freedom and that this energy be $\frac{1}{2}kT$. So the energy per unit volume of the gas is given by[*]

$$\frac{E}{n} = \frac{e \, \rho}{n} = \frac{5}{2}kT + \frac{h\nu}{e^{h\nu/kT} + 1} \tag{25}$$

Another frequently realized case is that for which the temperature is so low that only the ground vibrational state is populated. This is true for most diatomic molecules at temperatures of less than $1000^\circ K$. In this case

$$\frac{E}{n} = \frac{5}{2}kT, \tag{26}$$

and the gas behaves as a classical diatomic gas. The other limit $T \gtrsim \theta_V$ leads to further complications since then dissociation takes place and this energy, together with the energies of the internal states of each dissociation product, must be taken into account.

---

[*]Rotation of a diatomic gas counts as two degrees of freedom since there are two axes about which the molecule may rotate.

	$\theta_R(^\circ K)$ *	$\theta_V(^\circ K)$ *
H_2	85.4	6249
HD	64.3	5425
D_2	43.0	4440
N_2	2.9	3395
O_2	2.1	2273
F_2	2.	1284
CO	2.8	3122
Cl_2	.35	811
Br_2	.12	465
O_3		1014, 1501, 1597
CO_2		960, 1870, 4776
H_2O		2295, 5265, 5433
SO_2		745, 1656, 1959

Table II. θ_R and θ_V for several gases

----

*Calculated from data given in the Handbook of Physics[26] and N.B.S. circular[15]

For temperatures so low that $T \ll \theta_R$, the rotational degrees of freedom become completely frozen out. The internal energy of the gas can then be written

$$\frac{E}{n} = \frac{3}{2} kT \tag{27}$$

and is identical to that for a classical monatomic gas.

The interesting nonclassical behavior of a gas occurs near $T = \theta$. The nonclassical vibrational behavior has been studied using room temperature shock tubes. The only gases which are not liquefied or solidified near $T = \theta_R$ are hydrogen, deuterium, and hydrogen deuteride. For low temperatures in these gases, the discrete structure of the rotational eigenstates must be considered when thermodynamic calculations are made.

Given the initial conditions and the shock speed measurement, Eqs. 7, 8, and 23 are sufficient to allow the calculation of the final state of the gas behind the shock wave. These equations apply to any diatomic or monatomic gas.

4. Hydrogen Internal Energy - A Detailed Description

A more accurate expression for the energy states of a diatomic molecule is[15]

$$\epsilon (v,j) = (G_v - G_0) + B_v\, j(j+1) + D_v\, j^2(j+1)^2 + \qquad (28)$$

$$+ F_v\, j^3(j+1)^3 + H_v\, j^4(j+1)^4 + \frac{H_v^2 j^8(j+1)^8}{F_v j^3(j+1)^3 - H_v j^4(j+1)^4}$$

where, values for hydrogen from the N.B.S. data[15] are

$$G_v = 4405.3(v+\tfrac{1}{2}) - 125.325(v+\tfrac{1}{2})^2 + 1.95(v+\tfrac{1}{2})^3 - 0.113(v+\tfrac{1}{2})^4$$

$$B_v = 60.8483 - 3.06635(v+\tfrac{1}{2}) + 0.06836(v+\tfrac{1}{2})^2 - 0.0065(v+\tfrac{1}{2})^3$$

$$D_v = - 0.046435 + 0.0014904(v+\tfrac{1}{2}) - 0.000063648(v+\tfrac{1}{2})^2$$

$$F_v = 4.93203 \times 10^{-5} + 0.02800 \times 10^{-5}(v+\tfrac{1}{2}) \qquad (29)$$

$$H_v = - 6.7217 \times 10^{-8} \qquad\qquad (cm^{-1})$$

The excited vibrational states for hydrogen are insignificantly populated at temperatures less than $1000^\circ K$. Since this is the region of interest for this experiment, the energy level expression can be considerably simplified to read

$$\epsilon (j) = B\, j(j+1) + D\, j^2(j+1)^2 + F\, j^3(j+1)^3 + j^4(j+1)^4 +$$

$$+ \frac{H\, j^4(j+1)^4}{F\, j^3(j+1)^3 - H\, j^4(j+1)^4} \qquad (30)$$

The values of these constants are

$$B = 59.3314 \qquad\qquad D = -0.45706$$

$$F = 4.94603 \times 10^{-5} \qquad H = -6.7217 \times 10^{-8}\ (cm^{-1}) \qquad (31)$$

Eq. 23 can be written

$$\frac{E}{n} = \frac{3}{2}kT + \frac{\sum_{j=0}^{\infty} (2j+1) \, \epsilon_R(j) \, e^{-\epsilon_R(j)/kT}}{\sum_{j=0}^{\infty} (2j+1) \, e^{-\epsilon_R(j)/kT}} \qquad (32)$$

This is the form of the energy expression for the case in which the vibrational degree of freedom can be ignored, but the rotational energy states must be considered in detail. The infinite series converges very rapidly and usually only the first few terms need be calculated.

There is an additional consideration which must be made for diatomic molecules which posess identical constituent atoms (H_2, D_2, N_2, O_2, etc.). Transitions during collisions may be made between even rotational states and between odd rotational states but not between an even and an odd rotational state. This is a consequence of the symmetry requirements on the molecular wave function under interchange of nuclei. The wave function must be antisymmetric for nuclei having ½ integral spins (Fermi-Dirac statistics), whereas it must be symmetric for nuclei having integral spins (Bose-Einstein statistics).

The quantum mechanical rigid rotator wave functions each posesses a definite symmetry with respect to spacial inversion. This is equivalent to a nuclear interchange. The even j states are symmetric, whereas the odd j states are antisymmetric. As a result, for the case of hydrogen which has half integral spin nuclei, the state in which the nuclear spins are opposed (antisymmetric) can only be found associated with even j

rotational eigenstates (symmetric) in order that the total wave function be antisymmetric. Likewise, the state in which the nuclear spins are parallel (symmetric) can only be found associated with odd j rotational eigenstates (anti-symmetric). In order to make a transition from an even j to an odd j rotational eigenstate a nuclear spin flip is therefore required. This is a very slow process for a pure gas in a clean container. Weeks or even months are required for a significant number of transitions to take place. Thus for essentially all thermodynamic processes, hydrogen behaves as a mixture of two separate constituents.

The two constituents of hydrogen are called orthohydrogen and parahydrogen. Orthohydrogen consists of all molecules in rotational states of odd j values, whereas parahydrogen consists of all molecules in rotational states of even j values. There is a nuclear spin degeneracy of 3 for each state for which j is odd (spins parallel). This is due to the fact that there are 3 spin wave functions for this case. There is no degeneracy for states with even j (spins opposed) since there is only one spin state. Thus the internal energy equation for hydrogen must be written[*]

$$\frac{E}{n} = \frac{3}{2}kT + \frac{1}{4} \frac{\sum_{even} (2j+1) \epsilon_j \, e^{-\epsilon_j/kT}}{\sum_{even} (2j+1) \, e^{-\epsilon_j/kT}} + \frac{3}{4} \frac{\sum_{odd} (2j+1) \epsilon_j \, e^{-\epsilon_j/kT}}{\sum_{odd} (2j+1) \, e^{-\epsilon_j/kT}}$$

(33)

[*]See footnote on next page

This separation of hydrogen into two components has a very pronounced influence on the thermodynamic behavior of the gas at low temperatures. This was first observed by A. Eucken[16] in 1912 as an anomaly of the measured specific heat curve. This is shown in Fig. 6. Attempts made by Hund[17] in 1927 to explain the specific heat results, starting with the already well known internal rotational energy structure of hydrogen, led to a curve which differed appreciably from the experimental results. The behavior of the specific heat curve was finally explained by D. M. Dennison[18] in 1927, who proposed the two component model described above.

The fraction of molecules in each rotational eigenstate, ϵ_j, of the gas can easily be calculated for all temperatures from the following formula of statistical mechanics

$$ n_i = \frac{g_i \, e^{-\epsilon_i/kT}}{\sum\limits_{all \ s} g_s \, e^{-\epsilon_s/kT}} \qquad (34) $$

---

*Note that it would be INCORRECT to write the internal energy as

$$ \frac{E}{n} = \frac{3}{2}kT + \frac{\sum\limits_{even}(2j+1)\,\epsilon_j\,e^{-\epsilon_j/kT} + 3\sum\limits_{odd}(2j+1)\,\epsilon_j\,e^{-\epsilon_j/kT}}{\sum\limits_{even}(2j+1)\,e^{-\epsilon_j/kT} + 3\sum\limits_{odd}(2j+1)\,e^{-\epsilon_j/kT}} $$

since ortho and parahydrogen must be treated as separate and distinguishable gases. This equation would, however, be valid for very slow thermodynamic processes in the presence of a catalyst.
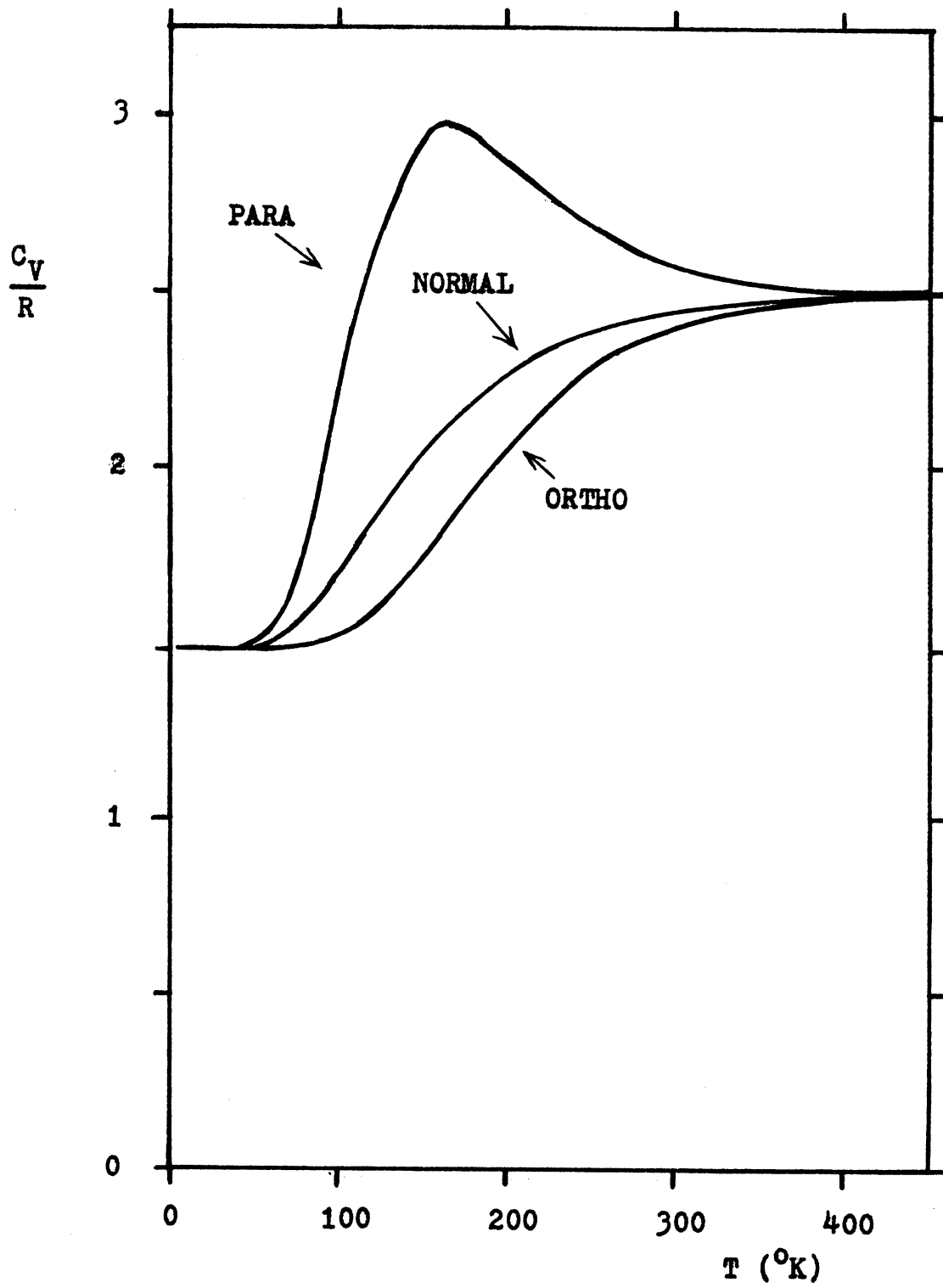
Figure 6. Specific heat of the three forms of hydrogen

Thus the fractional population of the para and the ortho-hydrogen eigenstates can be written as

$$n_j = \frac{(2j+1)\, e^{-\epsilon_j/kT}}{\sum\limits_{j \text{ even}} (2j+1)\, e^{-\epsilon_j/kT}} \qquad \text{(parahydrogen)} \qquad (35)$$

$$n_j = \frac{(2j+1)\, e^{-\epsilon_j/kT}}{\sum\limits_{j \text{ odd}} (2j+1)\, e^{-\epsilon_j/kT}} \qquad \text{(orthohydrogen)} \qquad (36)$$

The evaluation of these expressions gives results that are shown in Figs. 7 and 8. At low temperatures the lowest two energy levels are occupied, since the rotational transition from $j=1$ to $j=0$ cannot take place.

It is possible to obtain pure parahydrogen by cooling normal hydrogen in the presence of a special catalyst which speeds up the j odd $\longleftrightarrow$ j even transitions. If the gas is then transferred to a clean container before rewarming, pure parahydrogen is obtained. This gas will remain pure parahydrogen for several weeks if it does not come into contact with paramagnetic substances such as oxygen, nitric oxide, activated charcoal, etc.. Table III shows the percentage of parahydrogen obtained as a function of the temperature to which the catalyst is cooled. There is, unfortunately, no way known of producing pure orthohydrogen. The room temperature concentration of 75% orthohydrogen is the highest one experimentally attainable. This is usually
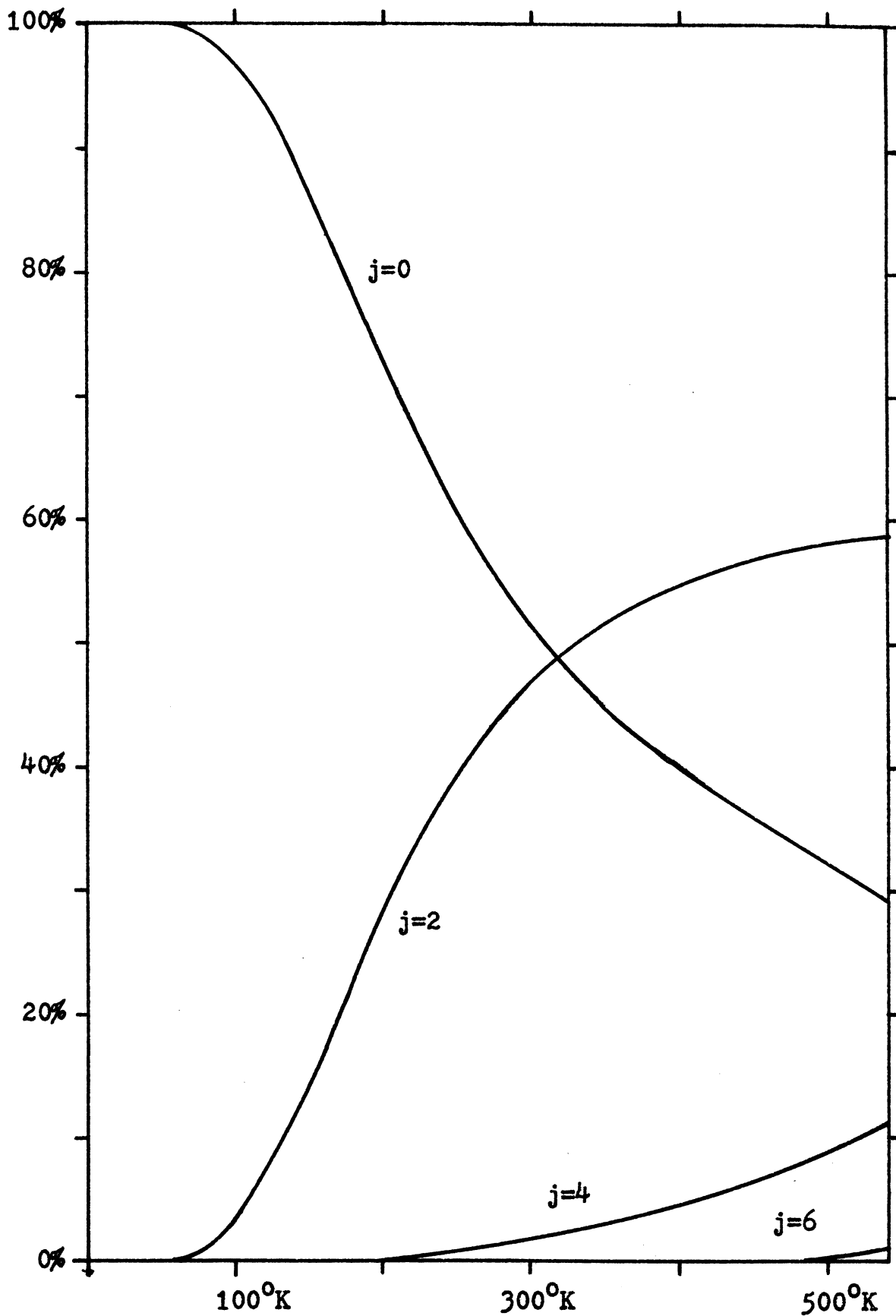
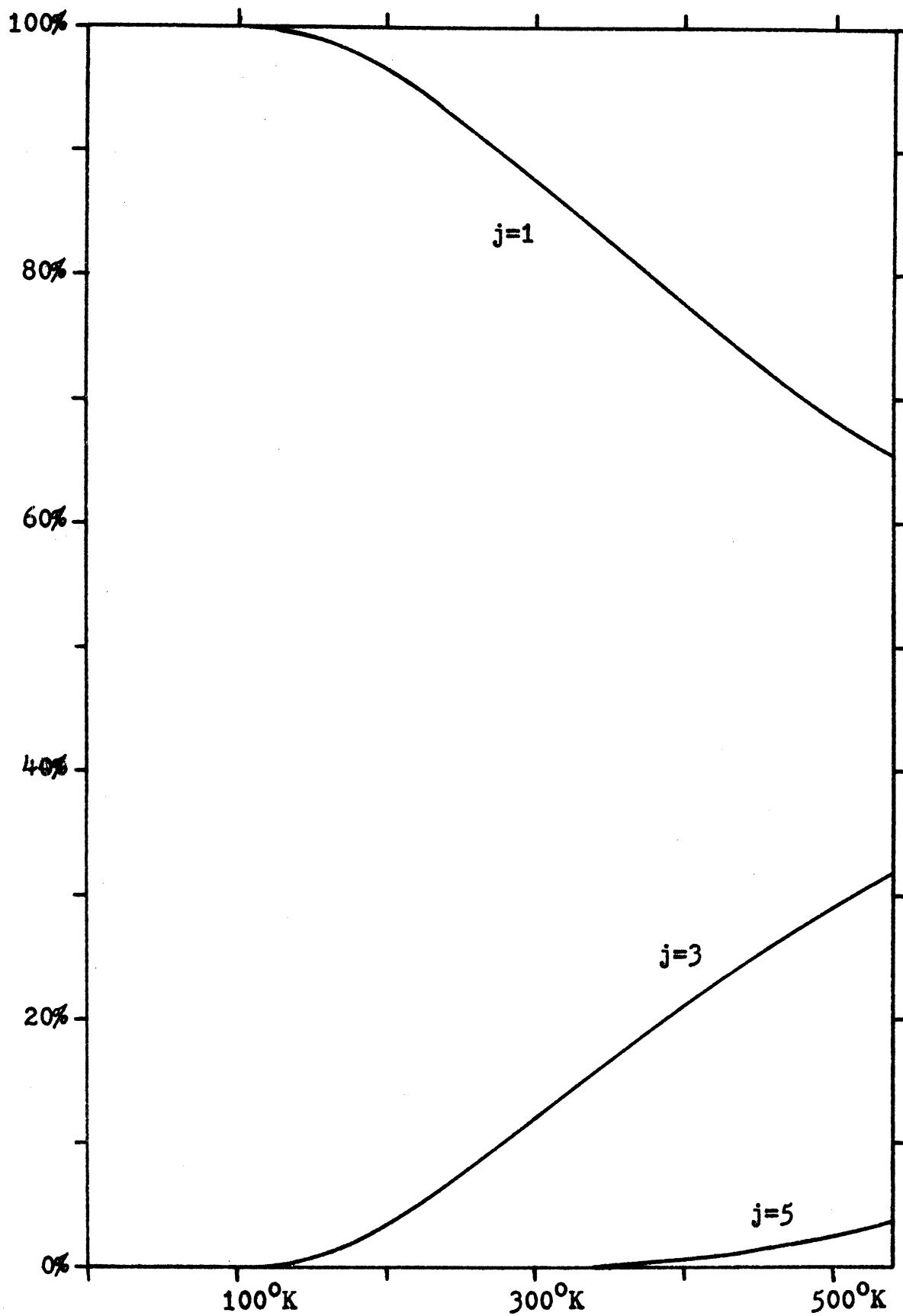Figure 7. % population of rotational energy states for parahydrogen

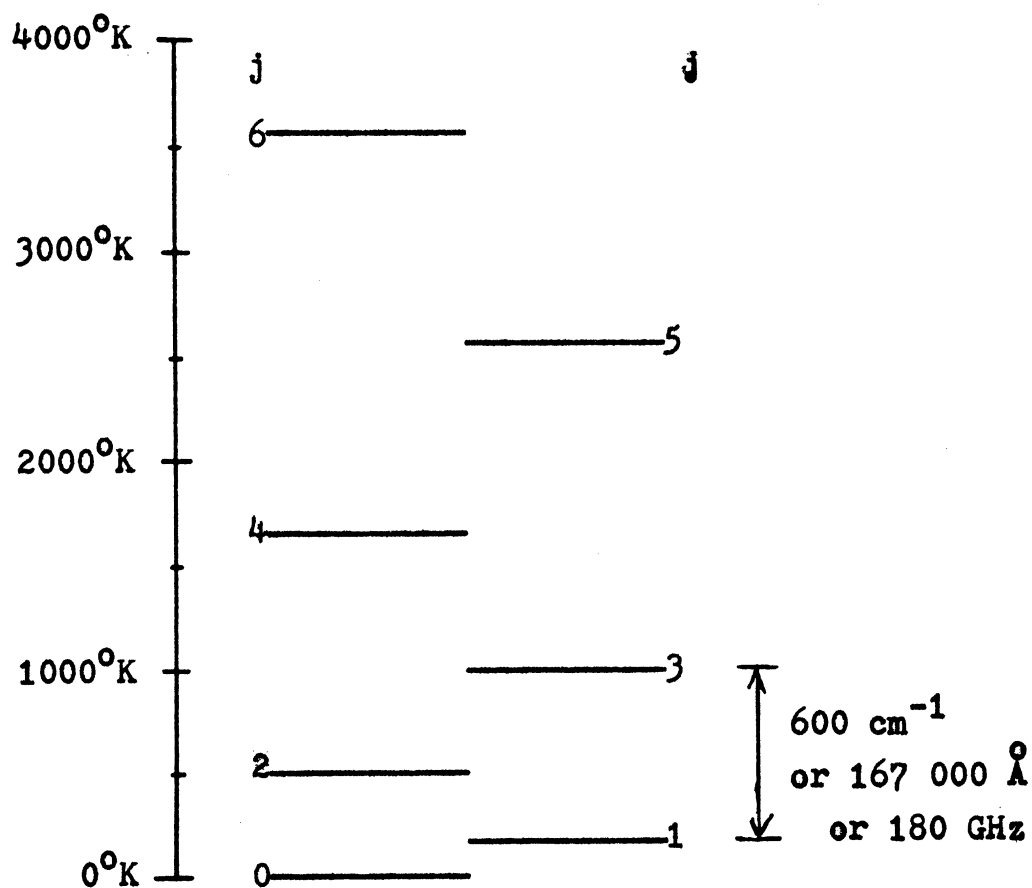Figure 8. % population of rotational energy states for orthohydrogen

Figure 9. Rotational energy levels for hydrogen

T (^{O}K)	percentage parahydrogen
10	99.999
20	99.821
30	97.021
40	88.727
50	77.054
60	65.569
80	48.537
100	38.620
150	28.603
300	25.072

Table III. Equilibrium percentages of parahydrogen

is usually referred to as normal hydrogen.

In order to understand the thermodynamic behavior of hydrogen better, it is helpful to define the "effective degrees of freedom" due to rotation as

$f_R/2$ = (energy contained in the rotational states) / kT

or,

$$\frac{f_R}{2} = \frac{\sum_j (2j+1)\epsilon_j \ e^{-\epsilon_j/kT}}{kT \sum_j (2j+1) \ e^{-\epsilon_j/kT}} \tag{37}$$

For para(ortho)hydrogen these sums extend only over the even (odd) values of j. For normal hydrogen the value of f_R is given by

$$f_R^{normal} = \tfrac{1}{4} (f_R^{para} + 3f_R^{ortho}) \tag{38}$$

A plot of the results of the evaluation of these sums is given in Fig. 10. As T approaches zero both components settle into their lowest rotational eigenstates. This has a consequence that

$$f_R^{para} \longrightarrow 0$$

whereas

$$f_R^{ortho} \longrightarrow \infty \quad \text{and} \quad f_R^{normal} \longrightarrow \infty .$$
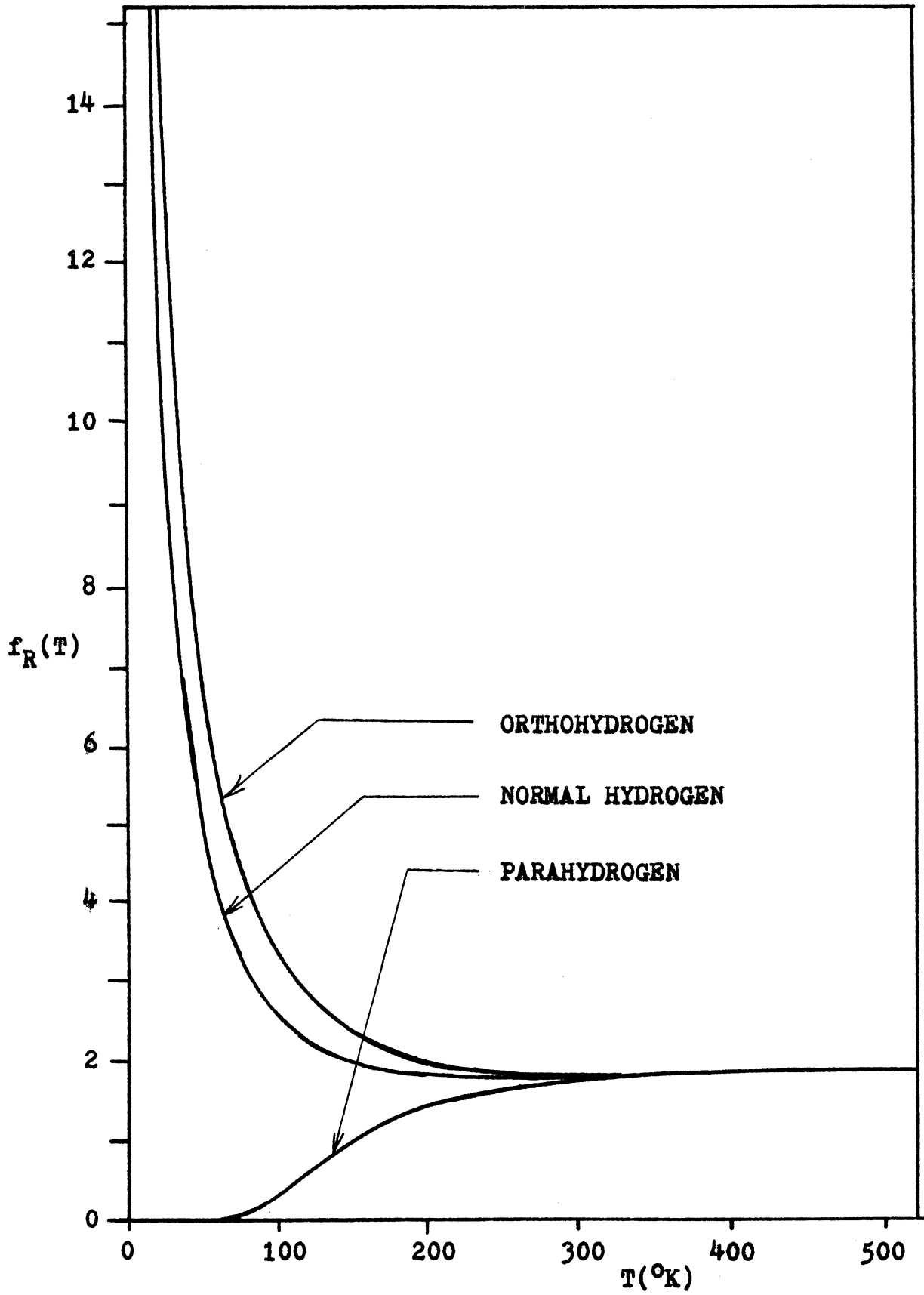
Figure 10. Effective degrees of freedom - $f_R(T)$

The reason for these differences is clear, namely, a certain amount of energy is "trapped" in the $j=1$ state.[*] This energy becomes larger and larger compared to kT as $T \longrightarrow 0$. f_R, however, was introduced with the expectation that the gas would behave monatomically whenever $f_R \longrightarrow 0$ and diatomically whenever $f_R \longrightarrow 2$. This correspondence works well with parahydrogen but not with orthohydrogen. The expected limits will occur for ortho and normal hydrogen if the zero of energy for the odd j states is taken to be ϵ_1, the energy of the $j=1$ rotational state. The energy of the higher states for the odd j levels must then be rewritten

$$\epsilon_j' = \epsilon_j - \epsilon_1 . \tag{39}$$

The new definition of the "effective degrees of freedom" for the rotational states of orthohydrogen, called f_R' for the moment, is

$$f_R' = \frac{\displaystyle\sum_{odd} (2j+1) \ \epsilon_j' \ e^{-\epsilon_j'/kT}}{kT \displaystyle\sum_{odd} (2j+1) \ e^{-\epsilon_j'/kT}} \tag{40}$$

The values obtained from these summations are shown in Fig. 11. f_R' can now be used as a parameter describing the transition

---

[*]For example, at the boiling point of liquid hydrogen, $20.4^{\circ}K$, there is 6 times more energy in rotation $(18/2 \ kT)$ than in translation.
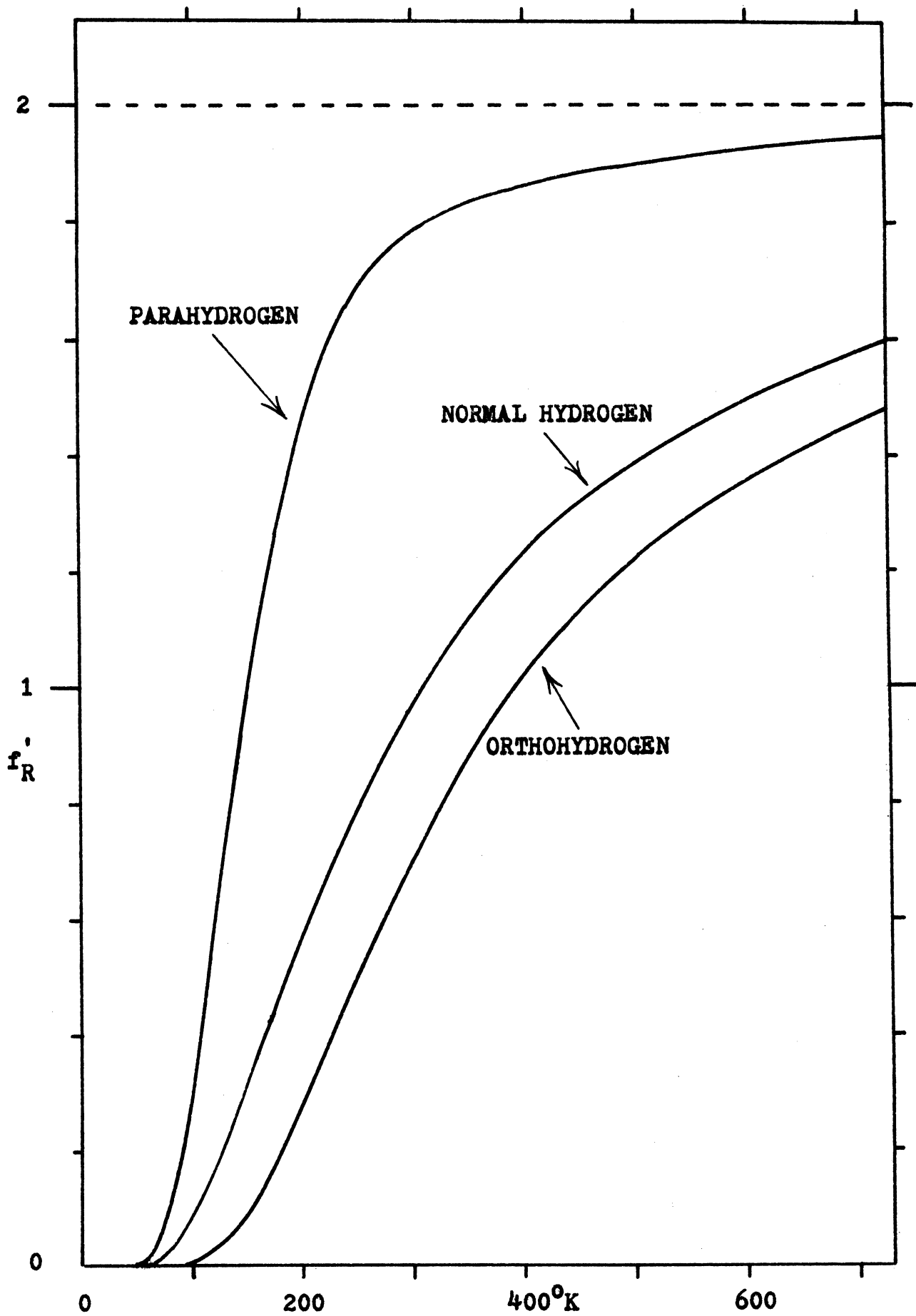
Figure 11. Effective degrees of freedom - $f_R'(T)$

from monatomic to diatomic gas behavior. Neglecting the energy of the $j=1$ state for orthohydrogen is a perfectly legitimate procedure since it is not an observable in this experiment. This is similar to neglecting the zero point energy of the vibrational energy levels in section 3 of this chapter. A more detailed justification of the assertion that either f_R or f_R' can be used in the shock calculation, is given in the following paragraph.

Consistent use of either f_R or f_R' in the shock calculation, is valid due to the fact that only the quantity $(e_1 - e_0)$ is used. From Eqs. 32 and 37 this quantity can be written

$$(e_1 - e_0)\frac{M}{N_0 k} = \frac{3}{2}(T_1 - T_0) + T_1 f_R(T_1) - T_0 f_R(T_0) \tag{41}$$

where N_0 is Avagadro's number and M is the molecular weight of the gas. For orthohydrogen this expression can be written

$$\frac{M}{N_0 k}(e_1 - e_0) = \frac{3}{2}(T_1 - T_0) + \frac{\sum\limits_{odd} (2j+1)\, \epsilon_j\, e^{-\epsilon_j/kT_1}}{\sum\limits_{odd} (2j+1)\, e^{-\epsilon_j/kT_1}} \tag{42}$$

$$- \frac{\sum\limits_{odd} (2j+1)\, \epsilon_j\, e^{-\epsilon_j/kT_0}}{\sum\limits_{odd} (2j+1)\, e^{-\epsilon_j/kT_0}}$$

Substitution of Eq. 39 into Eq. 42, with cancellation and rearrangement of terms, yields an identical expression but with ϵ_j' in place of ϵ_j. This new expression can be written

$$(e_1 - e_0)\frac{M}{N_0 k} = \frac{3}{2}(T_1 - T_0) + T_1 f_R'(T_1) + T_0 f_R'(T_0).$$

This expression is identical to Eq. 41 and proves the assertion that either f_R or f_R' may be used in the shock calculation for orthohydrogen. The same argument is valid for normal hydrogen. From now on, f_R' will be used exclusively as the "effective degrees of freedom" for rotation in ortho-hydrogen and normal hydrogen; however, the (') symbol will be dropped.

As can be seen in Fig. 11, hydrogen behaves as a monatomic gas at temperatures below about $70^\circ K$. Its total effective degrees of freedom (rotation and translation), f, approaches 3. At room temperature there are a sufficiently large number of occupied rotational states that the energy contained in them approaches kT. At high temperatures hydrogen behaves as an ideal diatomic gas with f=5. The thermodynamic properties of orthohydrogen and parahydrogen become identical in both temperature extremes. It is noteworthy that only three or four energy levels need be populated before the classical diatomic limit is approached. The value of f at intermediate temperatures (and thus the thermodynamic behavior of the gas) depends critically on the exact energy level structure of the gas. The thermodynamic behavior of parahydrogen will be noticeably different from that for orthohydrogen.

5. Hydrogen Shock Calculation -- Rankine-Hugoniot Predictions

Although all of the information necessary for calculating the state of the shocked gas is contained in the preceding equations, it is more convenient for computational purposes if they are rewritten in another form. Eqs. 7 and 8, with the help of Eq. 41, can be written

$$\frac{P_1}{P_0} = \frac{(r_0+1)f_1 + \sqrt{f_1^2(r_0+1)^2 + 4(f_1+1)(1- r_0 f_0)}}{2(f_1+1)} \tag{43}$$

$$\frac{\rho_1}{\rho_0} = \frac{(f_1+1) P_1/P_0 + 1}{P_1/P_0 + (f_0+1)} \tag{44}$$

where the dimensionless quantity r_0 has been defined as

$$r_0 = \frac{Mu^2}{RT_0} \tag{45}$$

and is used as a measure of shock strength.

The ideal gas relation can be used to calculate the temperature ratio as

$$\frac{T_1}{T_0} = \frac{P_1/P_0}{\rho_1/\rho_0} \quad \text{sometimes written} \quad T_{10} = \frac{P_{10}}{\rho_{10}}. \tag{46}$$

The procedure for solving these nonlinear algebraic equations is shown in Fig. 12 as a flow diagram. For each measured value of shock speed, the final state of the gas
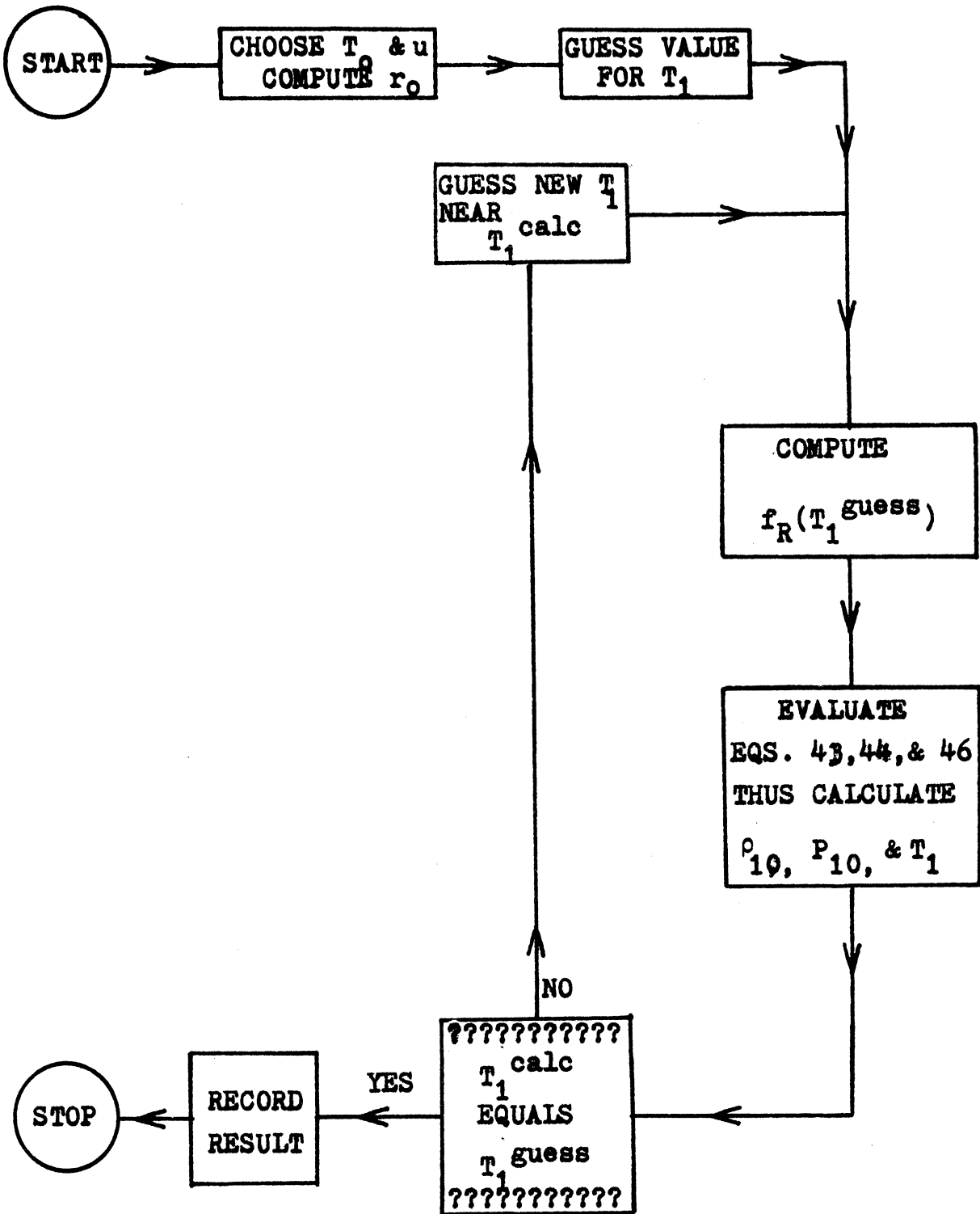
Figure 12. Flow diagram of shock calculation steps

behind the shock can be computed in terms of the measured initial conditions. Only three or four iterations are necessary to obtain satisfactory values of P_1, ρ_1, and T_1. This can even be done on a hand calculator. It is preferable, however, to use an electronic computer since many calculations are necessary, using various initial conditions and shock speeds. For this reason a computer program was devised to be used in the shock calculation. It was run on the University of Michigan I.B.M. 360/67 computer. Some of the results of this computation are shown in the following graphs. Thermodynamic states behind the shock as a function of shock velocity are shown in Figs. 13 to 18, for initial temperatures of $30^{\circ}K$ and $90^{\circ}K$. The Rankine-Hugoniot equation predictions for these initial temperatures are shown in Figs. 19 and 20. Figs. 21 and 22 show the different Rankine-Hugoniot curves obtainable for various initial temperatures.

The low and high temperature regions can be explained from Eq. 44. For low initial temperatures (e.g. $30^{\circ}K$) and low final temperatures, $f_1 = f_0 = 3$. Consequently the shock should behave as if it were traveling through a monatomic gas. For low initial temperatures but high final temperatures (i.e. for strong shocks in low temperature gases), Eq. 44 predicts that the density ratio should approach $f_1 + 1 = 6$ This is what is expected for a diatomic gas. Naturally, for both high initial and high final temperatures, the shock should behave diatomically for all shock strengths (until vibration and dissociation effects must be considered).

It should be noted that the monatomic behavior of hydrogen is displayed best for initial temperatures which are less than the boiling point of liquid nitrogen (77°K). For this reason it was necessary to use liquid helium as the coolant for much of the experiment. This imposed severe requirements on the design of the shock tube in order that the experiment could be completed at reasonable cost.

The Rankine-Hugoniot shock relation for ortho, para, and normal hydrogen are analogous to the specific heat curves of Fig. 6.
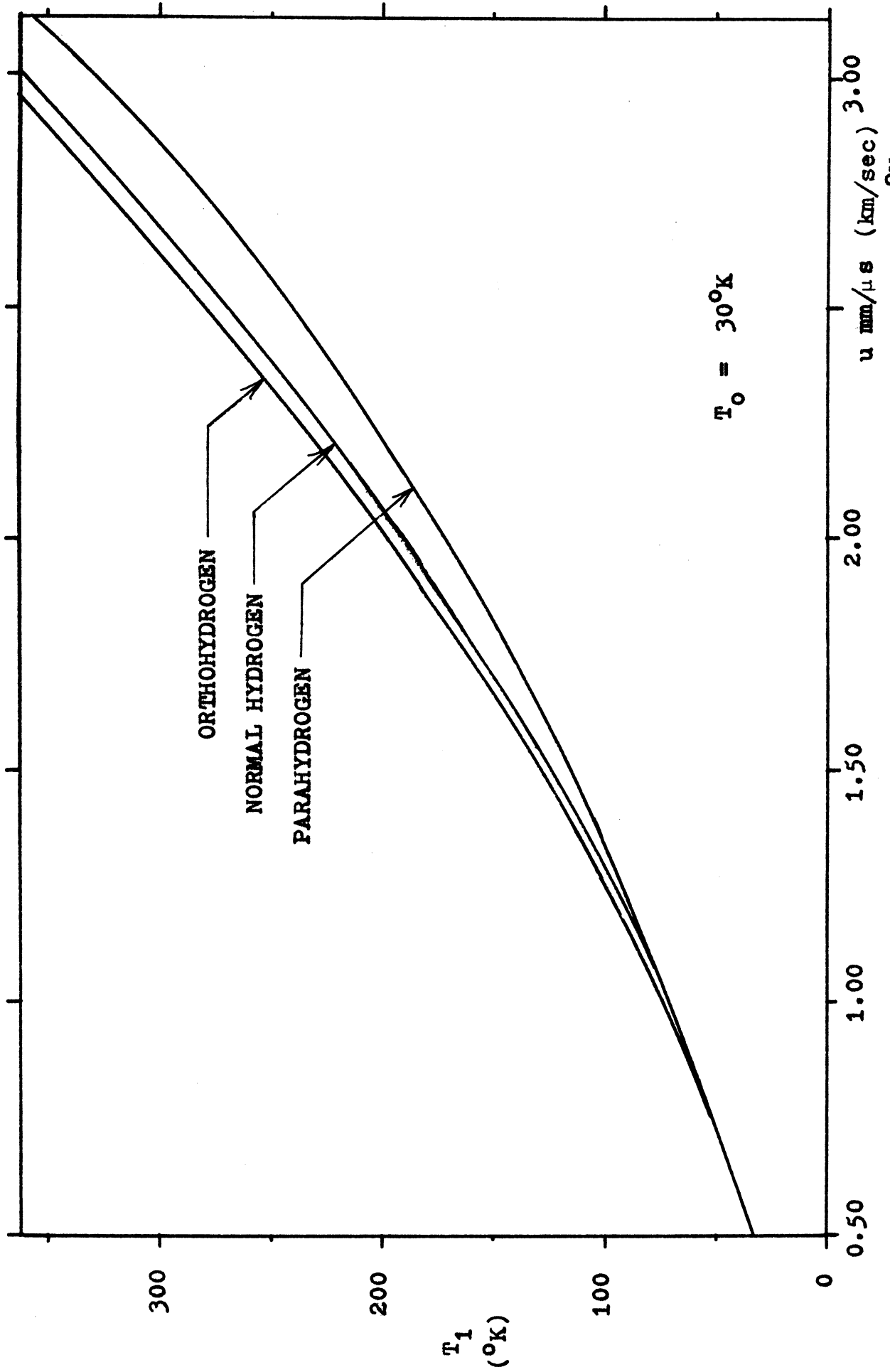
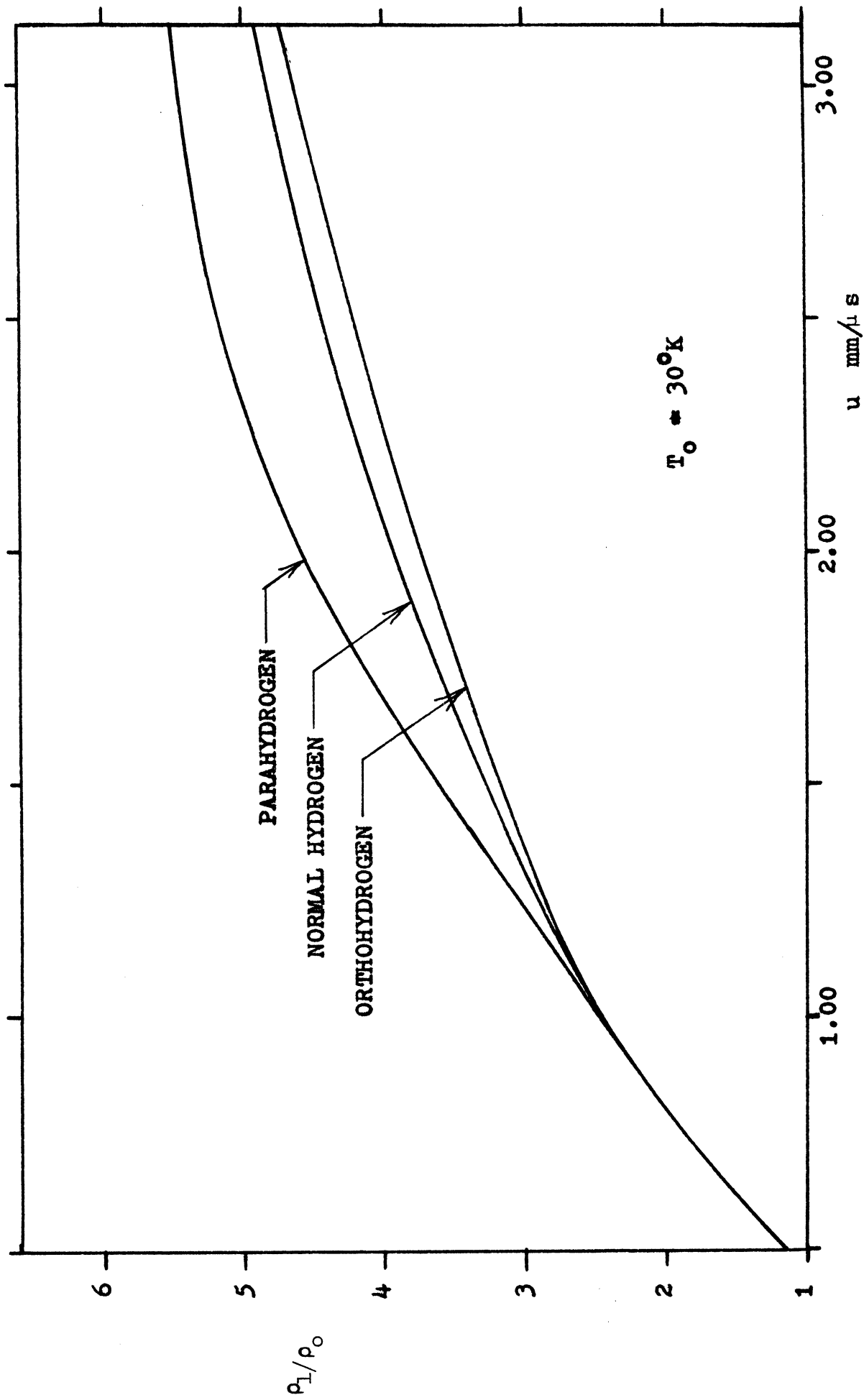Figure 13. Temperature as a function of shock speed for $T_o = 30°K$

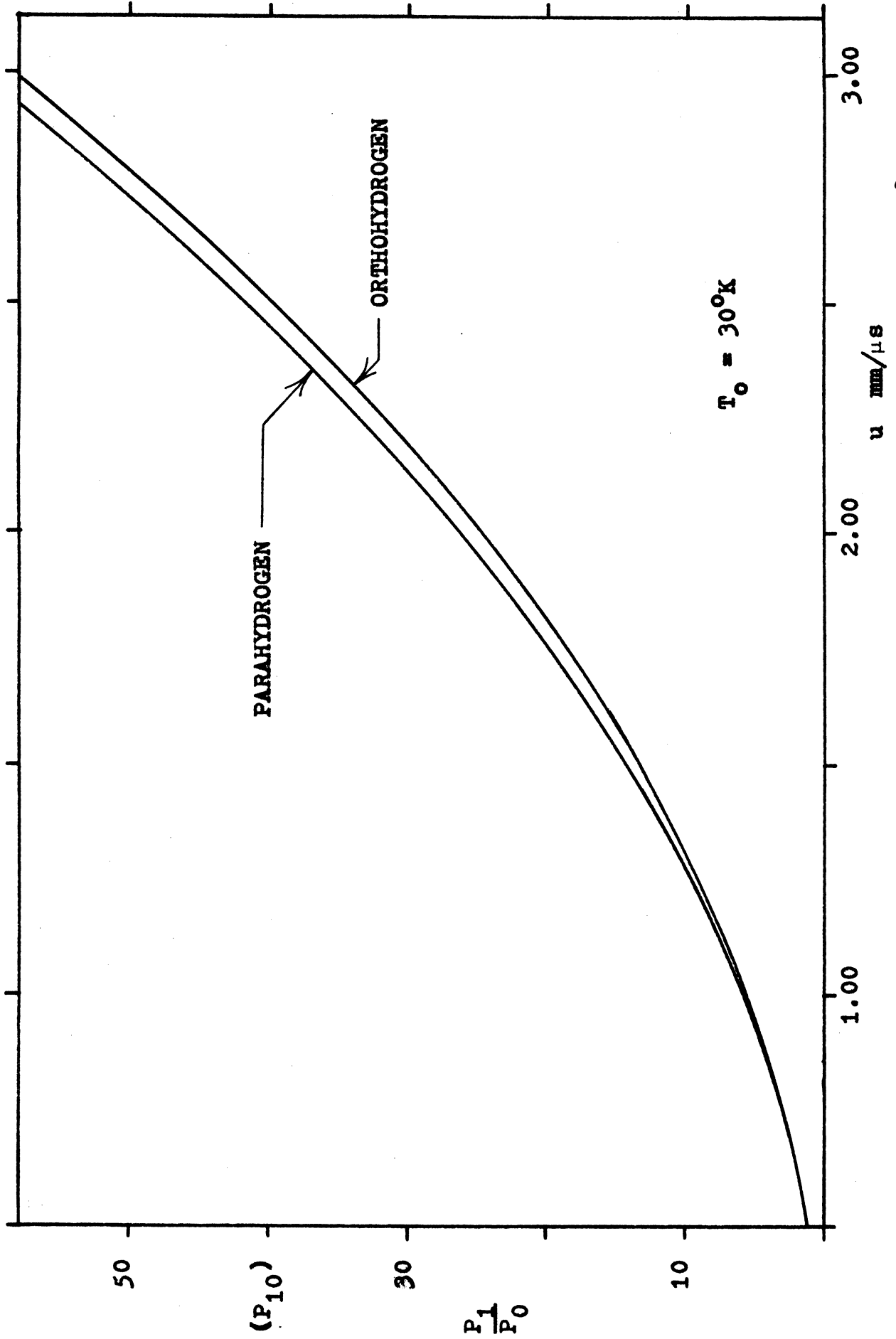Figure 14. Density ratio as a function of shock speed for $T_o = 30^\circ K$

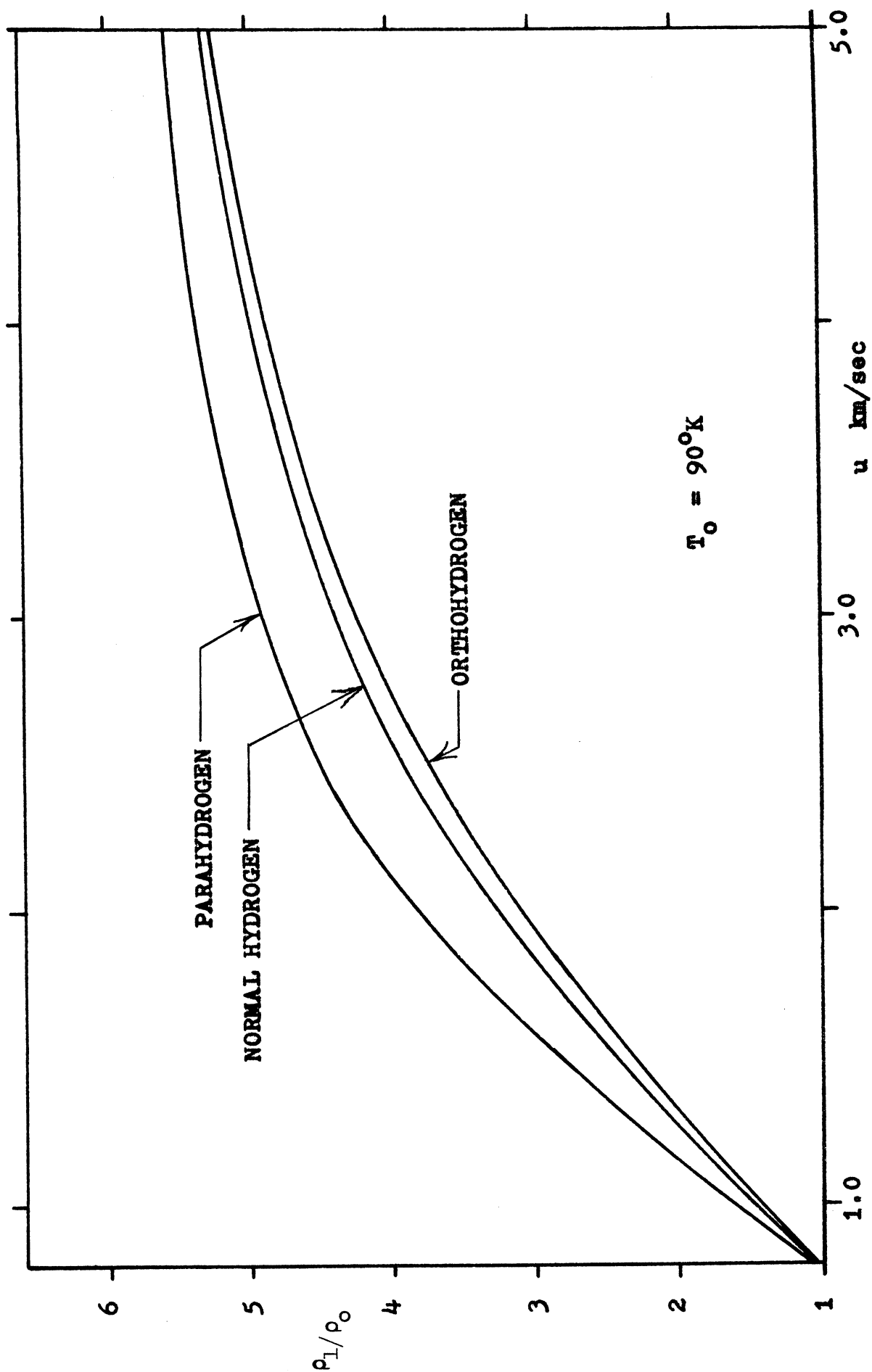Figure 15. Pressure ratio as a function of shock speed for $T_o = 30°K$

Figure 16. Density ratio as a function of shock speed for $T_o = 90^{\circ}K$
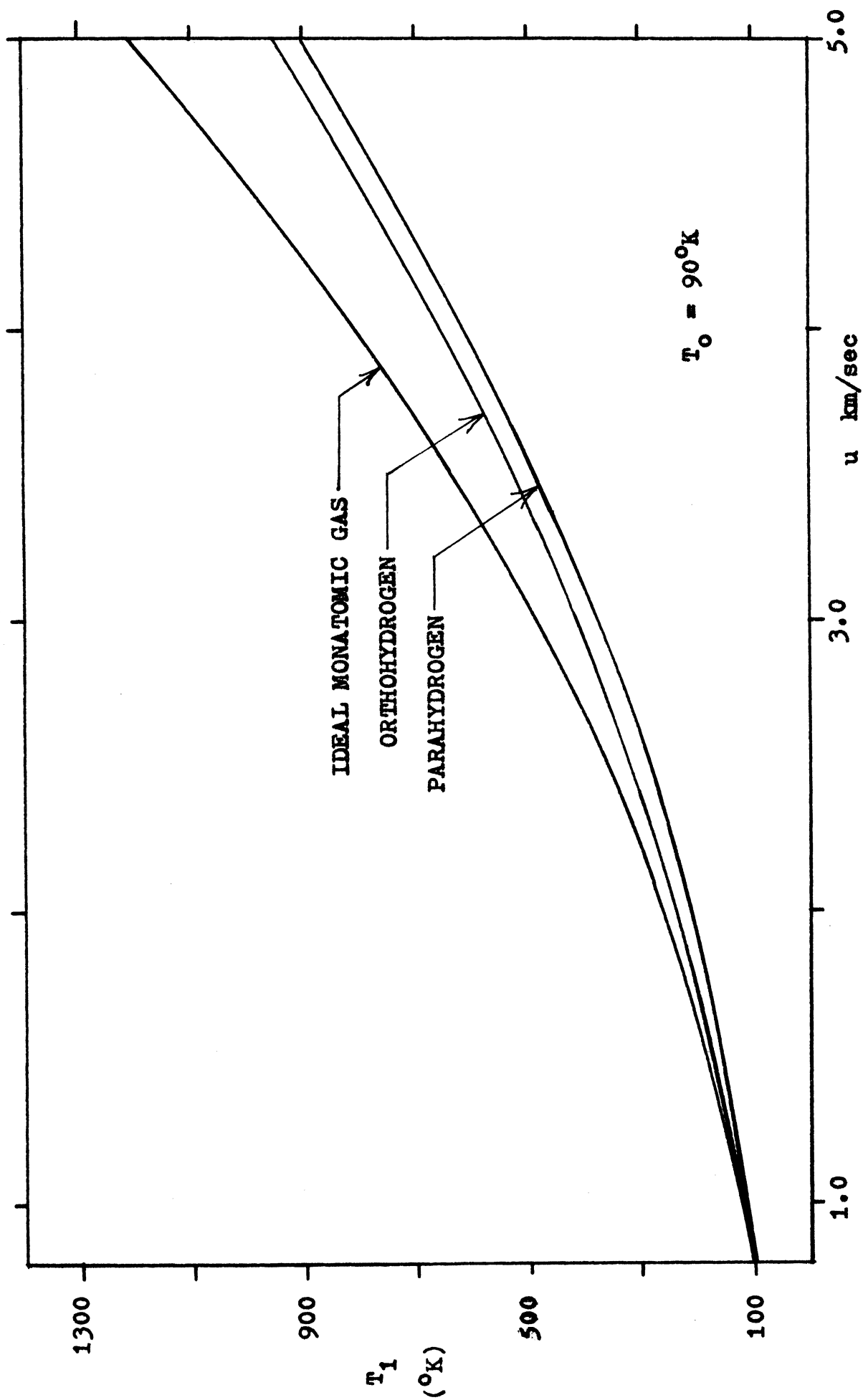
Figure 17. Temperature behind shock as a function of shock speed for $T_o = 90°K$

Figure 18. Pressure ratio as a function of shock speed for $T_o = 90°K$

Figure 19. Rankine-Hugoniot curves for T_o = 30°K
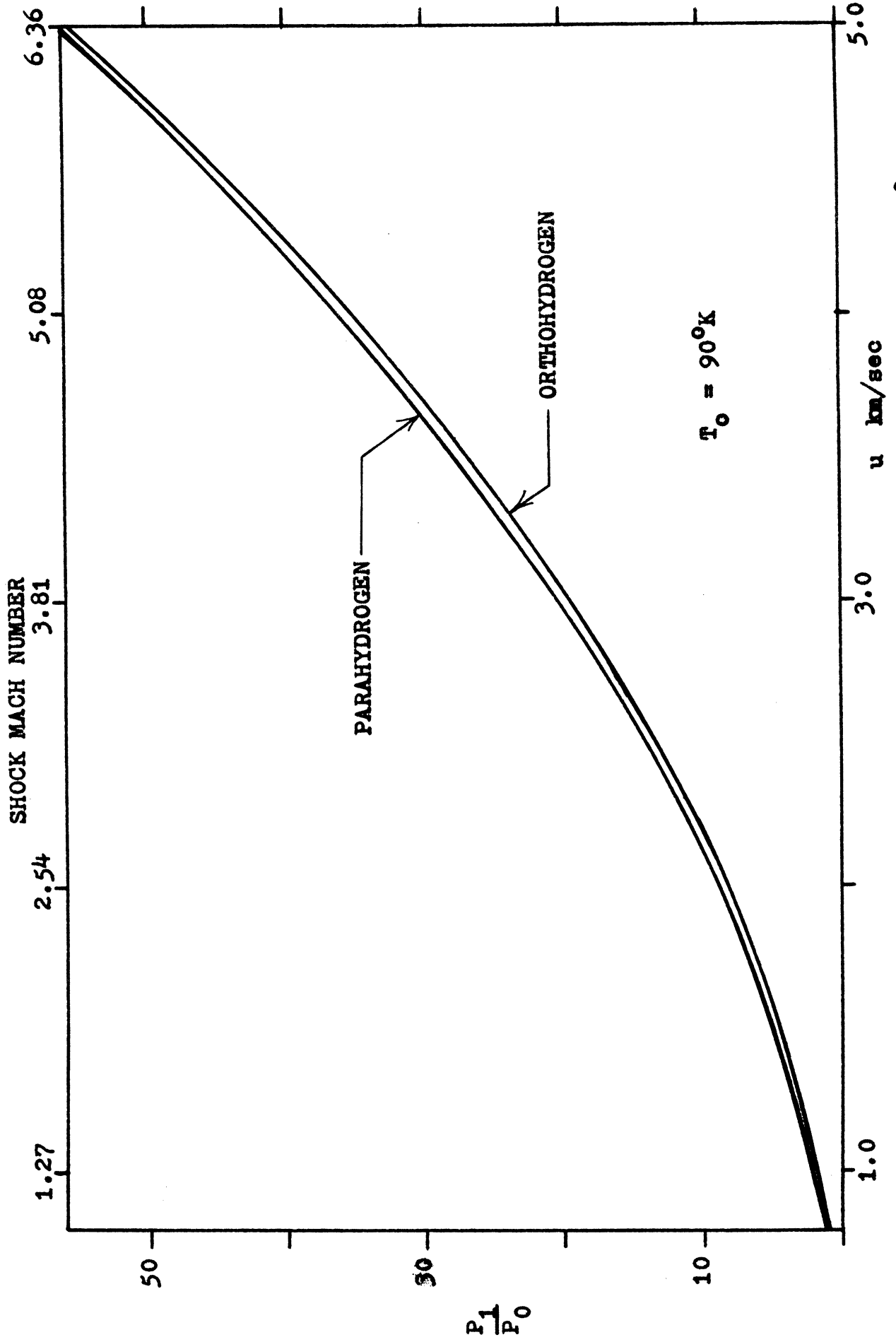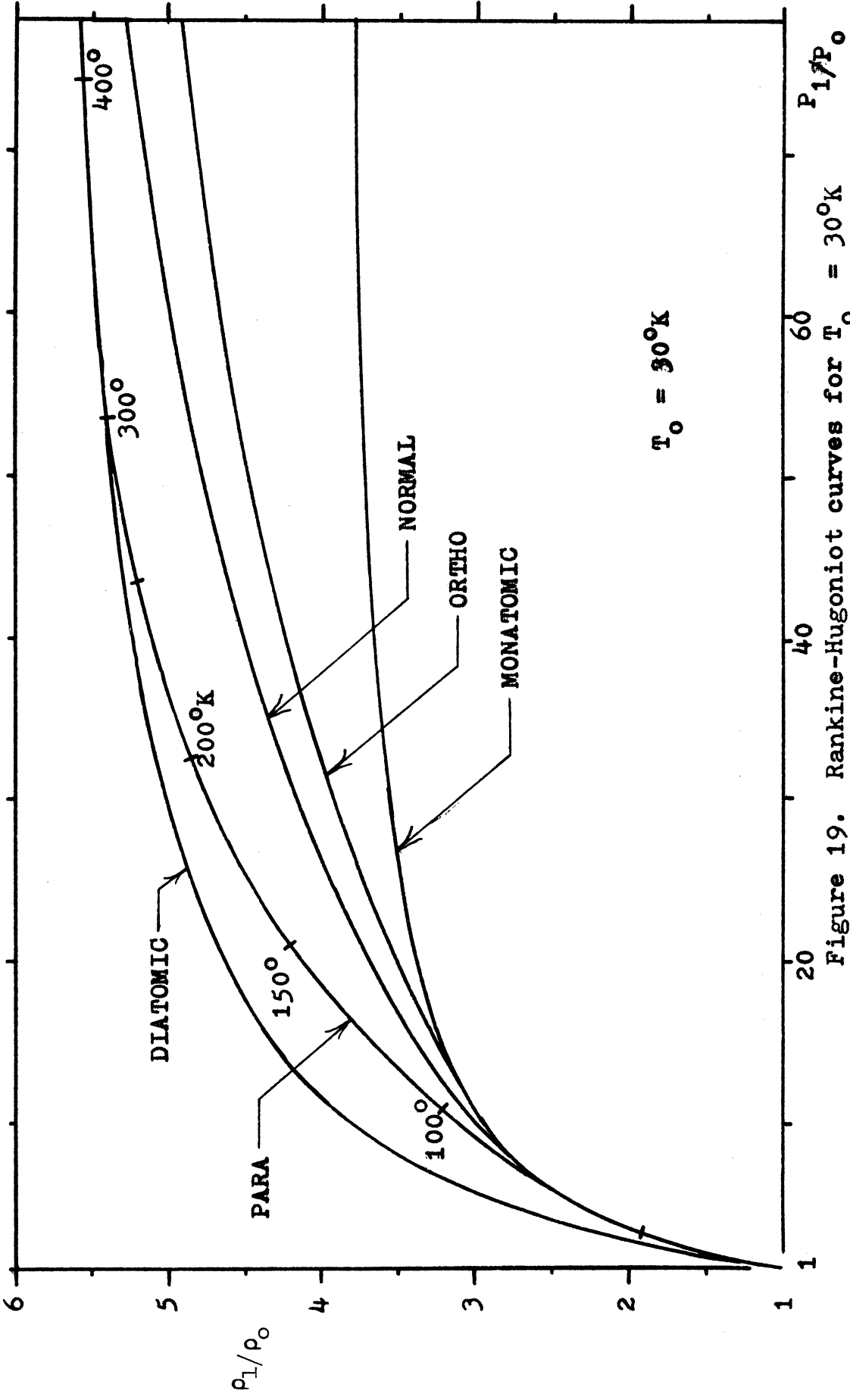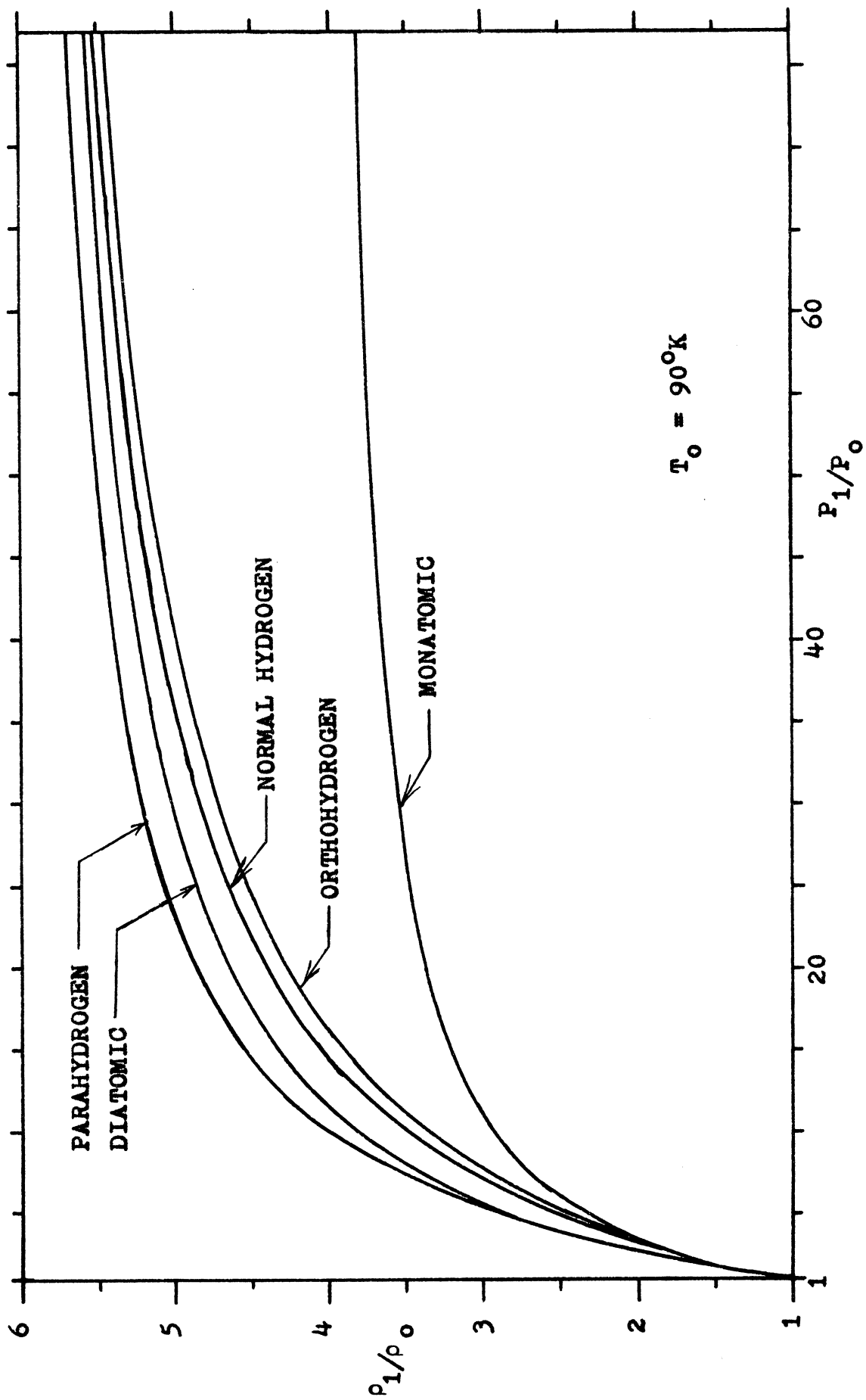
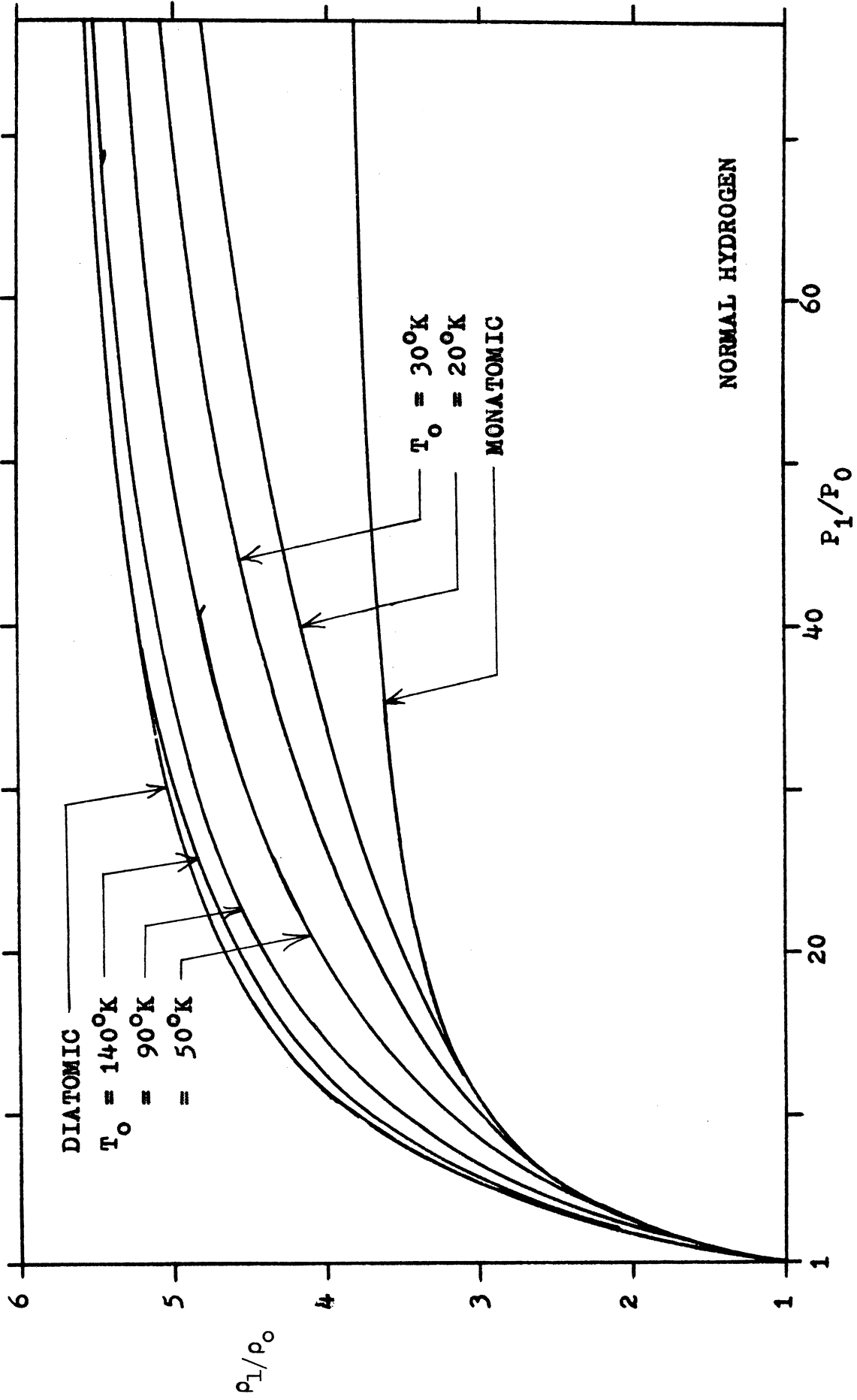Figure 20. Rankine-Hugoniot curves for $T_o = 90^{\circ}K$

Figure 21. Rankine-Hugeniot curves for normal hydrogen for several initial temperatures
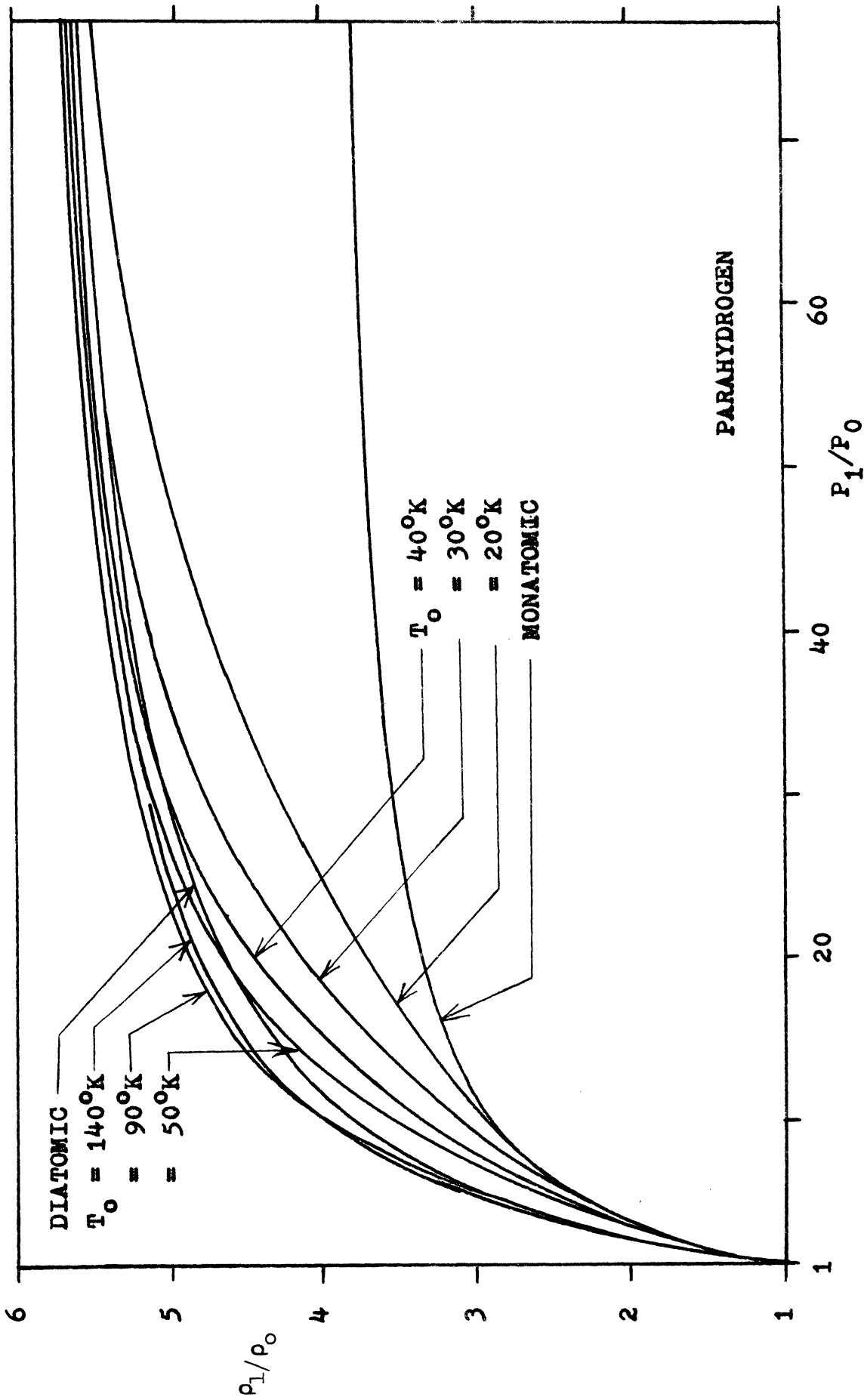
Figure 22. Rankine-hugoniot curves for parahydrogen for several initial temperatures

CHAPTER III

EXPERIMENTAL EQUIPMENT AND MEASUREMENT TECHNIQUES

1. Shock Tube Description

A schematic view of the cooled shock tube is shown in
Fig. 23. The 4' 1" long driver section is built of round
3" I.D. type 304L stainless steel tubing of $\frac{1}{2}$" wall thick-
ness. The 8' 2" long expansion section is made of round
3" I.D. type 6061 aluminum tubing of 3/4" wall thickness.
Both tubes are honed to give a very smooth inside surface.
Aluminum is used for the expansion section to insure temp-
erature uniformity. It is light and thick enough to allow
a single-piece construction. The test section windows are
machined directly into the tube. The flangeless design
minimizes the possibility of vacuum leaks and, at the same
time, simplifies the design of the cooling tubes. This type
of construction is very economical.

Liquefied gases are used to cool the shock tube. Liquid
nitrogen is used to reach temperatures as low as 80°K, and
for lower temperatures liquid helium is used. After leaving
a reservoir located between the shock tube and the outer
casing, the liquid (and subsequently gaseous) coolant flows
back and forth through 3/8" diameter hard temper copper
tubing fastened tightly to the shock tube by means of copper
straps. Apiezon "N" grease is smeared along the copper tubes
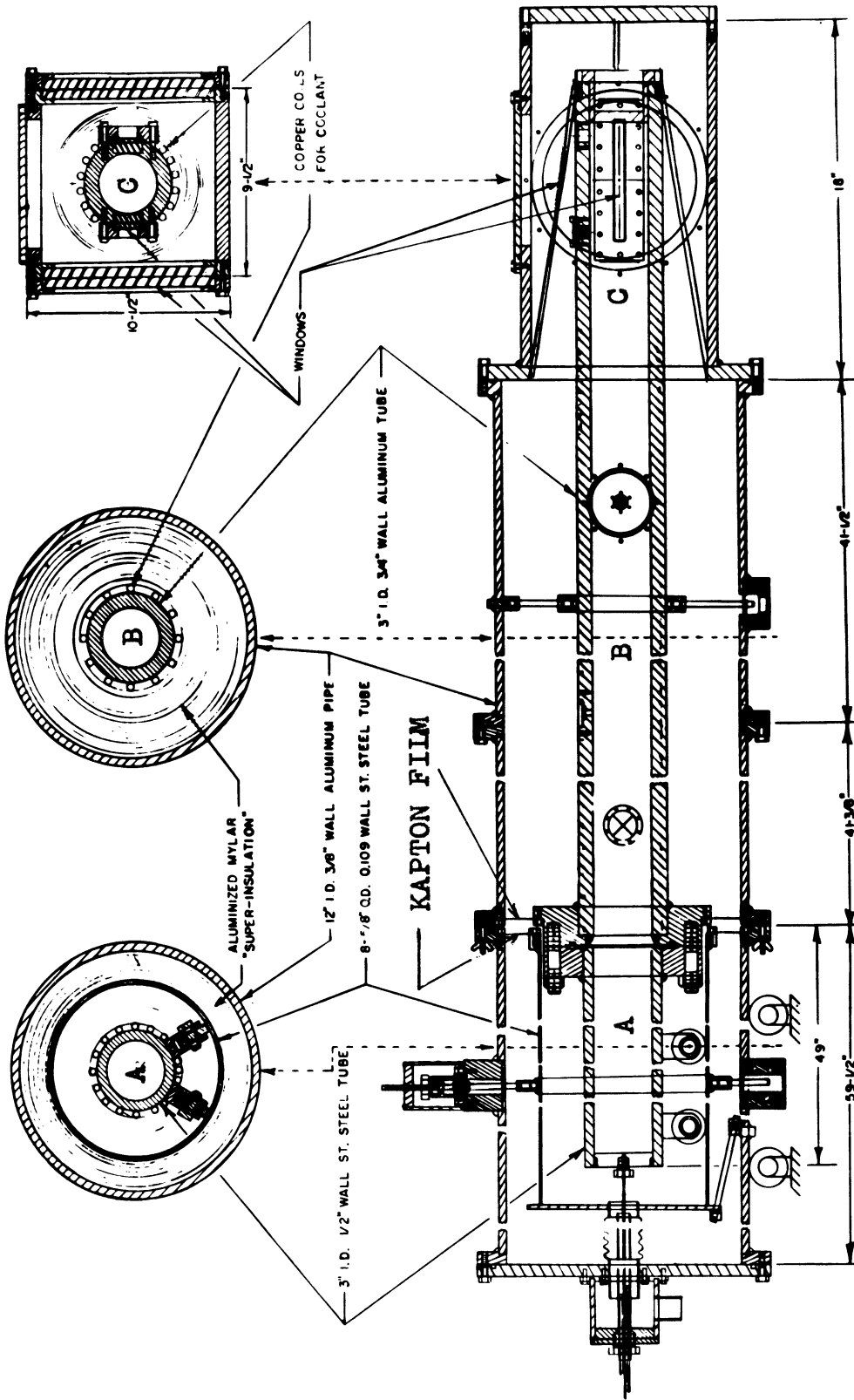to improve the thermal contact with the shock tube. A view

Figure 23. Schematic view of cooled shock tube

A driver section

B expansion section

C window configuration

of the shock tube, liquid reservoir, and copper tubing is shown in Fig. 24. The shock tube is wrapped with 80 to 100 layers of $\frac{1}{2}$ mil crinkled aluminized mylar superinsulation[*] and is suspended inside a 12" diameter aluminum tube by means of $\frac{1}{4}$" diameter nylon rods (see Fig. 25). The space between the two tubes is evacuated to less than 0.5 microns pressure to form a cylindrical dewar. A Consolidated Vacuum Company model MCF-300 vacuum diffusion pump is used in conjunction with a Welch Duo-Seal model 1402 mechanical pump. A liquid nitrogen cold trap is used between the diffusion pump and the insulation jacket. Fig. 27 shows a picture of the assembled shock tube.

Vacuum and pressure connections to the main shock tube must be made in such a way as to minimize heat leaks from the outer aluminum tube. Thus the main vacuum valve (which must fit flush with the inner shock tube surface when it is closed) is mounted directly onto the inner tube and operated by means of a detachable valve stem (see Fig. 28). The vacuum line between the main vacuum valve and the outer tube is made of an 8" length of thin $1\frac{1}{2}$" O.D. stainless steel flexible hose. A Cenco-Supervac OD-25 diffusion pump with a Welch Duo-Seal model 1405 mechanical pump is used to evacuate the shock tube. The high pressure gas is introduced

---

[*]Product of The Norton Company, Winchester, Mass.
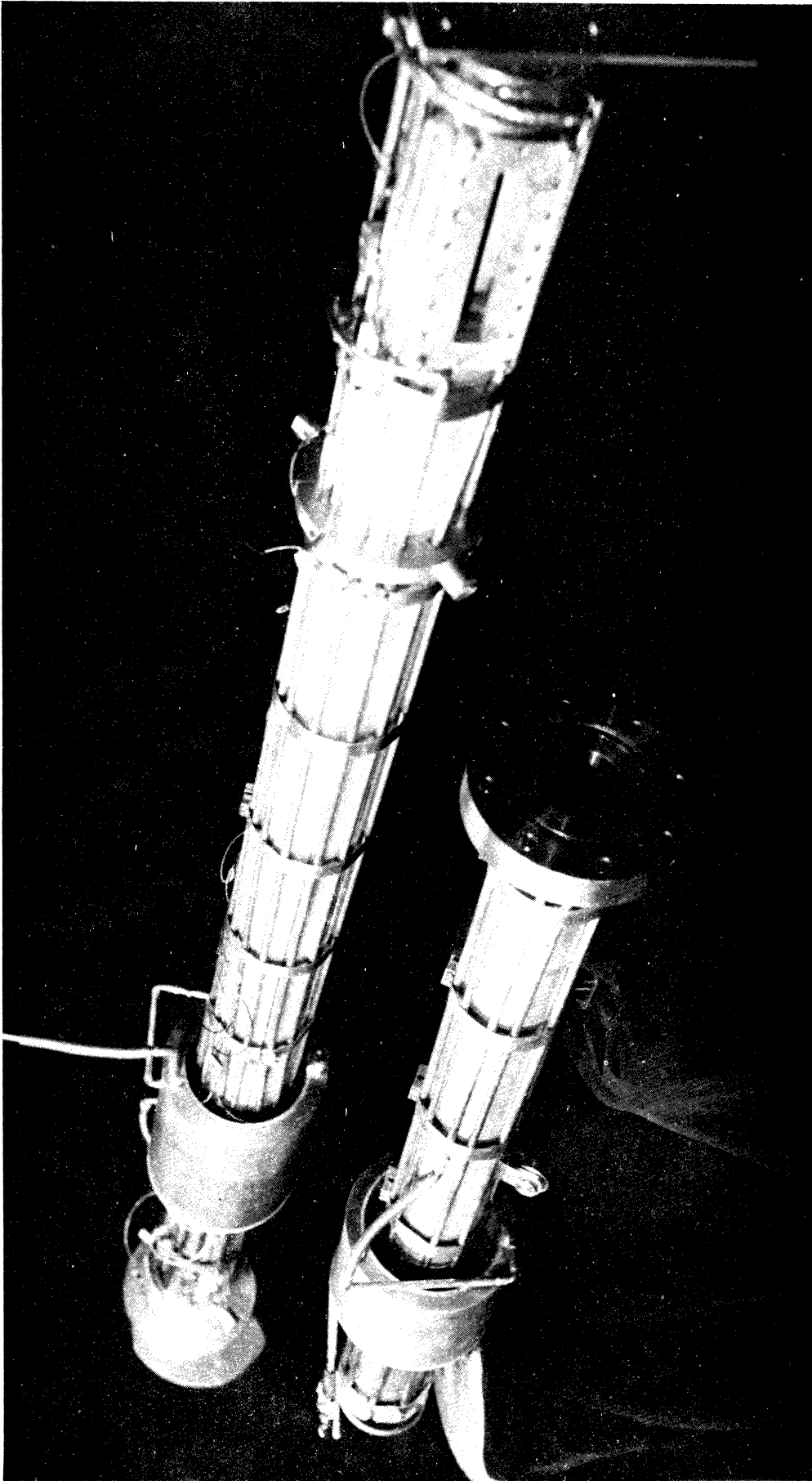
Figure 24. Shock tube with attached cooling system before suspension inside outer casing

upper tube - expansion section

lower tube - driver section
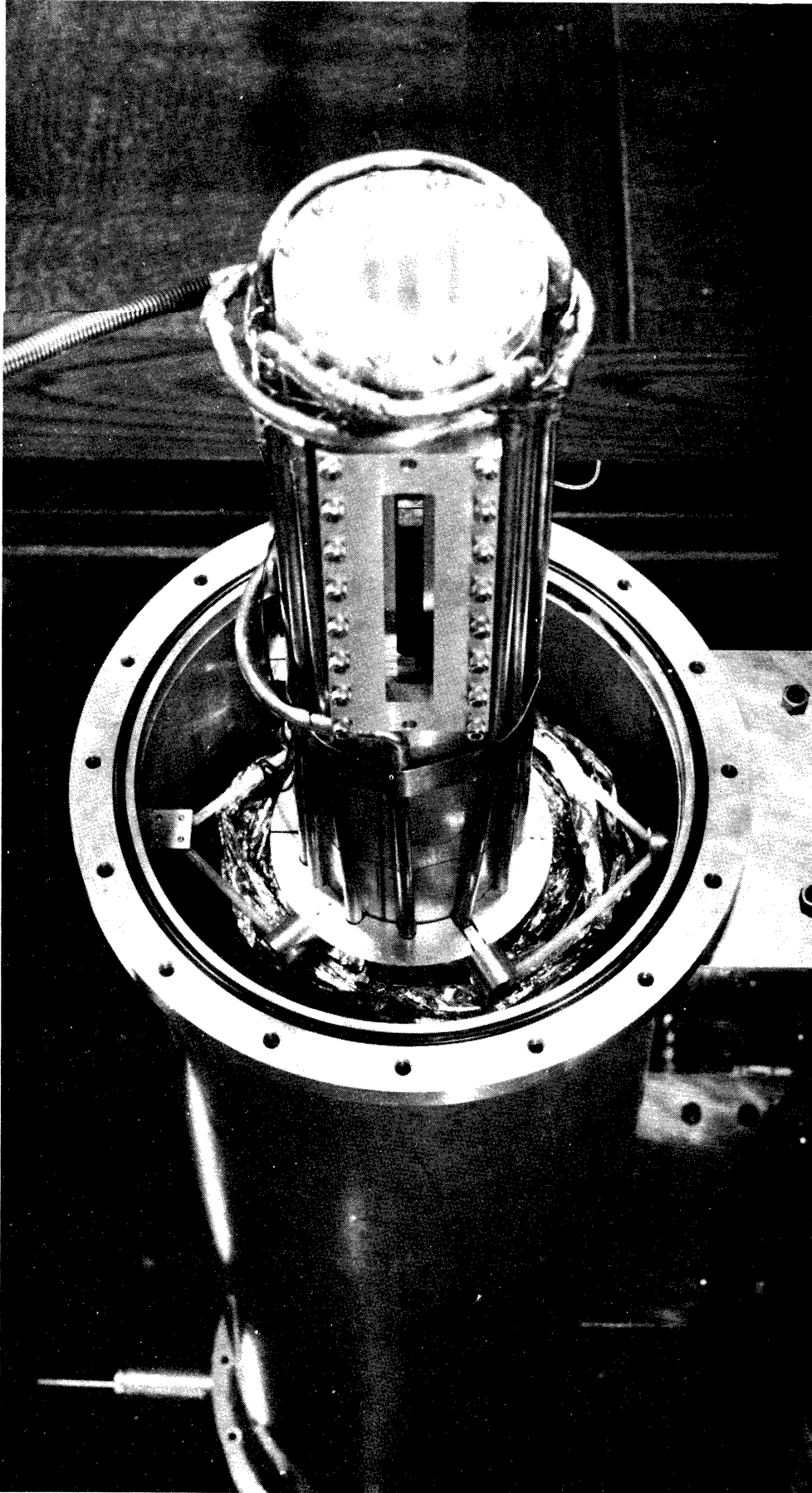
Figure 25. View of partially assembled shock tube showing aluminized mylar wrapping, nylon rod supports, and rectangular test section windows
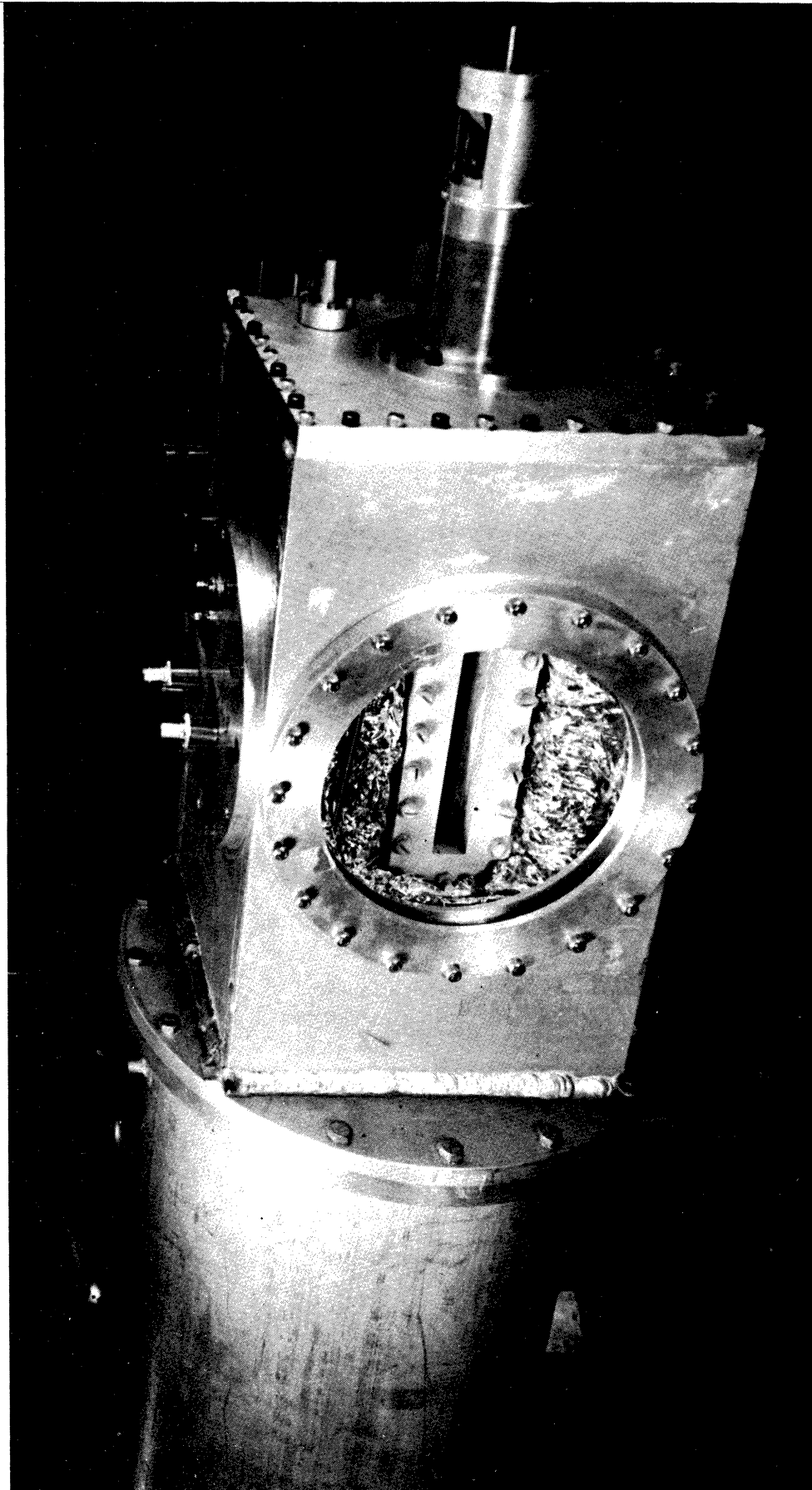
Figure 26. Assembled test section
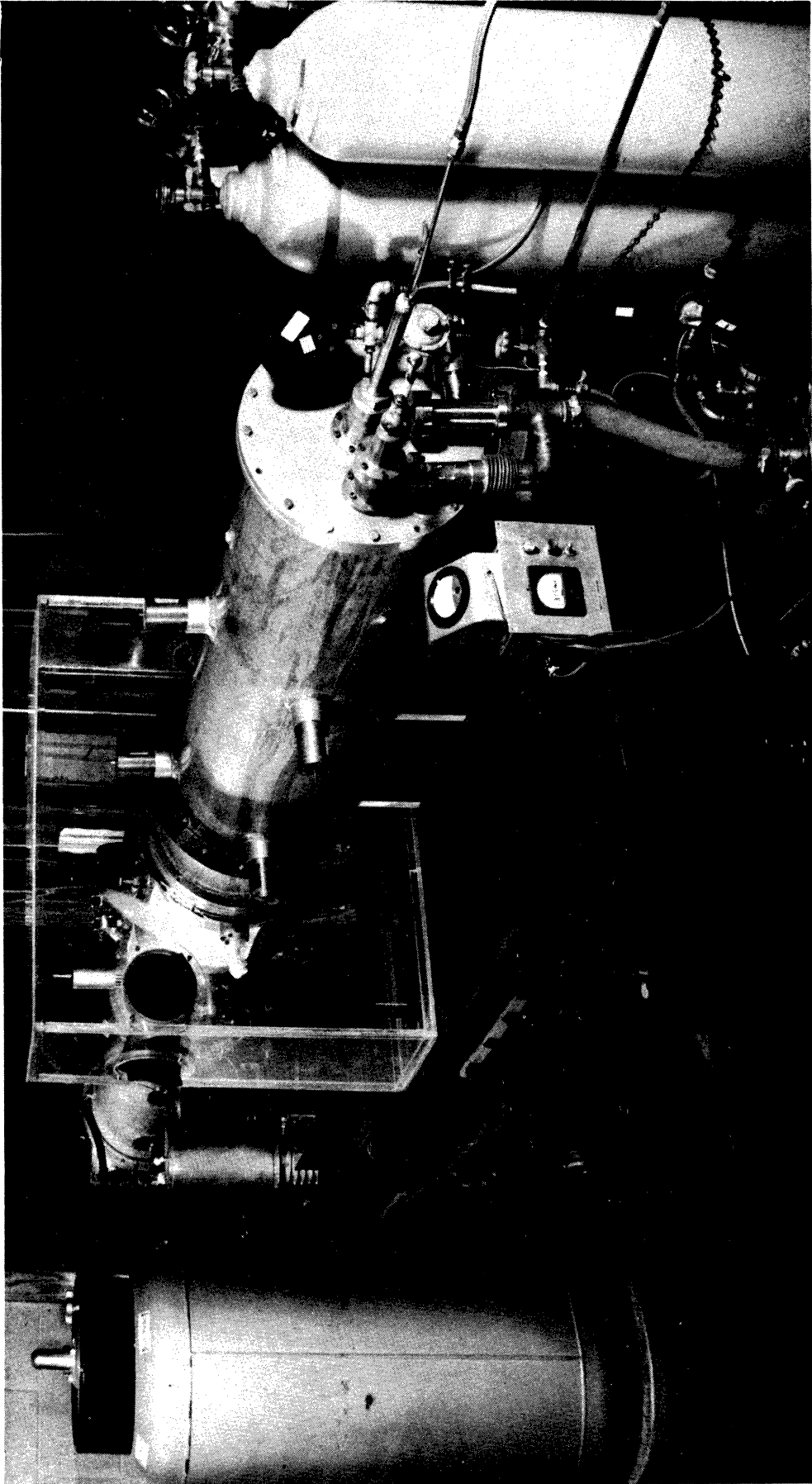
Figure 27. Assembled shock tube
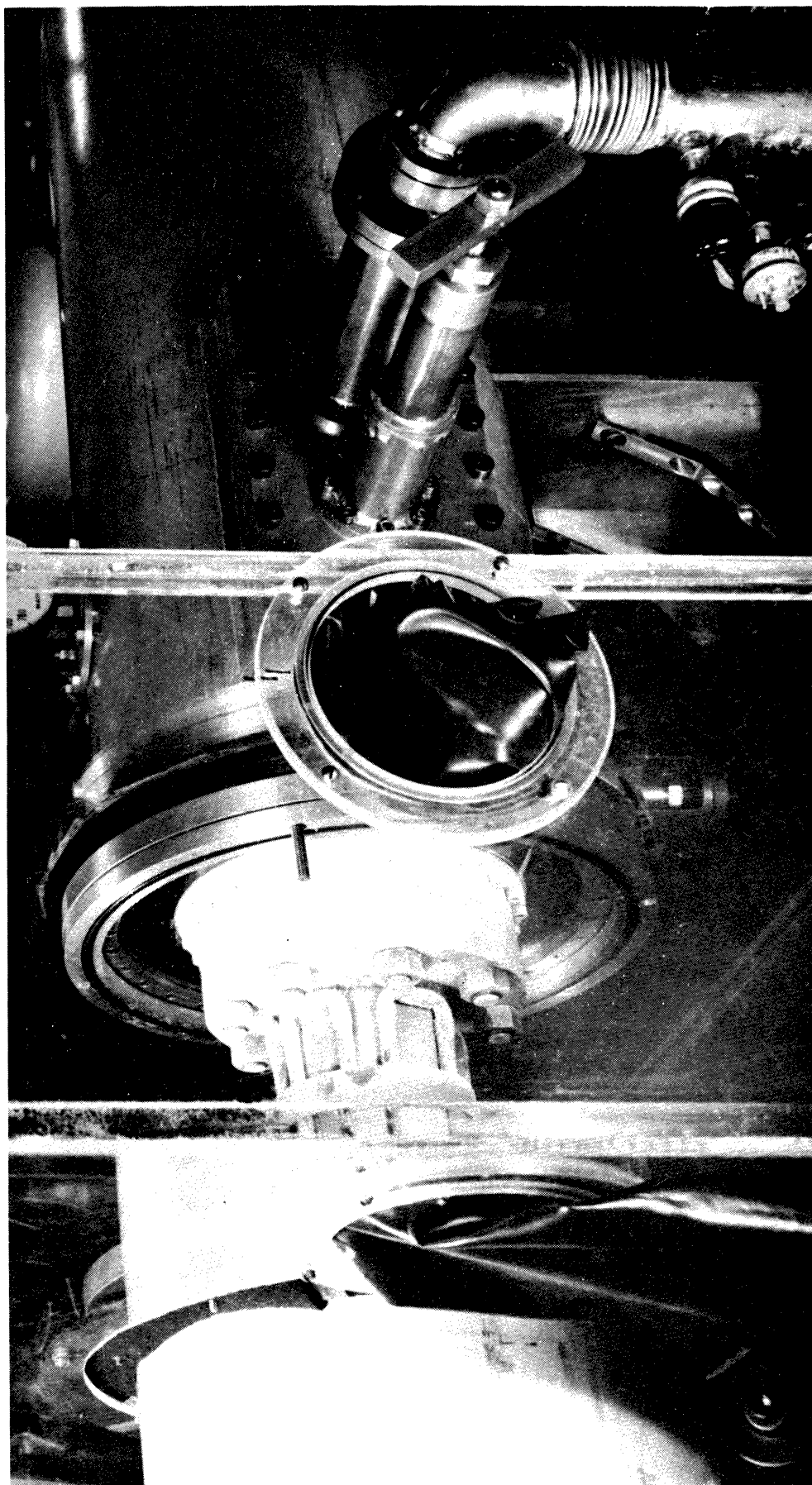
Figure 28. Cryogenic shock tube with opened outer casing
Note the annular Kapton film partition and the diaphragm changing chamber

into the driver section through a 3' long piece of ¼" O.D. x 1/8" I.D. stainless steel tubing. A thin-walled ¼" O.D. stainless steel tube, connected to the end of the expansion section, prevents recoil when the shock tube is fired.

After each shot in the shock tube the burst aluminum diaphragm, which separated the driver and expansion sections, must be replaced. This is accomplished while the shock tube remains cold. This tube cannot be exposed to air since water vapor, oxygen, nitrogen, and other atmospheric gases will condense on it. Thus a plexiglas dry box is built around the shock tube opening as shown in Figs. 27 and 28. The diaphragm is changed using long rubber gloves to provide a vapor barrier. The rubber gloves are covered with a pair of cotton or wool gloves to protect against the cold. A constant flow of cold dry nitrogen or helium is used to flood the box during the replacement process. This gas is supplied by the coolant exhaust.

Provision must be made to maintain high quality thermal insulation between the shock tube and the outer casing while the diaphragm is being replaced. Since the cylindrical space between the two tubes must be evacuated to achieve the insulation quality necessary for this experiment, the vacuum jacket is constructed in such a way that vertical partitions are inserted between the inner and the outer horizontal tubes. These partitions permit the sustaining of a longitudinal cylindrical vacuum insulation chamber between the shock tube and the outer chamber at all times. This allows the area

immediately adjacent to the diaphragm to be brought up to atmospheric pressure in order to replace the diaphragm after each shot, while still maintaining high quality vacuum insulation over the remaining shock tube surface area.

Each vertical partition is a 5 mil thick 2" wide annulus of Dupont "Kapton" Polyimide ("H") film. This material is chosen since it is very strong, withstands very low temperatures, and adds only a very small heat leak between the tubes. The film is sealed to the inner and outer tubes using thin flanges as shown in Fig. 29. These flanges have ridges machined onto them to concentrate the force against the "H" film and help to make the vacuum seal. The assembled parts can be seen in Fig. 28. This seal is sometimes more easily made vacuum-tight if a thin layer of teflon film is used underneath the "H" film layer.

Two thin-walled stainless steel tubes are used to support the inner tube against the atmospheric pressure which exerts a force of approximately 2000 pounds on it (and the "H" film annulus) when the area adjacent to the diaphragm is filled with nitrogen or helium gas during the process of changing a diaphragm. These tubes are shown in the schematic diagram in Fig. 23. After the diaphragm is changed, the inner chamber can again be evacuated to provide additional insulation.

It should be noted that the cylindrical vacuum chamber provides a vacuum space between the shock tube windows and the viewing windows on the outer tube. This allows the

① ALUMINUM OUTER CASING
② DUPONT KAPTON FILM
③ VACUUM SEAL FLANGES
④ CRINKLED ALUMINIZED MYLAR
⑤ TEFLON O-RING
⑥ KNIFE EDGE HIGH PRESSURE
                    SEAL
⑦ ALUMINUM DIAPHRAGM

DRIVER SECTION

EXPANSION SECTION

AXIS OF CYLINDRICAL SYMMETRY
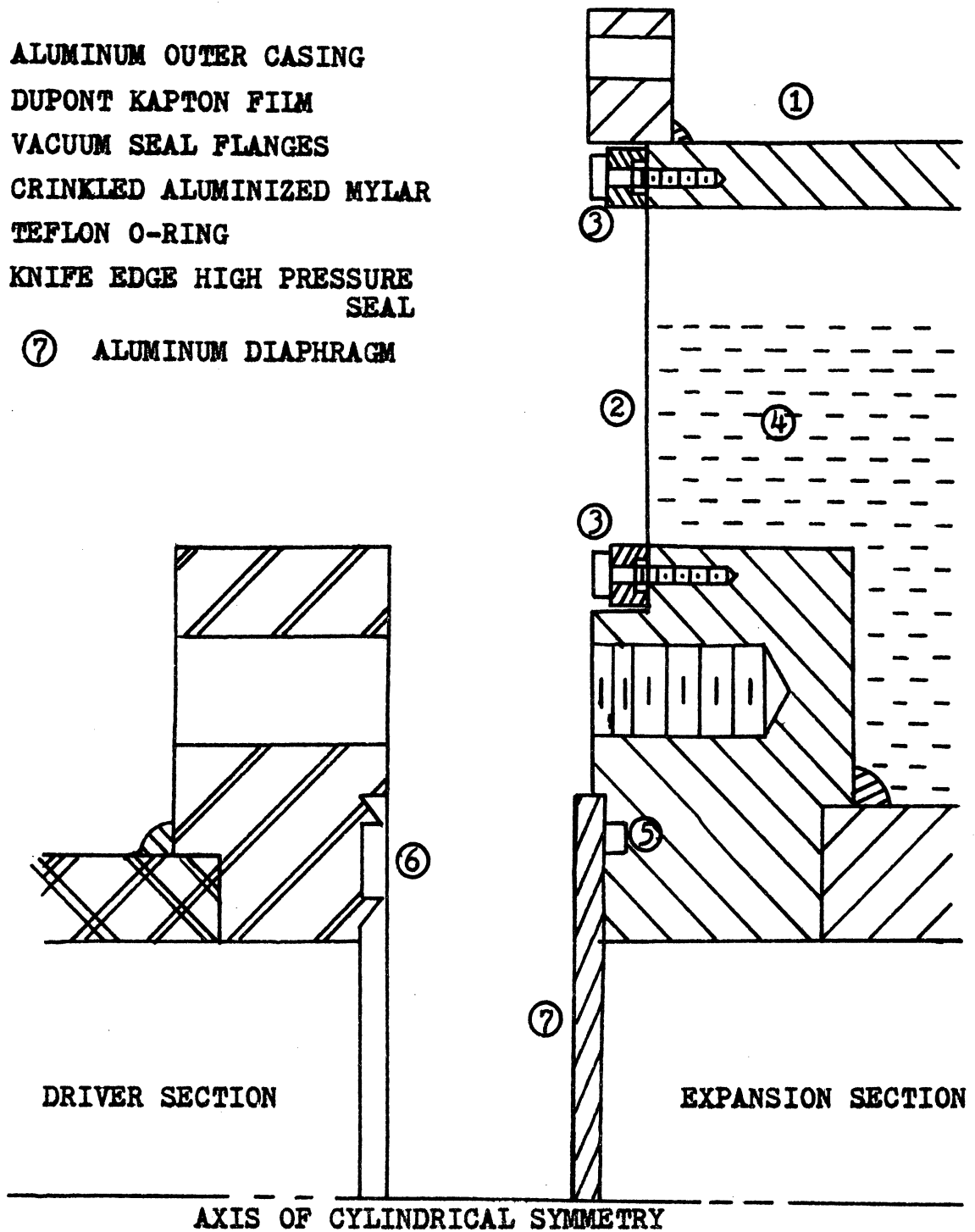
Figure 29. Full size drawing of diaphragm section

outer window to remain at room temperature and thus eliminates condensation and air current disturbances which would interfere with the optical measurements (see Fig. 26).

Pressure and vacuum seals of the diaphragm, flush valve, and pressure gauge to the cold inner tube are accomplished by use of knife edge seals, teflon O-rings, and indium wire tightly squeezed between matching surfaces. These are all well-known low temperature techniques. Attempts to seal rectangular glass windows using teflon O-rings were not very successful. Large pressure was needed to obtain a vacuum seal and this often broke the windows. The windows had to be retightened after each temperature cycling, often breaking them. Finally, a method similar to that described by Lipsett[19] was used. 3/16" thick pyrex round glass windows were tinned with indium alloy solder using an ultrasonic soldering iron. The matching metal surface was also tinned. A 1/16" diameter soft pure indium wire was squeezed between these two surfaces after being wetted with concentrated hydrochloric acid. This technique is described by Zipfel[20]. A diagram of the window seals is shown in Fig. 30. A glass spacer is necessary so that the windows fit flush with the inner surface of the shock tube. The threaded brass ring is tightened until the indium wire is squeezed flat. It is very easy to make this vacuum seal and no windows have yet been broken.
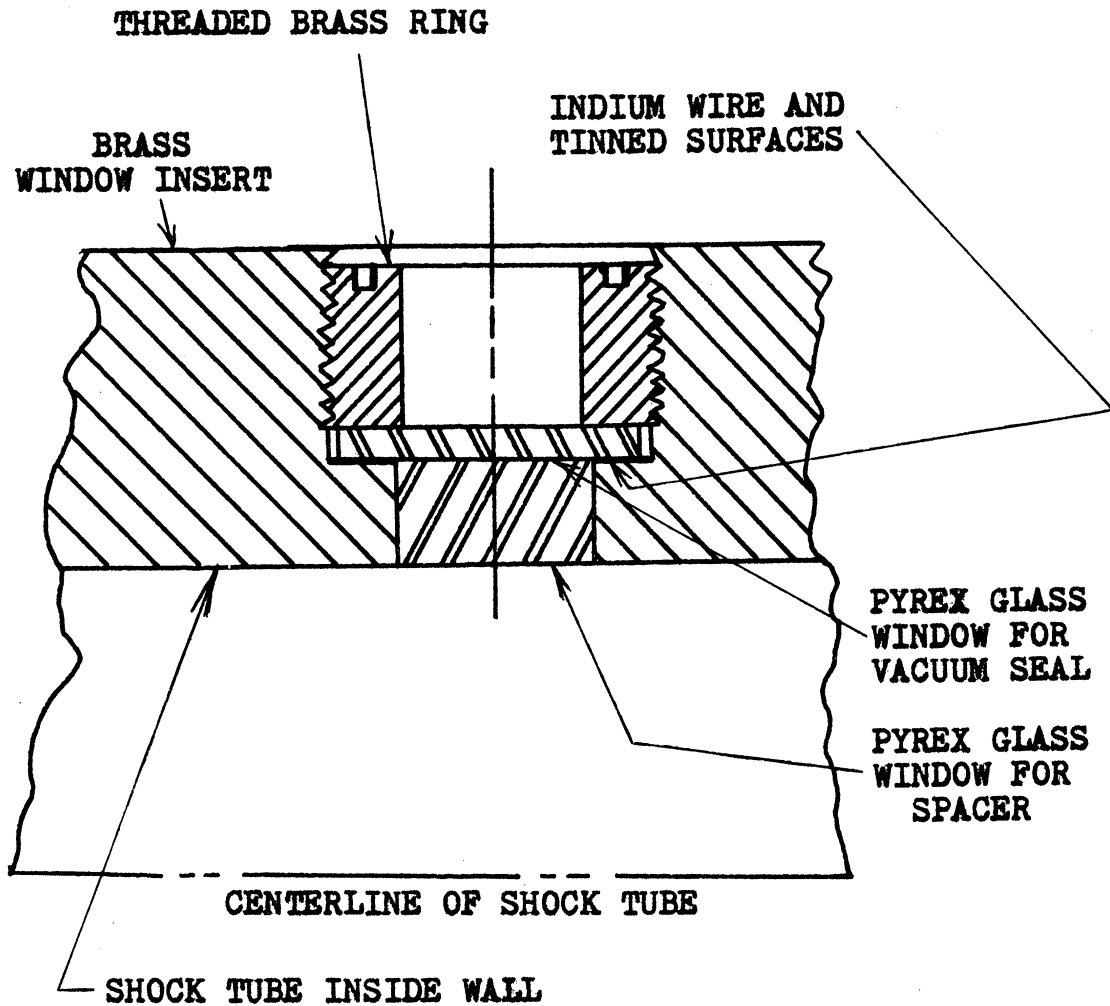
Figure 30. Window configuration and seal for round windows

A great deal of difficulty was initially encountered due to the condensation of water vapor inside the shock tube. The tube had to be rewarmed after each shot to pump off the ice that had coated the shock tube windows and prevented further optical measurements. The water vapor was due to impurities in the high pressure gases used in the compression section, and the following procedure was used to dry the gas.

Before entering the shock tube the high pressure gas is confined in a $4\frac{1}{2}$" diameter, 9" high brass cylinder immersed in liquid nitrogen. The cylinder is partially filled with Linde 4A molecular sieves. The gas is left in the cylinder for several minutes before being let into the shock tube. Even with this procedure it is necessary to start with very dry compressed gases having water vapor content less than about 2 ppm. Lower purity gases are not usable even with the cold trap. This may be due to ice crystals being formed and then being carried into the shock tube by the flow in spite of the tight pyrex wool packing used in the cold trap exit tube. Linde "ultrapure" grade and Liquid Carbonic "pure" grade hydrogen and helium gases are found to work very well and add no water vapor to the shock tube when the trap described above is used. Most other gases, including those labeled "less than 5 ppm water vapor content" are not usable due to their wetness. It was suggested to the author that passing the gas slowly through a large container filled with activated molecular sieve

pellets at room temperature would dry commercial grade gases
well enough that they could be used. This was tried but
with no success.

In order to prepare pure parahydrogen for use in these
shock studies the apparatus pictured in Fig. 31 was constructed.
The catalyst container, reservoir, and connecting tube are
initially filled with pure dry hydrogen to a pressure of
about 1000 psi. The tube is then lowered into a liquid
helium dewar and suspended in the cold gas above the liquid
phase. The gas in the reservoir then condenses into the
catalyst container and is converted to parahydrogen.
The temperature is monitored by means of the vapor pressure.
After several minutes the conversion is complete and the
glass flask can be filled with parahydrogen that, according
to Table III, is better than 99% pure. The valves are then
closed and the apparatus is removed from the helium dewar.
The "Apachi" catalyst used for this conversion process was
generously provided by Mr. John F. Kucirka of Air Products
and Chemicals, Inc., Allentown, Pennsylvania. It is about
23 times more active than iron hydroxide gel which is in
turn many times more active than activated charcoal.

The temperature is measured at several points along
the shock tube using copper-constantan thermocouples. The
wire leads are wrapped and epoxied around a solid copper
cylinder which is attached to the cold shock tube. The
leads then feed through the outer casing vacuum fittings
to a liquid nitrogen reference bath and a potentiometer.
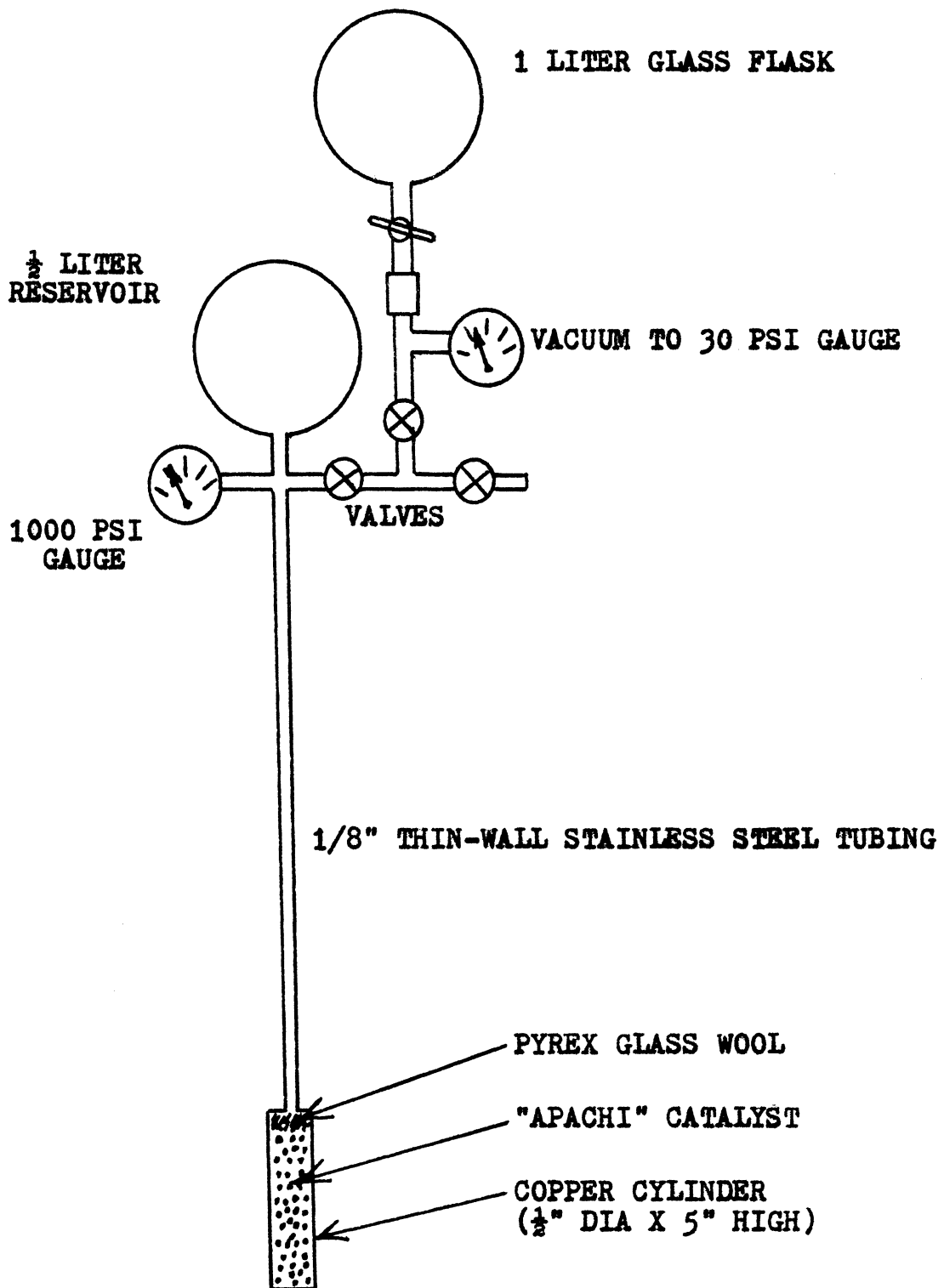
Figure 31. Aparatus for converting ortho to parahydrogen

The use of long thermocouple leads and many windings around the brass cylinder insures that the junction reads the actual shock tube temperature. The thermocouple voltages are read with a Leeds and Northrup potentiometer to $\pm$ 1.0 microvolts. Initial shock tube temperatures can be measured to within $\pm$ 0.5°K.

2. Instrumentation and Experimental Set-Up

In order to determine a point on the Rankine-Hugoniot curve the shock speed and at least one other quantity must be measured. The most accurately measurable quantity is the final density behind the shock. This can be determined using an interferometer. Another measurable quantity is the pressure. It can be found by use of a piezoelectric pressure transducer. However, the accuracy of this type of measurement is limited to about 8%. There is no direct method available to measure the final temperature. The nonclassical behavior of the gas due to energy being absorbed by the internal degrees of freedom makes itself known by a decrease in temperature and an increase in density. Pressure is affected very little. This was shown in Figs. 13 to 18 of Chapter II. Since the density change is the most accurately measurable quantity and, furthermore, is the parameter most sensitive to the

nonclassical behavior of the gas, it is used to monitor the Rankine-Hugoniot predictions. The pressure was also measured and provides a direct check on the density and shock velocity measurement results.

We are fortunate to possess a very good Mach-Zehnder interferometer, built originally by Dr. E. B. Turner in 1952-53 with financial support from the U. S. Navy. The mirrors, flat and smooth to $\lambda/20$, were a gift of the U. S. Naval Gun Factory. The interferometer is of conventional $30°$ - $60°$ Kinder design (see Fig. 32). The 9" interferometer elements provide an 8" diameter working beam. Although less than a 2" diameter beam is necessary for the interferometric studies, the large mirrors conveniently allow the simultaneous use of the same instrument for a 7" wide schlieren beam which is used to trigger the scopes and to measure shock speeds. Each interferometer element is provided with ball bearing mounts and built into a heavy box of $\frac{1}{4}$" thick welded steel plate construction. Access and beam holes are cut in the ends and sides. The box is mounted on rubber wheels to isolate the optical system from external vibrations. All mirrors are provided with micrometer adjustments except for mirror #2, which is coupled by a fine gear arrangement to small electric motors. These motors can be actuated by remote control. This is very convenient for making final adjustments in fringe orientation although it is often troublesome and time-consuming for making coarse initial adjustments of the optical system. Further details concerning
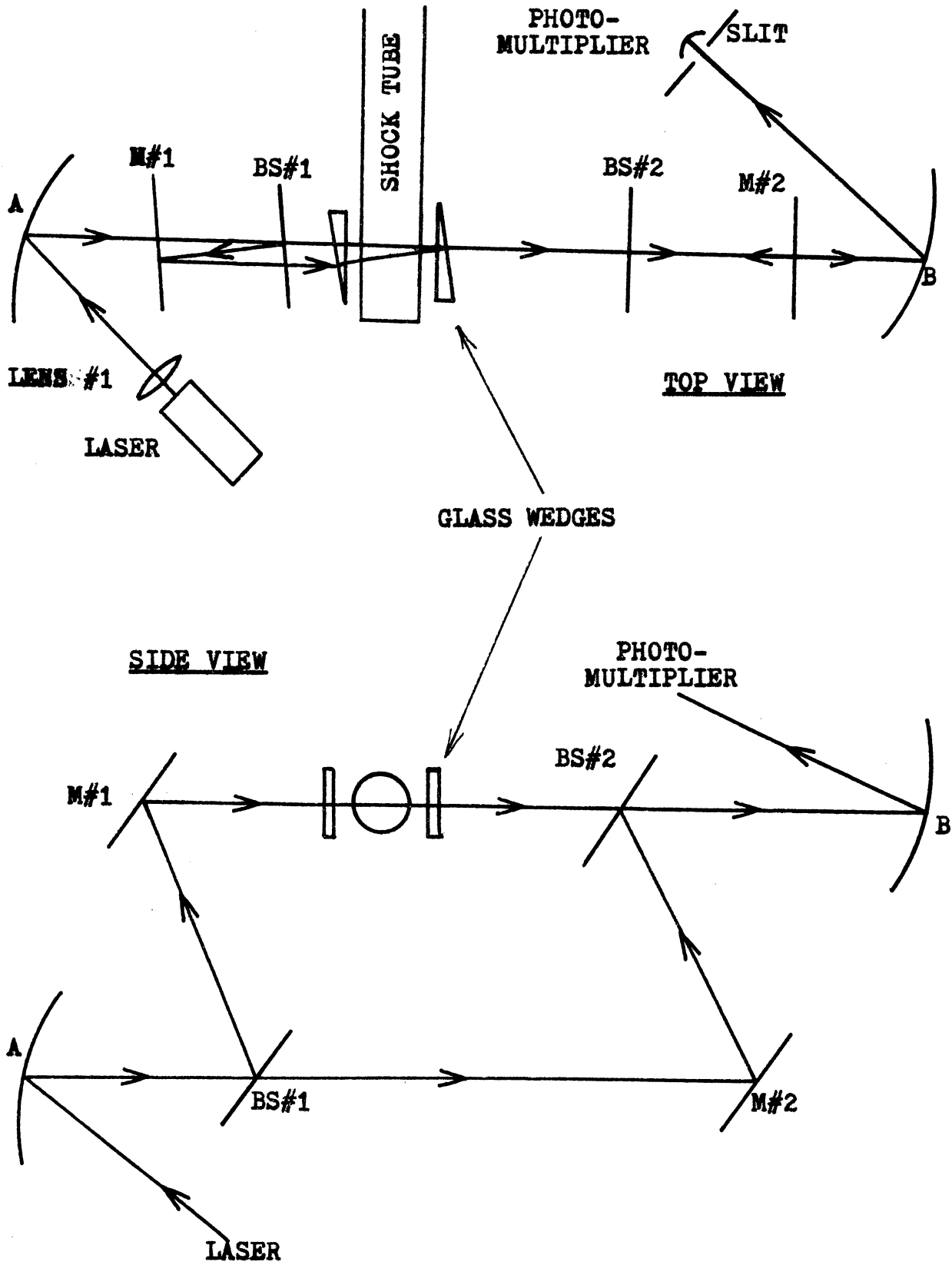
Figure 32. Schematic drawing of interferometer optics

this interferometer can be found in the Ph. D. thesis
of Alfred Curtis Hunting[21].

Instead of the usual flashlamp and photographic tech-
niques for recording the fringe shifts across the shock,
it is convenient to use a gas laser and a photomultiplier
recording system. A Spectra Physics model 132 helium-neon
gas laser having a power of 1 milliwatt, a wavelength of
6328 $\overset{o}{A}$, a beam diameter of 0.8 millimeters, and a beam
divergence of 1.0 milliradian is used as the light source.
A R.C.A. 7265, fourteen stage photomultiplier having an
S-20 spectral response is used to read the light intensity
of the interference fringes. A 6328 $\overset{o}{A}$ interference filter
is placed in front of the phototube to protect it from stray
light and accidental exposure to strong light sources. The
output of the photomultiplier at the time of the shock
passage is read on either a model 535A or a model 543A
Tektronix oscilloscope and the resulting trace is photographed
using a Polaroid camera. This results in several advantages.
The interferometer is extremely easy to set up and adjust
when the laser is used. The resultant data are quickly
and conveniently collected with no need of tedious film
processing and measurement. This method also automatically
eliminates light intensity problems which are so common with
photographic techniques. Only moderate quality windows are
necessary since requirements of fringe spatial uniformity
are minimal.

Instead of the slow and demanding process of aligning the interferometer mirrors using conventional light sources, such as the "technique of near and far fringes"[21,22], the use of the narrow beam of a gas laser allows quick and easy alignment. No more than ten minutes is required from start to finish no matter how far the mirrors initially are out of adjustment. One simply aims the laser, without lens #1, (see Fig. 32) at the center of parabolic mirror A. This mirror is then adjusted so that the beam passes through the center of beam splitter #1 and hits mirror #2 in the center. Mirror #2 is then adjusted so that the beam hits beam splitter #2 in the center and this element, in turn, is adjusted so that the beam strikes the center of parabolic mirror B. This completes the layout of the reference beam. The other beam, obtained from beam splitter #1, is adjusted by use of this element and mirror #1 so that it strikes the reference beam at the second beam splitter and remains parallel to it. This is accomplished by successive adjustments of the #1 elements using two reference surfaces such as parabolic mirror B and the face of the photomultiplier tube. The two beams generally make two spots on each surface. Beam splitter #1 is adjusted so that the points of laser light coincide at the parabolic mirror. Mirror #1 is then adjusted so that the points coincide at the photomultiplier surface. After this is done there are again two spots of light on the parabolic mirror so the beam splitter must again be adjusted...etc. This is a rapidly converging process which soon results in

perfectly parallel and coincident beams. When lens #1 is inserted to obtain a wide beam of light, fringes are immediately visible on the photomultiplier surface. They are real and in focus everywhere from beam splitter #2 to infinity. This is in sharp contrast to the usual case involving conventional, (e.g. mercury arc) light sources where the fringes are virtual, lie only near a certain point in space, and must be brought into coincidence with the test section by additional mirror adjustments.

The function of the wedges is to incline the beam with respect to the shock front. This allows the photomultiplier to follow the fringe shifts through the shock since the density change is gradual and not sharp, as it would be with a beam that was parallel to the shock front. The interferometer is adjusted so that there are vertical fringes at the photomultiplier surface. This surface is located at the image plane of the test section. The photomultiplier sees only the light passing through a 0.006" x $\frac{1}{4}$" vertical slit (i.e. it sees only the light from a particular ray passing through the test section). Let this light correspond to part of a dark fringe. If the optical path of this ray changes due to a density change in the shock tube by half a wavelength of the light then the ray will change from dark to light. A gradual change in the optical path results in a gradual change of the light intensity at the photomultiplier slit. By counting these changes one can determine the total number of fringes and

the fraction of fringes shifted. It is then possible to deduce the density change by the relation

$$\Delta\rho = \frac{\lambda N_{fs}}{(n_o - 1) D}$$ (47)

where

N_{fs} = total number of fringe shifts

D = shock tube diameter

λ = wavelength of light used

$\Delta\rho$ = change in density in amagats[*]

n_o = index of refraction at S.T.P.

Thus a measure of N_{fs} during the passage of a shock front provides a direct measure of $\Delta\rho$ across the shock.

The shock speed must measured. Additionally, the oscilloscopes must be triggered just before the arrival of the shock so that the fringe shift information can be recorded. These requirements are met by means of a schlieren optical system. The optical set-up is shown in Fig. 33. The light source is an Osram HBO 100W/2 dc mercury arc lamp having an arc diameter of 1 millimeter and a brightness of 1700 cd./mm^2. This source is focused onto a 0.008" x $\frac{1}{2}$" vertical slit using a 3" diameter 2$\frac{1}{2}$" focal length quartz lens. The slit is located at the focal point of parabolic

---

[*]The density of a gas in amagats is the ratio of the gas density to the density of the same gas at S.T.P.
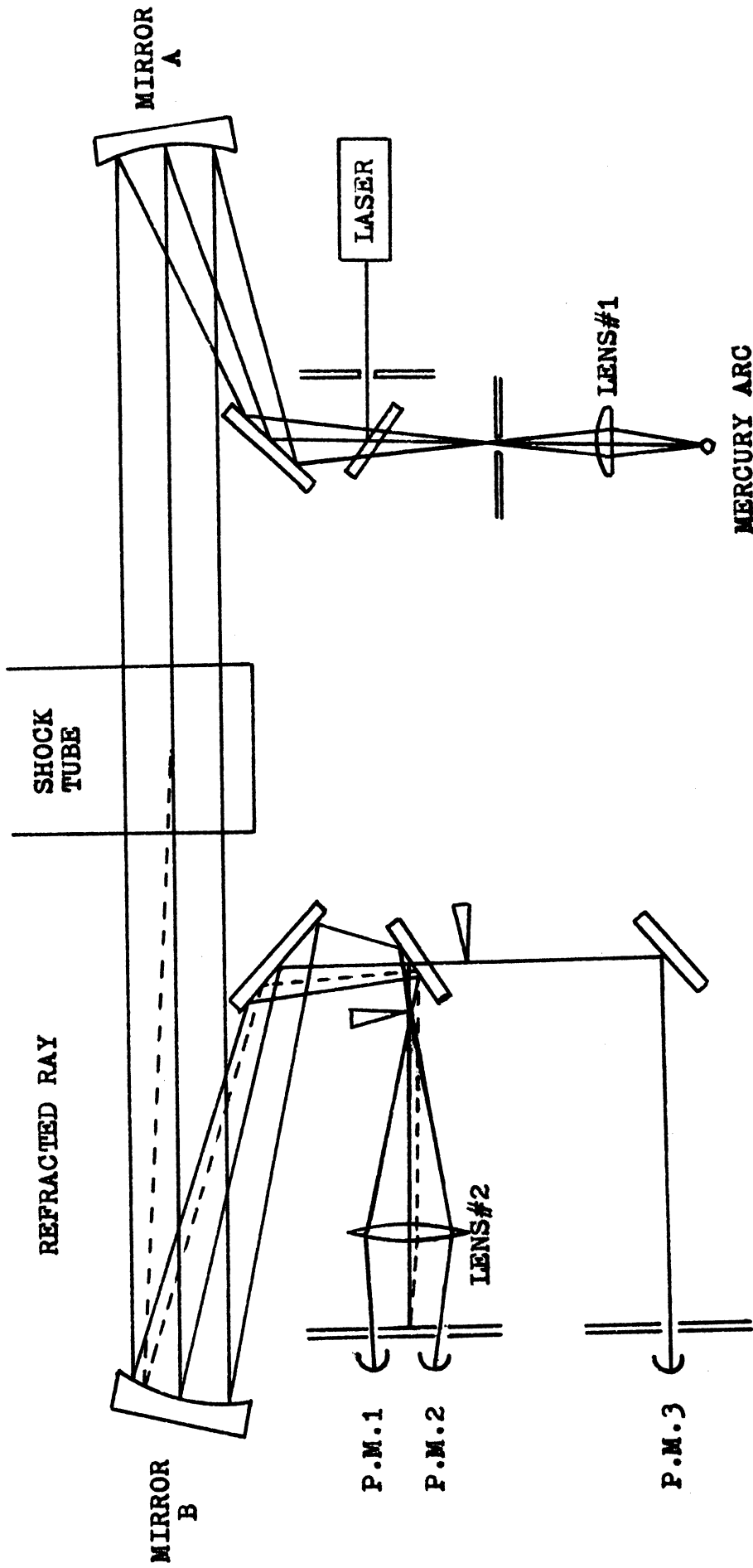
Figure 33. Schematic diagram of schlieren optical systems

mirror A so a parallel beam of light then goes through the test section. The image of the slit is focused onto a knife edge as shown in Fig. 33 using parabolic mirror B. Lens #2, in combination with this mirror, then focuses the image of the test section onto 0.040" x 3/4" vertical slits in front of photomultipliers #1 and #2. The insertion of the knife edge into the beam makes it possible to record the density gradients ocurring in the shock tube.

The principle of operation of the schlieren optical system will now be described with reference to Fig. 33. First note that light leaving the test section at any angle is brought back into focus at the photomultipler surface at its own image point (provided, of course, that it strikes parabolic mirror B). Furthermore it should be noted that the gradual insertion of the knife edge does nothing but uniformly change the intensity of the parallel light reaching the photomultipliers. However, the knife edge performs a very essential function for nonparallel light originating at the test section. Light that passes through a density gradient (e.g. a heat wave or a shock) is deflected from its parallel direction and moved either into or away from the knife edge, depending on the direction of the density gradient. This is shown in Fig. 33. The photomultipliers then see this density gradient as a decrease or increase in the light intensity. The change in intensity is directly proportional to the gradient of the density. This is how the passage of the shock is detected for scope triggering and shock speed measurement.
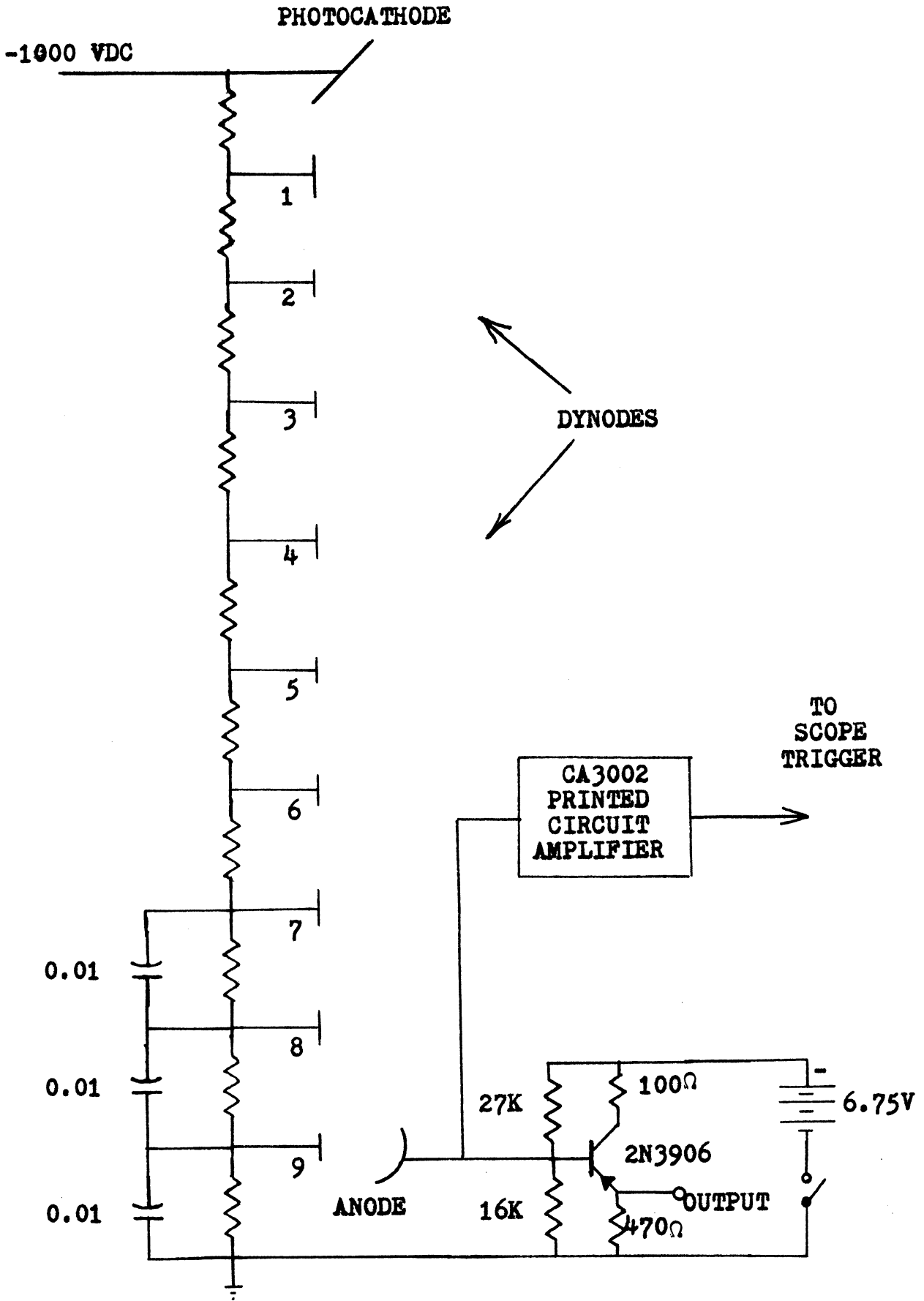
Figure 34. 1P28 photomultiplier and emitter follower circuits

When the shock image reaches slit #1, a signal is generated which triggers the oscilloscopes via an R.C.A. CA-3002 integrated circuit amplifier as shown in Fig. 34. The same signal is fed into a 2N3906 emitter follower circuit. This provides the photomultiplier with a low output impedance. The signal travels through about six feet of coaxial cable to a 5 tube 6AG5 amplifier. The output from this amplifier starts a 1 megahertz oscillator. An identical circuit is used from photomultiplier #2 to stop the oscillator when the shock image arrives at the second slit. The output of the oscillator is read on a scaler which thus gives the time of passage between the slits (see Fig. 35). Knowing the distance between the slits and the magnification factor of the optical system, one can easily compute the shock speed.

The pressure is measured by means of a Kistler* 606L pressure transducer and a Kistler* 504A charge amplifier. The transducer contains a pre-stressed quartz crystal. Changes in pressure cause a charge to be induced on the crystal. The transducer has a charge sensitivity of approximately 5 picocoulombs per psi of pressure and a rise time of less than 5 microseconds. The high impedance charge amplifier converts this charge output to a voltage which can be conveniently displayed on an oscilloscope. A Hewlett-Packard model 152A oscilloscope is used. It is triggered by a signal from the schlieren system just before the

---

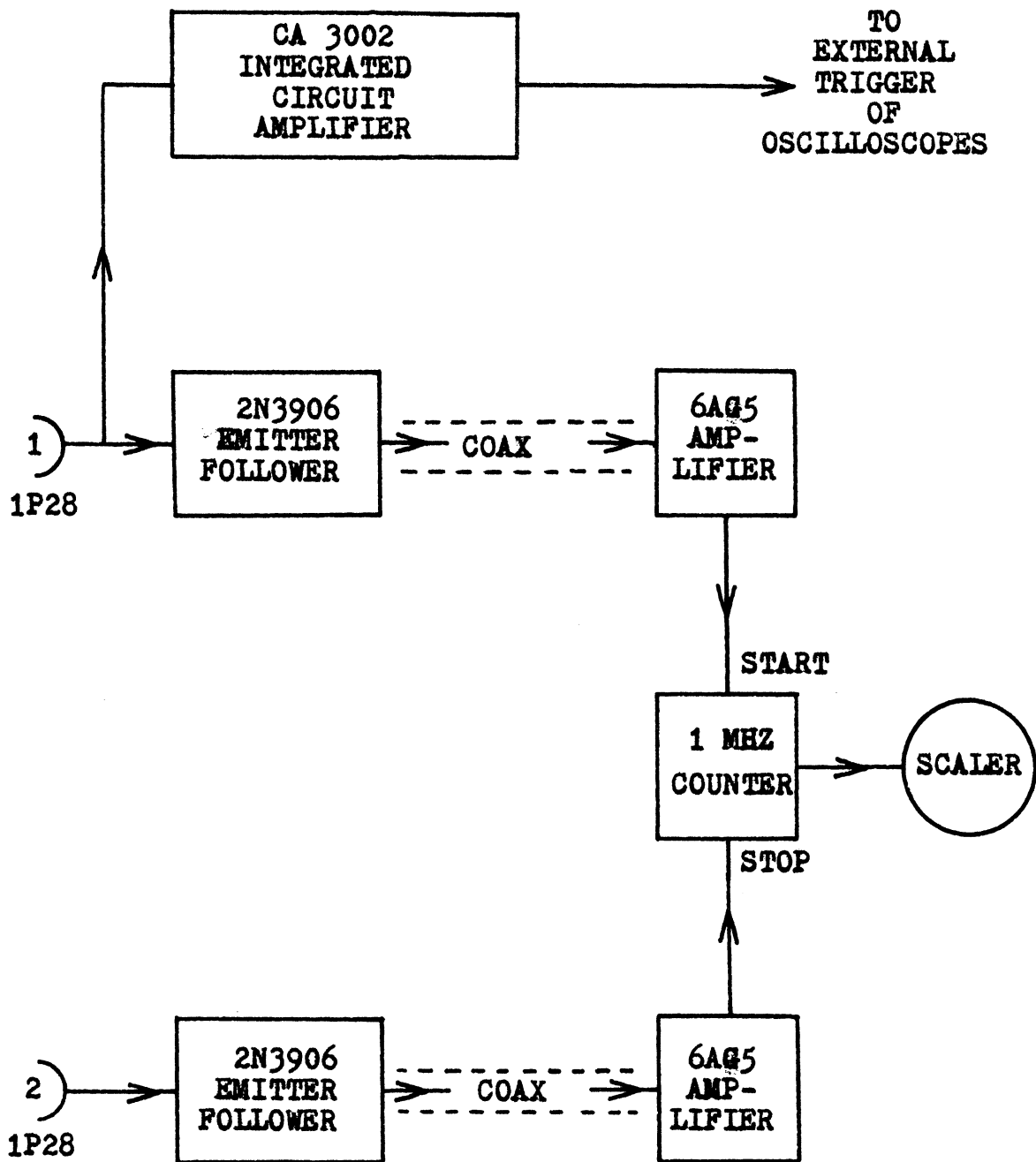*Kistler Instrument Corporation, Clarence, New York

Figure 35. Block diagram of shock speed measurement
and oscilloscope triggering electronics

arrival of the shock. The trace is photographed using a Polaroid camera.

In order to assure that low temperature shock waves and related flow regions are similar to those of their higher temperature counterparts, wave speed photographs are made using a rotating drum camera. Since these shocks are not luminous it is necessary to use a schlieren system to observe the properties of the flow regions. The optical arrangement is shown in Fig. 36. The light source is a General Electric FT-218 xenon flash lamp. It is powered by a 525 mfd. capacitor bank charged to 900 volts. Just before the arrival of the shock, the flash discharge is initiated by a 10.000 volt pulse from a 5C22 thyratron tube connected to the triggering electrode of the flash lamp. The discharge lasts for approximately 1000 microseconds and is fairly constant in intensity. The flash lamp is masked except for a 0.3 mm x 10.0 mm vertical slit located at the focal point of the parabolic mirror. A parallel beam of light travels through a 6" x 0.10" horizontal slit on one of the test section windows and is brought to a focus at the knife edge using a second parabolic mirror. A lens images the test section horizontal slit across a strip of Kodak type 2484 film (A.S.A. speed 2000) in a rotating drum camera. The drum revolves at speeds up to 12 000 r.p.m. and has a writing speed on the film of about 7 microseconds per millimeter.
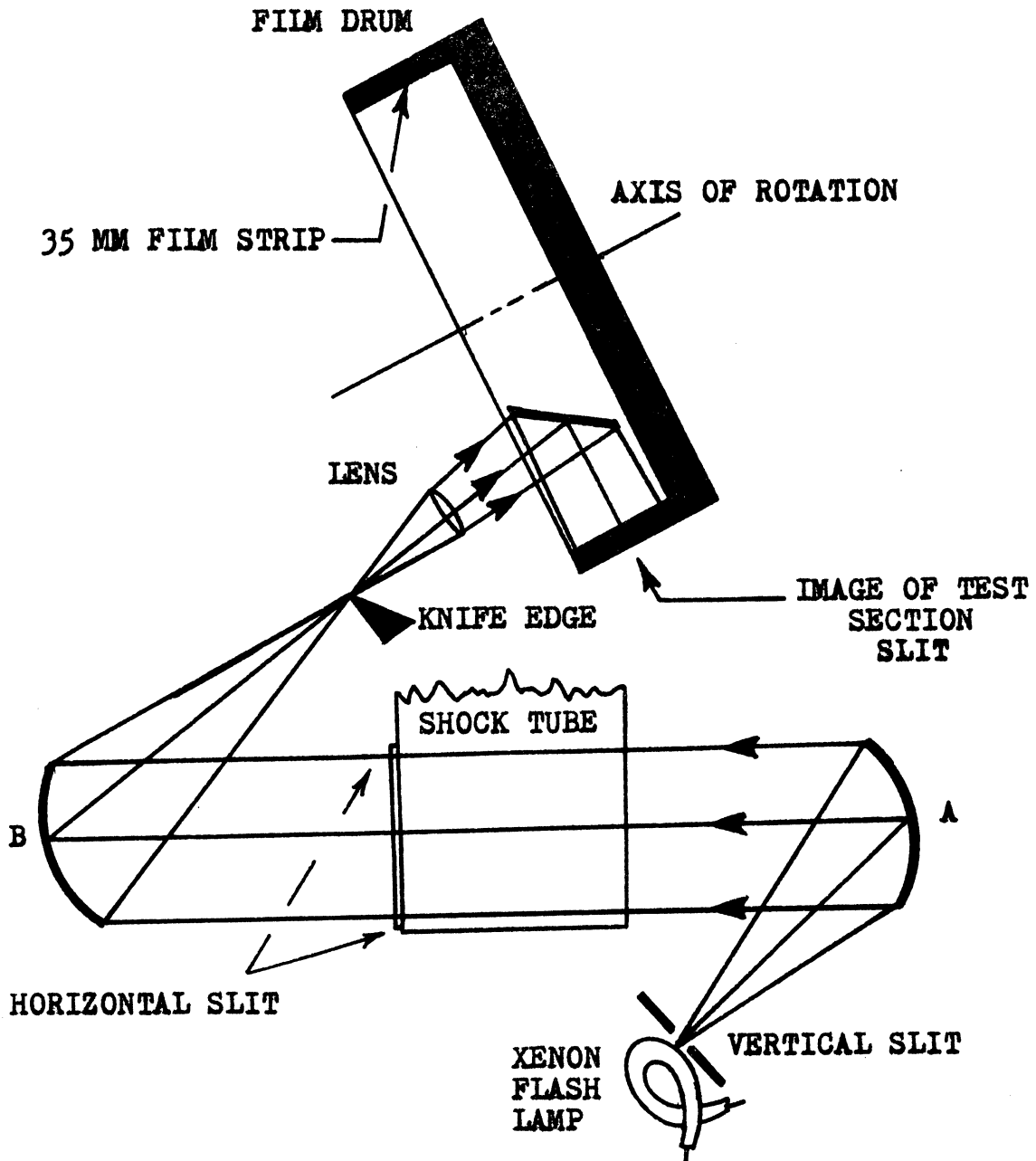
Figure 36. Schematic diagram of schlieren wave speed system

The fractional change of light intensity in a schlieren system for a density gradient which refracts light through an angle α is given by the expression[23]

$$\frac{\Delta I}{I} = \frac{\alpha F}{a} \tag{48}$$

where

F = focal length of the lenses or mirrors

a = width of slit image at the knife edge

This equation is valid provided that the density gradient is not so large that the slit image is moved entirely off the knife edge. The angle α can be written as

$$\alpha = (n_o - 1) D \frac{d\rho}{dx} \tag{49}$$

where x is a coordinate position measured along the shock tube axis (or, perpendicular to the parallel light beam).

The sensitivity of a schlieren system is directly proportional to the focal lengths of the lenses or mirrors used. This is the basis of the sensitive schlieren system used to measure the density gradients near the shock. These measurements are made in order to look for a delay in the population of the excited rotational eigenstates. The population of these levels takes up energy from the gas causing it to decrease in temperature and increase in density.

By using a narrow light source slit (0.006") and 46" focal length parabolic mirrors it is possible to detect

a density gradient of 0.0005 amagats per millimeter in

hydrogen.[*] A spacial resolution of less than 0.1 milli-

meter is attained by using a 0.006" wide vertical slit

over the photomultiplier and carefully orienting the light

beam perpendicular to the shock tube axis. These two

narrow slits cause a very great decrease in the light

reaching the photomultiplier so a very bright light source

is necessary if an adequate signal to noise ratio is to

be obtained. The laser is an obvious choice. It is also

useful for aligning the system since the angle of the beam

can be adjusted until the beam reflected from the windows

coincides with the incident beam. The laser beam can be

adjusted perpendicular to the windows to within 0.005 radians.

Thus the beam moves up or downstream by less than 0.1

millimeter as it traverses the 3" shock tube. The inter-

ferometer housing makes an excellent optical bench for this

arrangement since it shields the system from vibrations of

the building. These vibrations otherwise would cause a

large flutter in the light intensity at the photomultiplier.

Simple photomultiplier tubes such as the 931A, 1P21,

1P28, etc. are insufficiently sensitive to allow a clear

trace of the output signal. Statistical fluctuations are

too large to accurately read the shock wave signal. It is

also impossible to reliably trigger the scopes internally

---

*An optical system of this high sensitivity is necessary for
the detection of rotational relaxation effects. Interfer-
ometric methods are not sensitive enough to measure the small
density changes involved.

due to the dark current peaks.[*] The poor signal quality is partly due to the weak response of ordinary photocathodes to the red, 6328 Å, laser light. This difficulty is circumvented by use of a 14 stage RCA 7265 photomultiplier having an improved red sensitivity (S-20 spectral response) due to its special photocathode material. This is a very satisfactory solution. The resultant high signal to noise ratio can be seen in the oscilloscope traces shown in Chapter IV.

The circuit used with the 7265 photomultiplier is shown in Fig. 37. The 0.1 microfarad capacitors in the final stages are sufficiently large to insure the constancy of the voltage levels at the final dynodes during the arrival of intense light pulses of duration less than 10 microseconds. As long as the current maxima do not exceed 1 milliampere, the photomultiplier output will remain linearly related to the light intensity.

Although the rise time of the photomultiplier is on the order of a few nanoseconds, care must be taken or else the rise time of the signal displayed on the oscilloscope will be very much longer. This will occur if the output impedance of the photomultiplier circuit is too large or the coaxial cables leading to the oscilloscopes are too long.

---

[*]Internal triggering is very useful for this part of the experiment due to the high sweep speeds of 0.2 μs/cm used. This procedure greatly facilitates the synchronization of the sweep to the shock arrival.
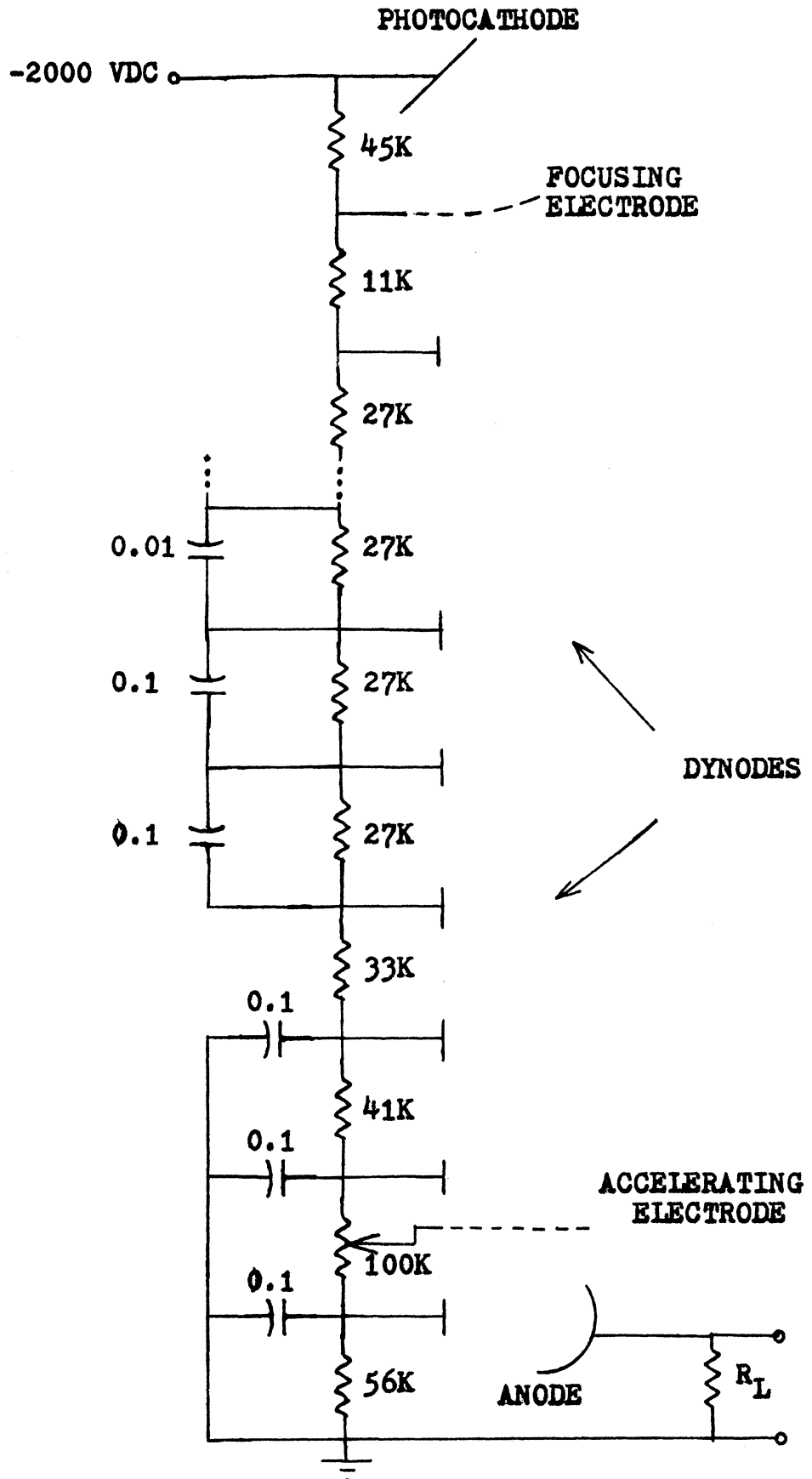
Figure 37. 7265 photomultiplier circuit

Consider, for example, a 10K output impedance of the photo-multiplier and three feet of coaxial cable leading to the oscilloscope. The stray capacitance of the photomultiplier socket plus that of the connecting cable is of the order of 100 picofarads. This leads to a rise time of

$$\tau_R = R_L C = 10^4 \times 10^{-10} = 10^{-6} \text{ sec} = 1.0 \text{ microseconds.}$$

This is longer than the whole duration of the signal to be measured. If the photomultiplier load resistance must be large in order to obtain measurable output voltages, then it is necessary to mount an emitter follower circuit at the base of the phototube and couple the signal to the oscilloscope using the low output impedance of this circuit. This was initially done using an emitter follower circuit similar to that used by Koopman[24] and Roberts[25]. Small nonlinearities in response were discovered by me, however, and this method of coupling was discontinued. It was found that light intensities were large enough so that a load resistance of 200 ohms would allow an output voltage of 0.2 volts without exceeding the photomultiplier current maximum of 1 milliampere. This voltage is sufficiently large to be measured easily on an oscilloscope. The signal on the load resistor is led to the oscilloscope using approximately three feet of coaxial cable. The expected rise time of the displayed signal is therefore

$$\tau_R = R_{output} C_{coax} = 200 \times 10^{-10} = 0.02 \text{ microseconds}$$

which is adequate for this experiment. Tests and dark current traces show that this predicted rise time is realized in practice.

In order to measure shock speeds and either fringe shifts or laser-schlieren traces, it is necessary to pass two beams at once through the test section. This is easily done by locating the sources of each beam at different heights near the focal point of parabolic mirror A. The insertion of a small mirror near the focal point of parabolic mirror B which intercepts only the lower beam allows these two optical systems to be separated (see Fig. 33).

CHAPTER IV

EXPERIMENTAL RESULTS OF RANKINE-HUGONIOT MEASUREMENTS

1. Cooled Shock Tube Performance

The aluminized-mylar-filled vacuum dewar surrounding the shock tube provides adequate insulation. The heat leak into the shock tube is approximately fifteen watts. This means that less than fifteen liters of liquid nitrogen per day are necessary to operate at a temperature of $80^\circ K$. At the present price of $18 ¢$ per liter this represents only a nominal cost. The shock tube temperature of $80^\circ K$ has been maintained for periods of time exceeding one month. For a temperature of $30^\circ K$, liquid helium is used as the coolant. Less than two liters of liquid helium per hour are necessary to maintain this temperature. Although only one watt-hour of heat is taken up by the heat of vaporization, seven watt-hours are taken up in heating the helium to its exhaust temperature of $30^\circ K$. This is the major reason why coolant tubes running back and forth along the shock tube are used rather than a liquid filled jacket surrounding it. At the present price of $4 per liter, the cost of maintaining shock tube at this temperature is substantial. For this reason the shock tube is not kept at $30^\circ K$ for long periods of time. Instead, the shock tube temperature is lowered from $80^\circ K$ using liquid helium starting early in the morning. Several hours are required to accomplish this. Three or

four shots are then fired in succession, after which, the
tube is allowed to rewarm to 80°K.

Initially the stainless steel driver was cooled in
the same manner as the expansion section using copper tubes
strapped tightly to its surface (see Fig. 24). For the
liquid helium cooled shots, however, a different design
was employed. A liquid nitrogen cooled cylindrical heat
shield is built around the driver section and a temperature
gradient from 30°K to 77°K is maintained within this section
of the shock tube. The temperature uniformity along the
aluminum expansion section is not greatly affected. The
higher temperature driver section reduces the cost of cooling
the shock tube with liquid helium and, at the same time,
increases the sound speed of the driver gas. This higher
sound speed makes it possible to generate stronger shocks
than otherwise can be attained. This is a modified version
of the "heated driver" technique.

In cooling the shock tube from room temperature, about
75 liters of liquid nitrogen are required. For cooling
from 80°K to 30°K, about 35 liters of liquid helium are
needed. The reservoirs are periodically filled and the
liquefied gas flows through the copper tubes slowly. A
pressure relief valve connected to a tube leading from the
top of the reservoir provides automatic regulation of the
flow rate. The reservoirs need to be refilled with liquefied
gases at about one hour intervals during the initial cooling
process.

The shock tube was found to perform quite adequately after the initial window sealing and water vapor problems were solved. The difficulties encountered in operating at these reduced temperatures, when everything is working properly, are not much greater than those for a room temperature shock tube. During normal operation four or five shots are taken per day. Approximately every two weeks the shock tube must be warmed to about $-50^{\circ}C$ to pump off the trace quantities of water vapor which have entered the system and coated the insides of the shock tube windows.

2. Schlieren Wave Speed Pictures

Several examples of schlieren wave speed pictures are shown in Fig. 38. The horizontal slit on the test section is imaged across a strip of film on a rotating drum as described in Chapter III. As the shock passes along the slit, light is deflected around the knife edge and the image of the shock passes across the film. Since the film is moving rapidly perpendicular to the slit image, the incident shock is seen as an inclined light line. The reflected shock appears as another inclined line but since its density gradient is in the opposite direction, it deflects light into the knife edge and the shock appears as a dark line. The cold gas of the interface region can be seen following the shock. The flow here is not homogeneous. A small amount
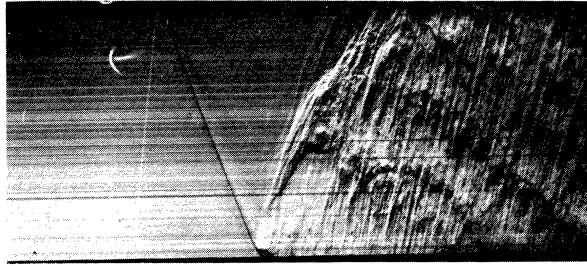
$T_0 = 296°K$ $P_0 = 11.0$ torr

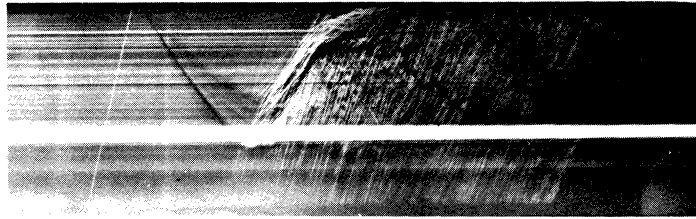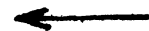$T_1 = 850°K$ $P_4 = 500$ psi (driver)

shock mach number = 3.21

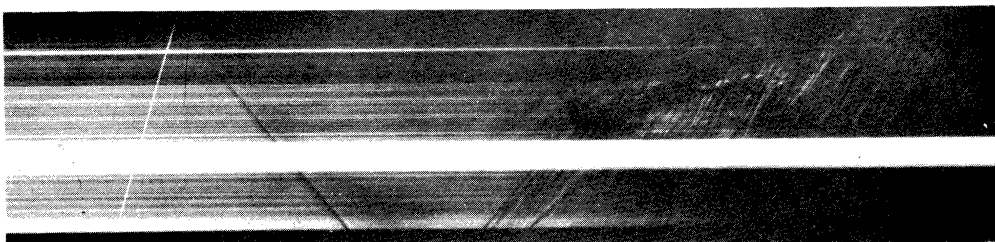direction of motion of film   position of test section slit

←

                     end wall

$T_0 = 85°K$ $P_0 = 1.84$ torr

$T_1 = 309°K$ $P_4 = 260$ psi

shock mach number = 3.51

$T_0 = 85°K$ $P_0 = 4.0$ torr

$T_1 = 183°K$ $P_4 = 202$ psi

shock mach number = 2.30

Figure 38. Wave speed schlieren pictures in hydrogen

of bifurcation of the reflected shock, due to its interaction with the boundary layer, can also be seen. The light line in the center of the picture is caused by scattered light from the laser-schlieren system that was also set up in this part of the experiment. All flow regions are similar to those observed in room temperature shock tubes as can be seen by comparison with the room temperature shock picture.

3. Measurement Results and Interpretation

A typical shot involves the measurement of the shock speed, fringe shifts, and pressure gauge output. This is shown in Fig. 39.

In order to convert a fringe shift measurement into a density ratio measurement, Eq. 47 is rewritten

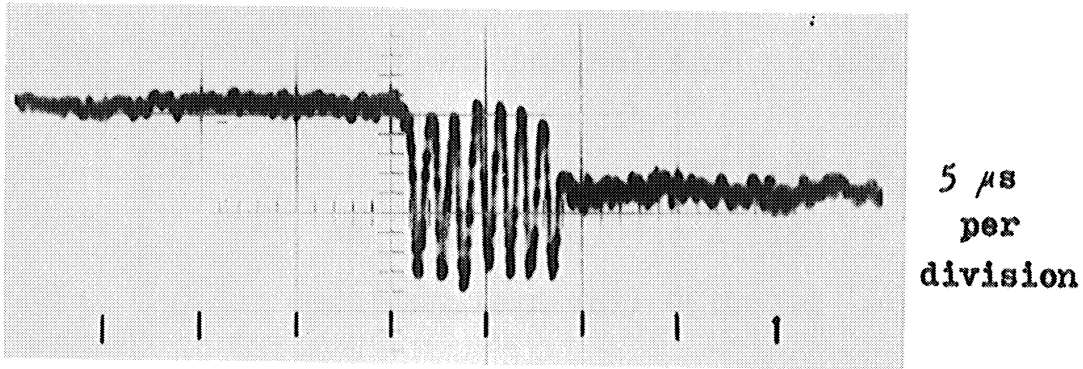$$\Delta \rho = \rho_1 - \rho_0 = \frac{\lambda \, N_{fs}}{(n_0 - 1) \, D}$$

so,

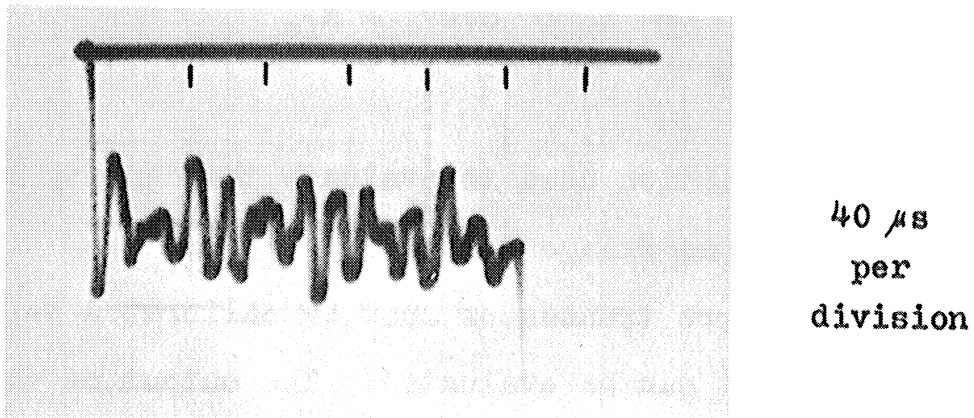$$\frac{\rho_1}{\rho_0} = 1 + \frac{\lambda \, N_{fs}}{(n_0 - 1) \, D \, \rho_0} \tag{50}$$

ρ_0 is in units of amagats and can be written

$$\rho_0 = \frac{T_{S.T.P.}}{P_{S.T.P.}} \frac{P_0}{T_0} = \frac{273.2}{760} \frac{P_0}{T_0} \tag{51}$$

where P_0 is in units of torr and T_0 is in $^\circ K$.

(a)　Fringe shift oscilloscope output

5 μs
per
division

(b)　Pressure trace

40 μs
per
division

DIRECT MEASUREMENTS:　　$u = 1.46$ km/sec

$P_0 = 17.0$ torr

$T_0 = 90^{\circ}K$

$N_{fs} = 6.80$ fringes

$\rho_1/\rho_0 = 2.8$

$P_1/P_0 = 10.06$

$P_1 = 180.$ torr

CALCULATED RESULTS:　$\rho_1/\rho_0 = 2.7$

$P_1 = 169.$ torr

$P_1/P_0 = 9.5$

Figure 39.　Typical results from a single shot

Using the preceding relation and the values

$$D = 76.2 \text{ mm}$$

$$\lambda = 6328 \text{ Å or } 6.328 \times 10^{-4} \text{ mm}$$

$$n_0 = 1.000139 \text{ (for hydrogen)}$$

Eq. 50 becomes

$$\frac{\rho_1}{\rho_0} = 1 + 6.07 \frac{P_0}{T_0} N_{fs}. \tag{52}$$

This is the relation used to evaluate the density ratio from the measured fringe shifts.

The pressure transducer must be calibrated before its measured output can be evaluated. The output of the transducer depends on its temperature, so this calibration must be done at the operating temperature of the shock tube. It is possible to calibrate the gauge statically, but due to stray charge which leaks onto the quartz crystal during the time that this is being done, it is found more convenient to calibrate the gauge directly by use of shock waves in ideal gases. This is done with helium and argon test gases. The output of the crystal is directly proportional to the applied pressure so only a few experimental points are required.

Oscillations in the pressure gauge output are caused primarily by the undamped oscillations within the gauge itself due to the sudden pressure jump across the shock. There is an additional effect due to wall vibrations caused

by the diaphragm burst and sound wave reflections in the
shock tube walls. The oscillations are lessened, but not
eliminated, by an interstage filter in the charge amplifier
which suppresses the natural ringing frequency (130 kilohertz)
of the pressure gauge. The mean value of the output voltage
is obtained by averaging over these oscillations. A polar
planimeter is used to measure the pressure traces which
have previously been photographically enlarged to 8" x 11"
size. The repeatability of subsequent measurements with
the polar planimeter is much less than 1%. A plot of
the calculated pressure, based on the measured shock speed
and initial pressure measurement is shown in Fig. 40. as
a function of the average value of the measured pressure
trace height. Pressure measurement errors are attributed
to unsymmetric oscillations about the "true" value of the
pressure. These errors are estimated from the scatter of
points to be 5% to 10%.

Pressure and shock speed measurements alone are not
sufficient to enable para and normal hydrogen to be
distinguished from each other or from classical monatomic
or diatomic gases. This is due both to the errors in the
pressure measurement and the insensitivity of the pressure
to the internal degrees of freedom of the gas.

Density measurements, however, are both accurate and
sensitive to the effects of the internal degrees of freedom.
The Rankine-Hugoniot relation can be plotted using the
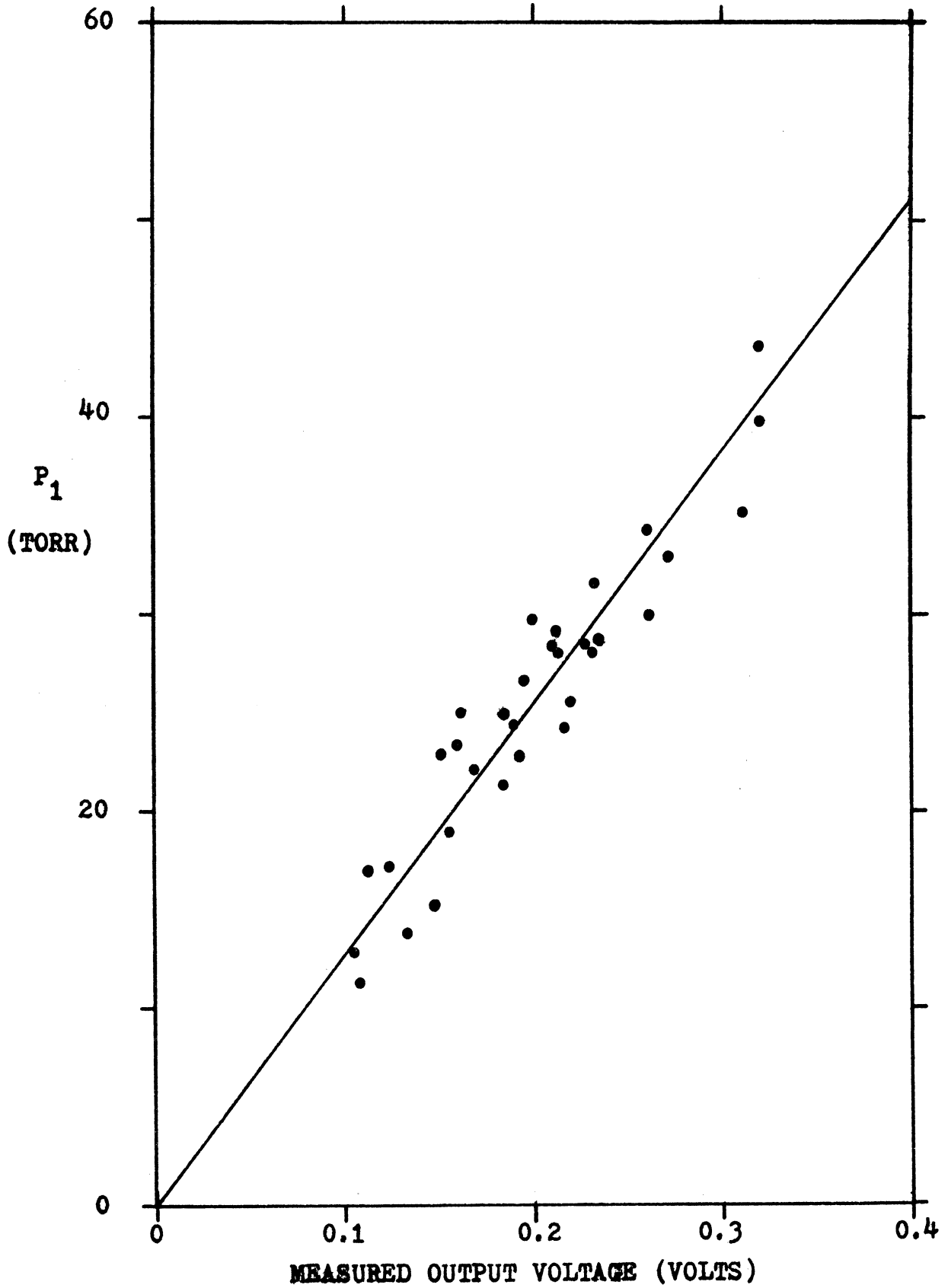density measurements and the shock speed measurements.

Figure 40. Experimental results of pressure trace measurements

The shock speed, in conjunction with the shock calculation, is used to determine the pressure ratio expected for each shot. This is most accurate method of obtaining a point on the Rankine-Hugoniot curve. The results of the density and shock speed measurements for the Rankine-Hugoniot equation are shown in Figs. 41 and 42 for initial temperatures of $30^\circ K$ and $90^\circ K$.

There is a third method of determining the Rankine-Hugoniot curves, which is more direct but less accurate. This method also demonstrates the internal consistency of the experimental results. The points are obtained using only the measured pressures and densities. The shock speed measurement is ignored. The results are shown in Fig. 43 for the initial shock tube temperature of $90^\circ K$. The results are extremely inaccurate for the $30^\circ K$ shots due to the very low initial pressures used. These results are not shown.

4. Brief Discussion of Errors

The initial pressure is measured to within $\pm$ 0.05 torr using a di-butyl pthylate manometer. Since initial pressures are usually greater than ten torr in this part of the experiment, errors from this source are less than $\frac{1}{2}\%$. The fringe shifts can be measured to within 1/10 fringe which, for a typical 5 fringe shifts, represents an accuracy of 2%.
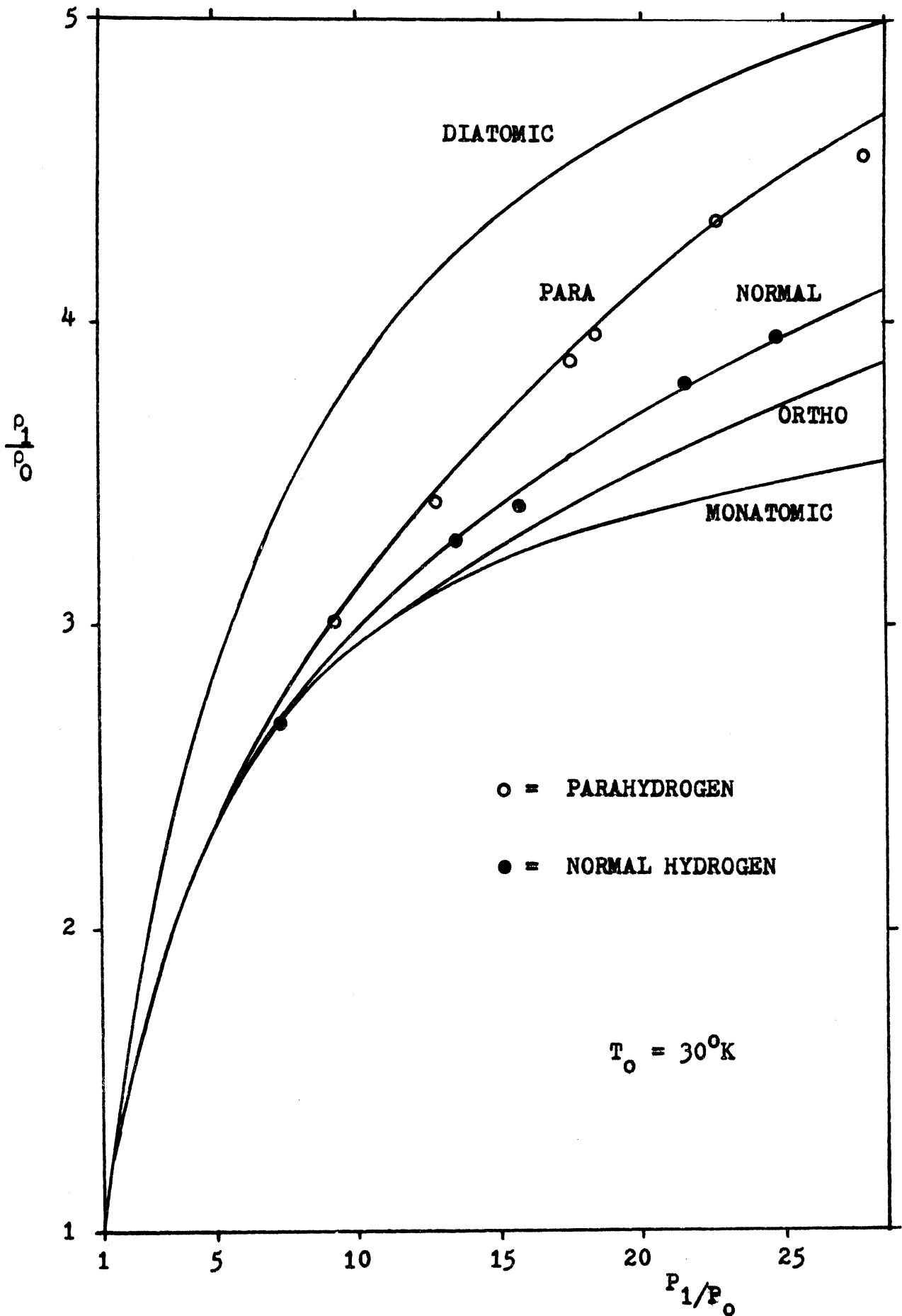
Figure 41. 30°K Rankine-Hugoniot results using shock speed and density ratio measurements
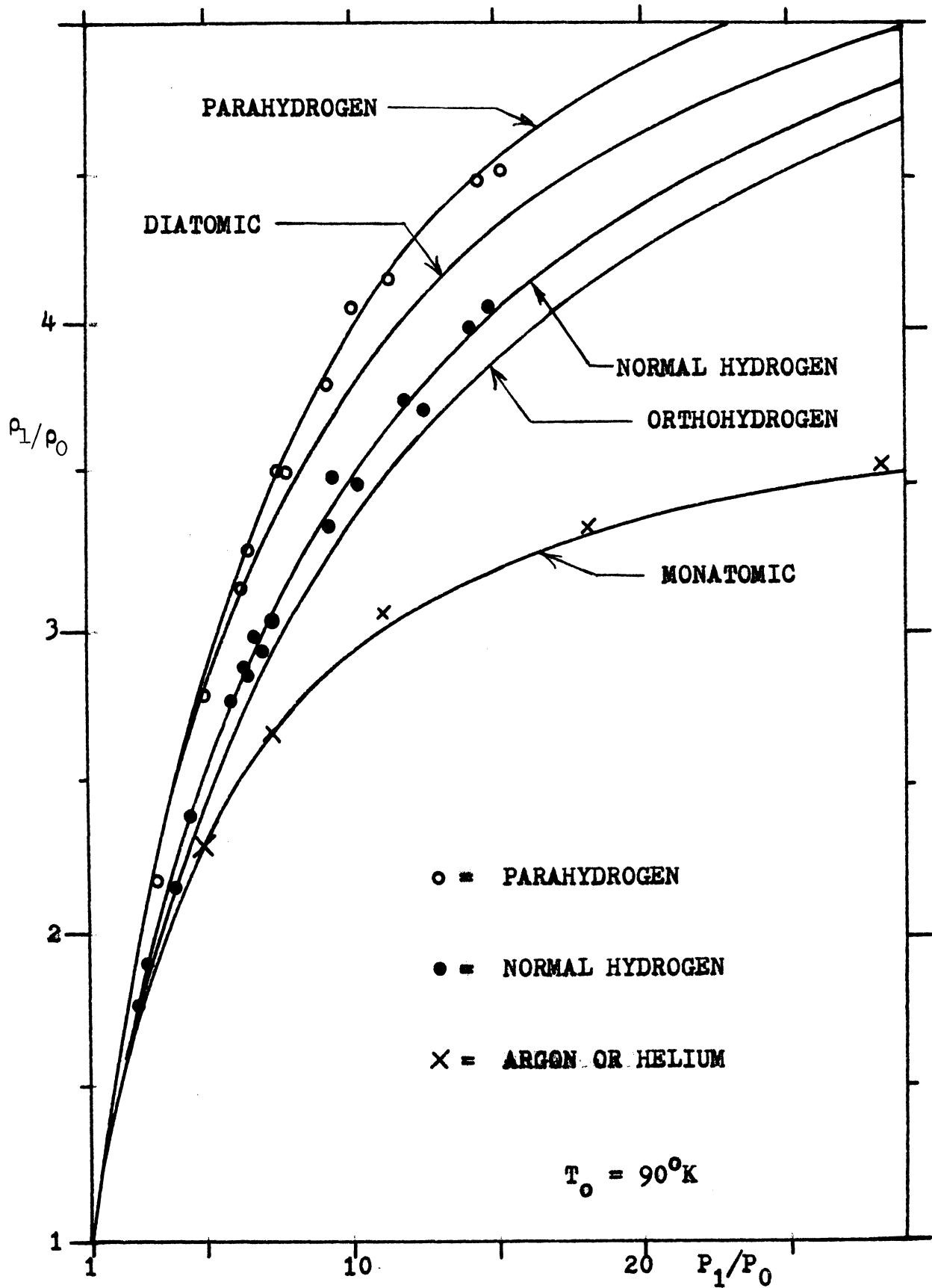
Figure 42. 90°K Rankine-Hugoniot measurements using shock speed and density ratio measurements
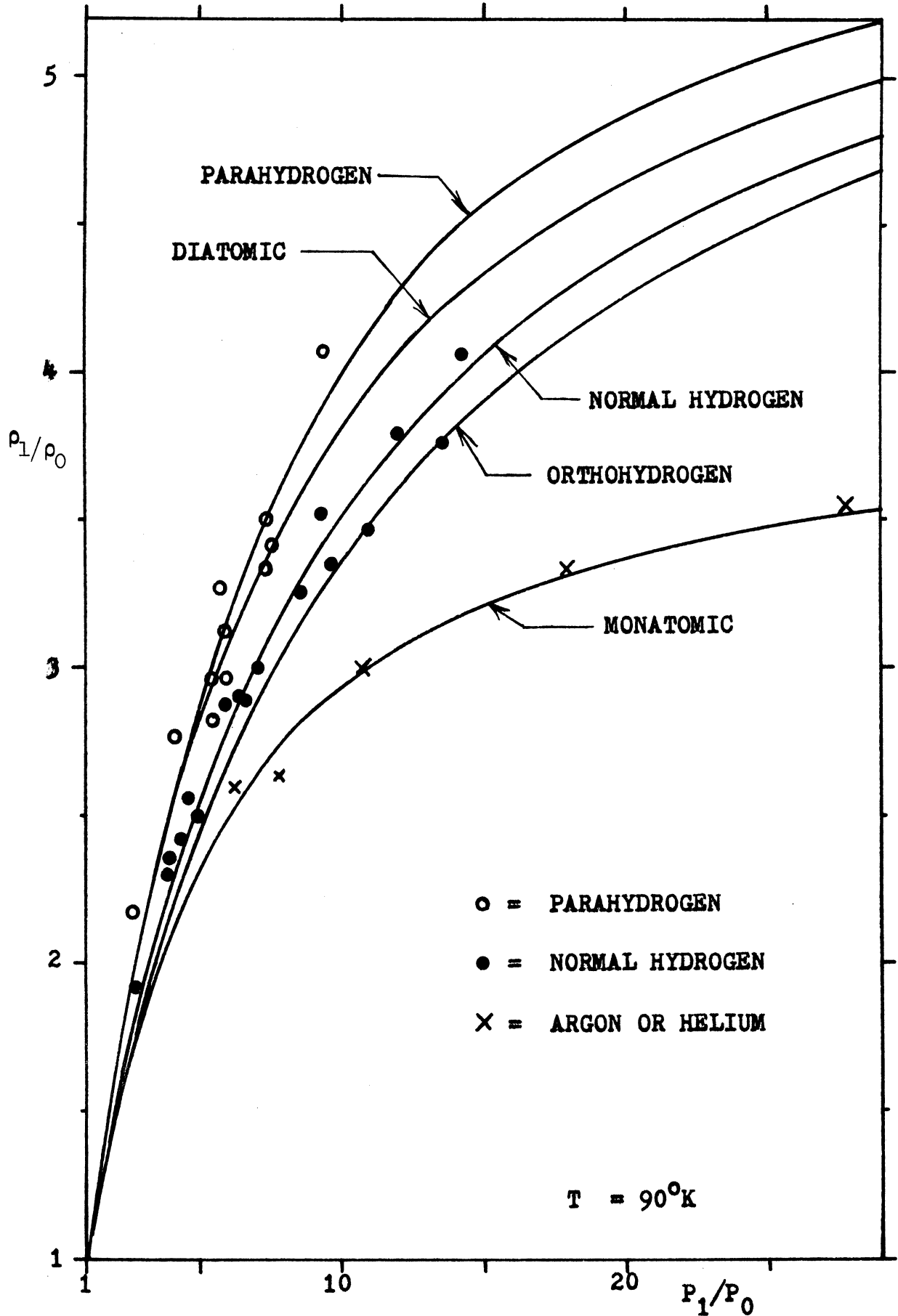
Figure 43. Rankine-Hugoniot equation using direct measurements of both pressure and density

Due to the 1 microsecond digital nature of the scaler,
which measures transit times between photomultipliers #1
and #2 of about 70 microseconds, the errors in shock velocity
can be as much as 1½%. This results in calculated pressure
uncertainties of at most 3%. The temperature uniformity
along the tube is better than 1°K which represents 1% at
90°K initial temperature and 3% at 30°K initial temperature.
Thus in this experiment uncertainties of at most 5% can be
expected.

5. Conclusions

The cryogenic shock tube has proven to be a feasible
and economical instrument which can be operated at 80°K for
long periods of time and at temperatures as low as 30°K for
shorter periods. It is believed that even lower temperature
operation is possible with this design.

Shock waves at low temperatures are well formed and
exhibit flow regions similar to those for higher initial
shock tube temperatures. The flow behind both the incident
and the reflected shocks is uniform and homogeneous.

The predictions of the Rankine-Hugoniot equation have
been measured and confirmed for parahydrogen and normal
hydrogen. The scatter of measured points falls well within
the expected range of 5%. It has been demonstrated that
shock wave experiments can be used for observing such

comparatively esoteric effects as the difference between
parahydrogen and normal hydrogen.[50]

CHAPTER V

EXPERIMENTAL RESULTS OF ROTATIONAL RELAXATION MEASUREMENTS

1. Measurements and Interpretation

A large number of shots have been made at various initial pressures using the sensitive laser-schlieren system described in Chapter III. Several shock profiles for normal hydrogen are shown in Fig. 44. The asymmetry of these profiles is ascribed to density gradients which are caused by the cooling of the gas behind the shock due to translational energy being lost in exciting the rotational energy states. In order to interpret these results and infer a relaxation time from them, the relaxation processes and measurements must be examined in detail.

For a simple two-level gas of n particles per unit volume, the populations must obey the reaction equation

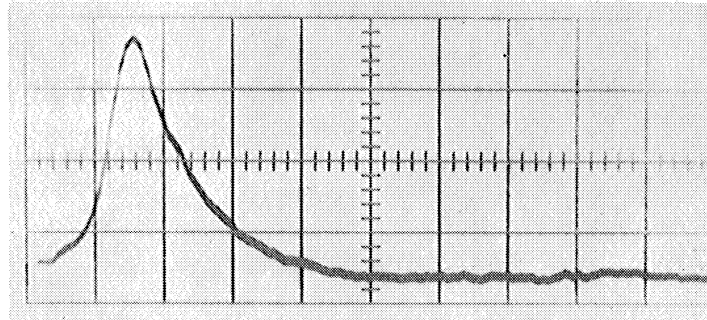$$\frac{dn_b}{dt} = k_{ab}\, n_a - k_{ba}\, n_b \tag{53}$$

where

n_a = number density of particles in state a (possibly degenerate)

n_b = " " " " " " b " "

k_{ab} = probability per second of a transition a $\longrightarrow$ b

k_{ba} = " " " " " " b $\longrightarrow$ a

NORMAL HYDROGEN

$$P_o = 1.55 \text{ torr} \qquad u = 3.0 \text{ km/sec}$$
$$T_o = 98^\circ K \qquad T_1 = 410^\circ K$$

sweep speed
$0.2\mu s/\text{division}$

PARAHYDROGEN

$$P_o = 2.0 \text{ torr} \qquad u = 2.4 \text{ km/sec}$$
$$T_o = 100^\circ K \qquad T_1 = 350^\circ K$$

sweep speed
$0.2\mu s/\text{division}$

NORMAL HYDROGEN

$$P_o = 4.00 \text{ torr} \qquad u = 1.26 \text{ km/sec}$$
$$T_o = 83^\circ K \qquad T_1 = 130^\circ K$$
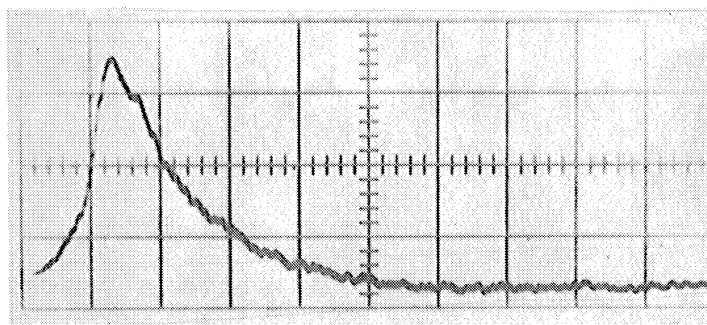
sweep speed
$0.5\mu s/\text{division}$

Figure 44. Shock profiles in hydrogen

Since the total number of particles is a constant, the constraint

$$n_a + n_b = n \tag{54}$$

must be observed. So

$$\frac{dn_b}{dt} + (k_{ab} + k_{ba}) \, n_b = k_{ab} \, n. \tag{55}$$

Assuming that k_{ab} and k_{ba} are constants independent of n_a and n_b, this differential equation has the solution

$$n_b = \frac{k_{ab} \, n}{k_{ab} + k_{ba}} (1 - e^{-t/\tau}) \tag{56}$$

where

$$\tau = \frac{1}{k_{ab} + k_{ba}} \tag{57}$$

is the relaxation time, and the initial condition $n_b=0$ at t=0 has been assumed. The same exponential behavior would occur for any initial population of state b.

k_{ab} and k_{ba} can be related using the fact that at equilibrium there must be a stationary population of each level, which obeys the Boltzmann distribution law. Thus

$$\frac{dn_b}{dt}^{equil} = 0 = k_{ab} \, n_a^{equil} - k_{ba} \, n_b^{equil} \tag{58}$$

and

$$k_{ba} = \frac{n_a^{equil}}{n_b^{equil}} = \frac{g_a \, e^{-\epsilon_a/kT}}{g_b \, e^{-\epsilon_b/kT}} \, k_{ab} \tag{59}$$

The relaxation time can thus be written

$$\tau = \cfrac{1}{1 + \cfrac{g_a}{g_b} e^{(\epsilon_b - \epsilon_a)/kT}} \; \frac{1}{k_{ab}} \qquad (60)$$

Since rotational transitions are caused primarily by binary molecular collisions, k_{ab} should be proportional to the collision frequency ν_c, and

$$k_{ab} = \nu_c \; F(T). \qquad (61)$$

At a fixed temperature, ν_c is proportional to the pressure P. Thus the relaxation time may be written

$$\tau = \frac{G(T)}{P}. \qquad (62)$$

The dependence on temperature is not obvious and must be determined experimentally or by a complex calculation.

The purpose of this experiment is to measure $G(T)$ for normal hydrogen and parahydrogen. These are both, to a very good approximation, two-level gases for temperatures less than about $400^\circ K$.

In order to monitor the relaxation process, measurements are performed at one point in space as a function of the time, t, after the arrival of the shock at that point (see Fig. 45). The gas at a distance x behind the shock front has been shocked for a longer time t'. These quantities are
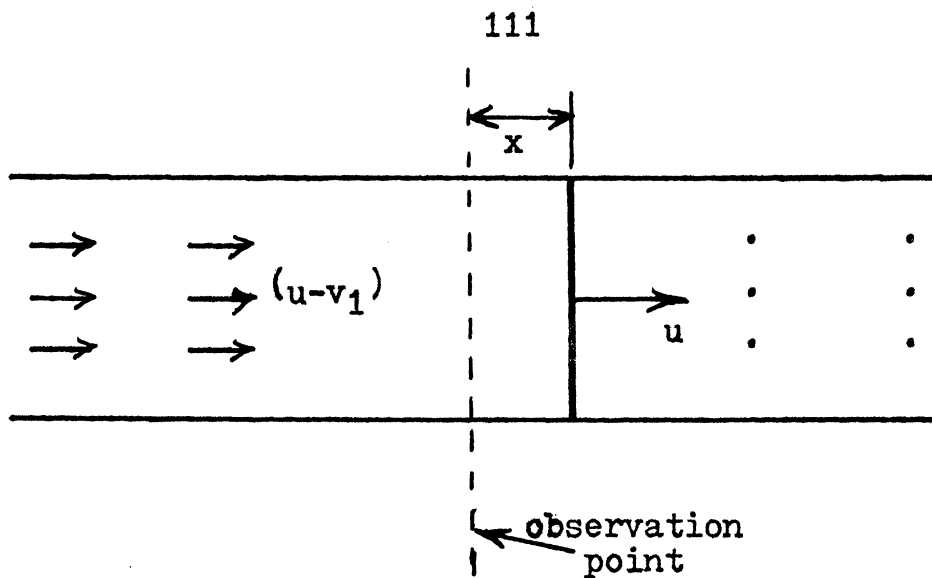
Figure 45. Relaxation measurements at a point in space

related by the equation

$$x = v_1 t'$$

(63)

where v_1, as defined earlier, is the speed of the shocked gas with respect to the shock front, and u is the velocity of the shock. From the conservation of mass equation

$$\rho_o u = \rho_1 v_1$$

t' can be expressed as

$$t' = \frac{x}{u} \frac{\rho_1}{\rho_o}$$

(64)

However, t can be written as x/u. Thus the actual length of time elapsed since the gas at the observation point has been shocked can be expressed as

$$t' = \frac{\rho_1}{\rho_o} t.$$

(65)

The quantity that is measured by the schlieren system at the observation point is the density gradient. This is very nearly proportional to the temperature gradient since the pressure changes very little. The temperature gradient is exactly proportional to dn_b/dx, the gradient of the population of the excited state b.[*] Thus the photomultiplier intensity, $I(t)$, will be a record of dn_b/dx as a function of the time t. This can be written in terms of the length of time, t', that the gas has been shocked. By use of the chain rule and equations 55 and 56

$$I(t) = \frac{dn_b}{dx} = \frac{dn_b}{dt'}\frac{dt'}{dx} = \frac{dt'}{dx} k_{ab} \, n \, e^{-t'/\tau} \qquad (66)$$

In terms of the time t, this expression becomes

$$I(t) = \frac{\rho_1}{\rho_0} \frac{k_{ab} \, n}{u} \, e^{-t/(\tau \, \rho_0/\rho_1)} \qquad (67)$$

or,

$$I(t) = \frac{\rho_1 k_{ab} \, n}{\rho_0 \, u} \, e^{-t/\tau_A} \qquad (68)$$

where τ_A is an "apparent" relaxation time which can be determined by fitting an exponential curve to the photomultiplier signal. The actual relaxation time of the gas can be determined from the relation

$$\tau = \frac{\rho_1}{\rho_0} \tau_A \qquad (69)$$

This time, τ , can be determined for any experiment with a pressure P. The result can then be converted to

the standard form of the relaxation time for the gas at a pressure of one atmosphere. This is done by using the pressure dependence given in Eq. 62.

$$\tau^* = \frac{\text{relaxation time for}}{\text{one atmosphere pressure}} = \frac{P_1}{760} \frac{\rho_1}{\rho_0} \tau_A \qquad (70)$$

or,

$$\tau^* = \frac{P_1}{P_0} \frac{\rho_1}{\rho_0} \frac{P_0}{760} \tau_A \qquad (71)$$

This is the form used to reduce the measured relaxation times to the standard relaxation times of one atmosphere pressure.

The shock profile traces are measured using a traveling microscope and the results are plotted on semi-log paper. Almost all curves can be fitted well with a straight line. Fig. 46 shows a good, but not unusually good, example of the closeness of the fit. The apparent relaxation time is deduced from this graph by the formula

$$\tau_A = \frac{t_2 - t_1}{\ln 10} = \frac{t_2 - t_1}{2.303} \qquad (72)$$

where t_i is the intercept of the fitted straight line with the dividing line between two adjacent cycles of the log paper.

---

*These gradients are equal since e, the energy per unit mass, must be constant during the relaxation process and can be written as $e = 3/2 \ kT' + n_b \ \epsilon_b$, with $T' =$ translational temperature.
Thus the gradient of this expression implies

$$\frac{dT'}{dx} = - \ \epsilon_b \frac{dn_b}{dx}$$
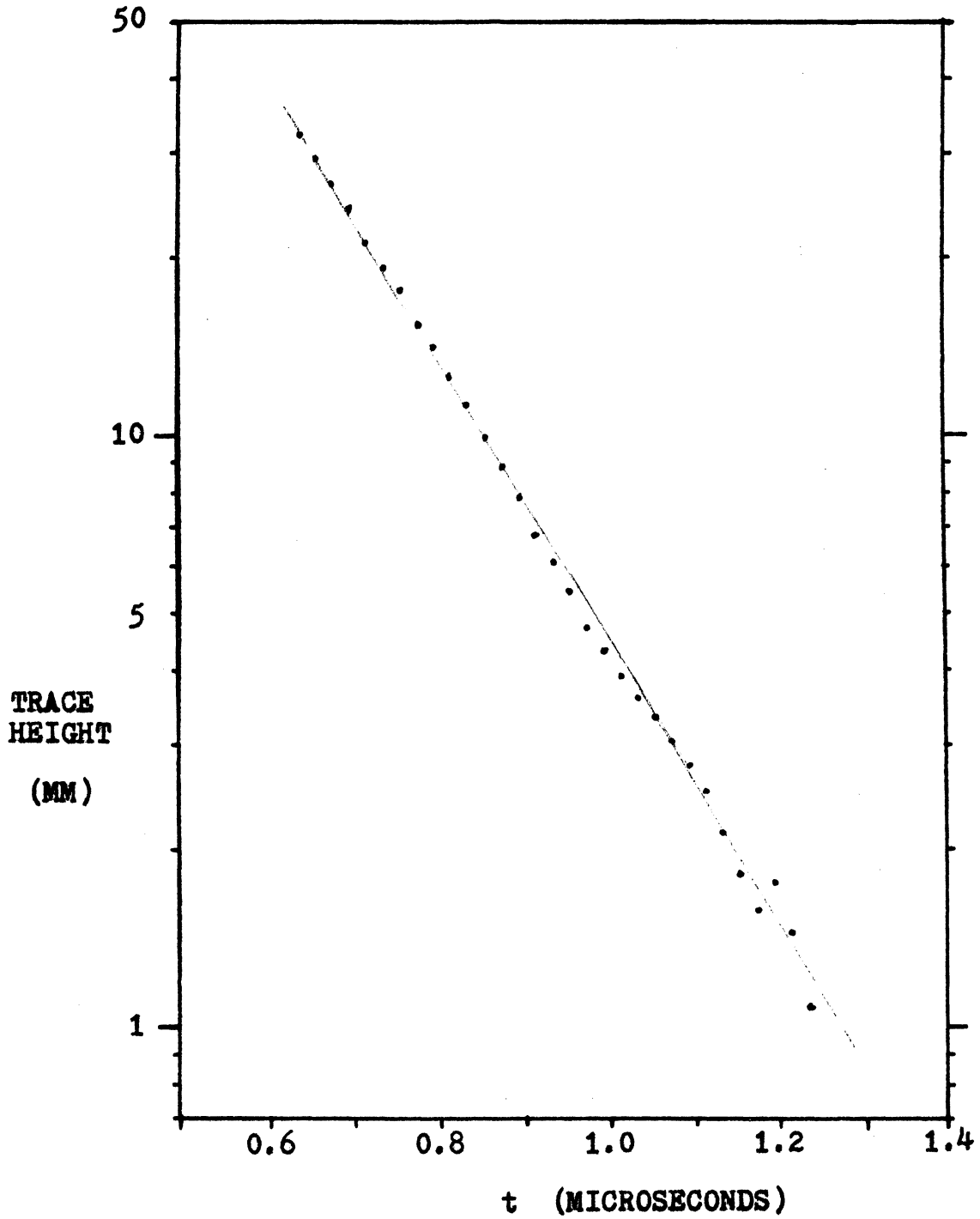
as asserted.

Figure 46. Schlieren density gradient trace - semi-log plot

The results of the rotational relaxation measurements
are shown in Fig. 47 for normal hydrogen and Fig. 48 for
parahydrogen. Relaxation times are given for a broad range
of temperatures. Initial pressures vary from 1.5 to 5.0
torr and are distributed over the entire temperature range.
No pressure dependence, other than the assumed linear relation,
can be detected from the data. This can be seen in Fig. 49
where the deviation of the relaxation times from the mean
values is plotted as a function of the pressure.

These results can also be written in terms of Z, the
number of collisions necessary for the gas to relax to 1/e
of its equilibrium value. To do this it is necessary to
know the frequency of collisions at each temperature. The
time between collisions τ_c, for hydrogen at 1 atmosphere
pressure is given by Herzfeld[27] as 0.3×10^{-10} sec at $90^{\circ}K$
and 0.7×10^{-10} sec at $296^{\circ}K$. The collision number, Z, for
population of the rotational energy states can be written as

$$Z = \frac{\tau^*}{\tau_c} . \qquad (73)$$

The results for Z as a function of temperature range from
370 collisions at $200^{\circ}K$ to 440 collisions at $350^{\circ}K$.

Several shots were made in monatomic gases. No asymmetry
is observed as can be seen in the shock profiles shown in
Fig. 50. This is what is expected since no relaxation processes
are expected at these temperatures. The shock profiles are
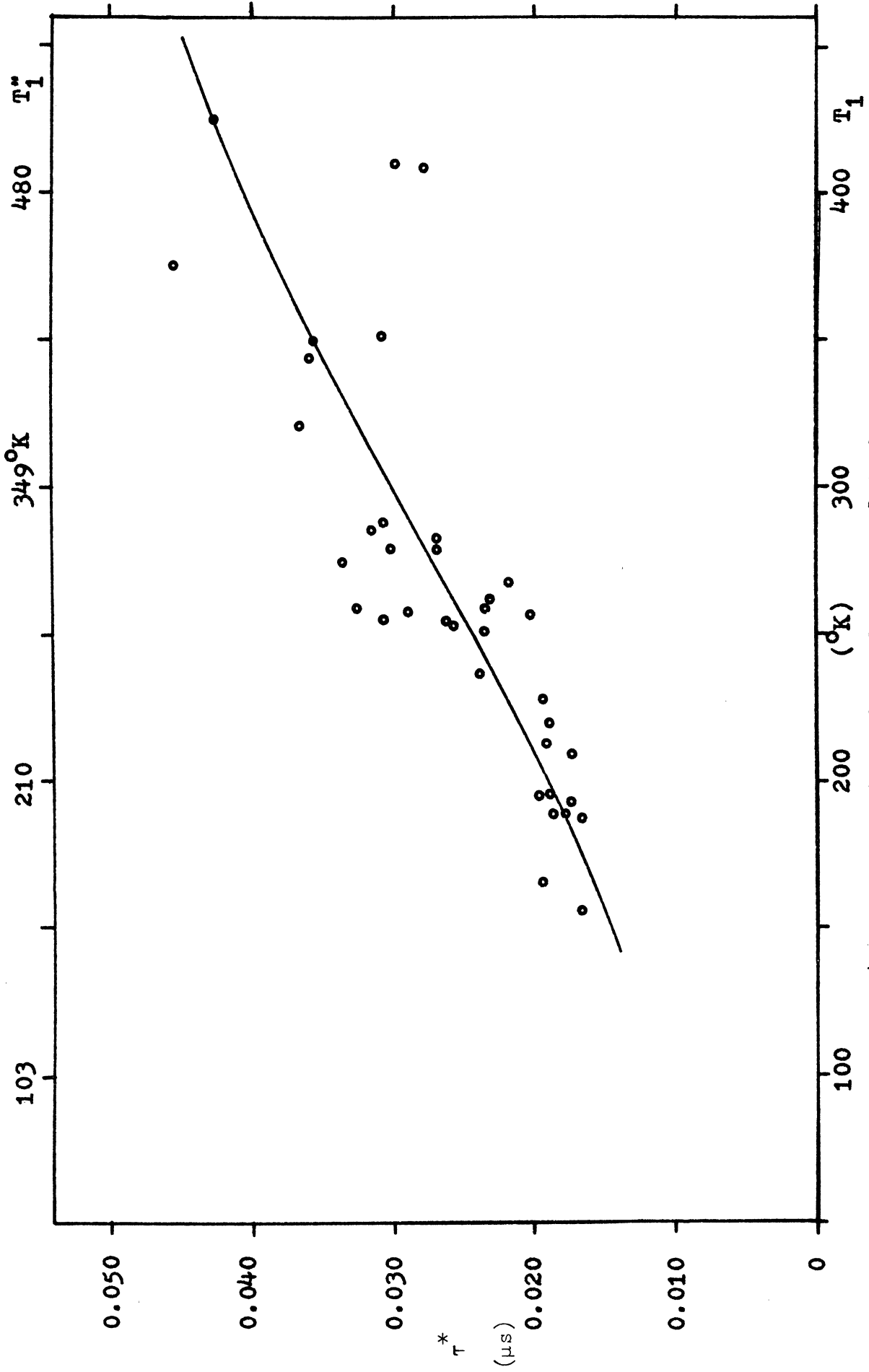broader in time than those in hydrogen, but this is due to

Figure 47. Relaxation times for normal hydrogen
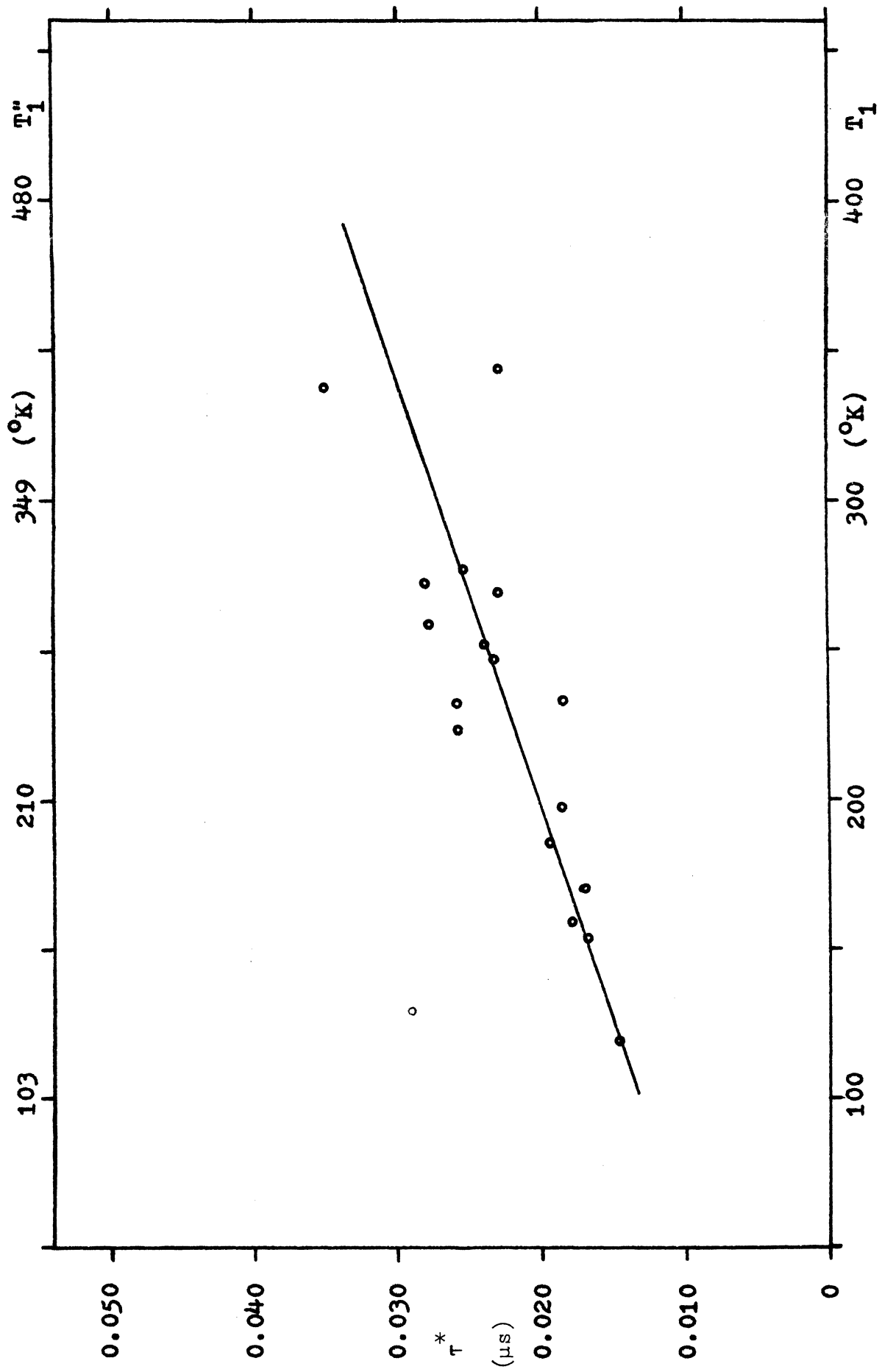
Figure 48. Relaxation times for parahydrogen
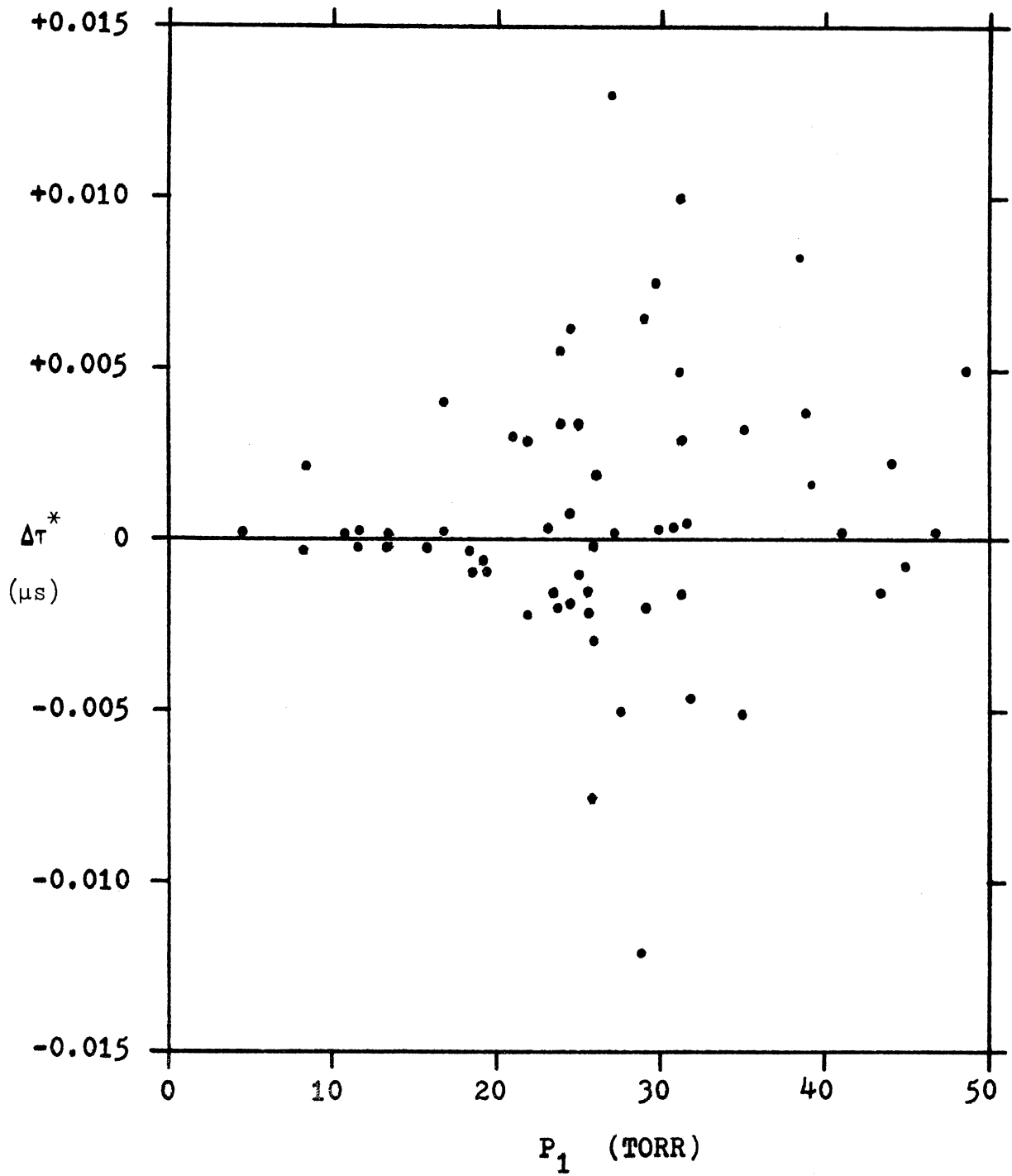
Figure 49. Deviation of relaxation times from mean values
as a function of pressure
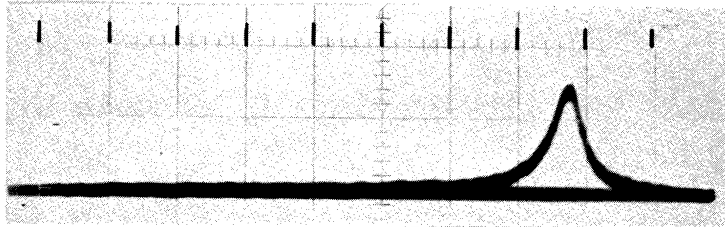
sweep speed
1.0 μs/division

NEON

P_o = 3.0 torr   u = 0.93 km/sec
T_o = 97°K T_1 = 1139°K
                         Mach number 5.8
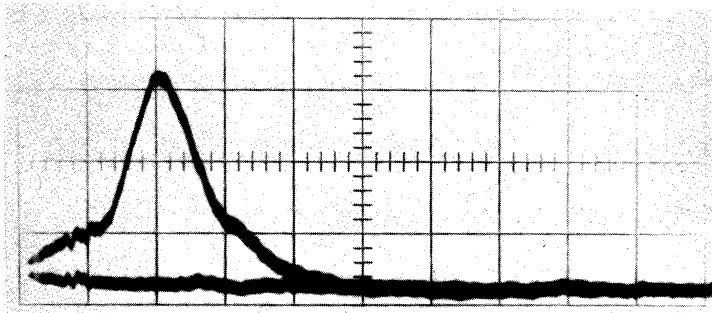
sweep speed
0.5 μs/division

NEON

P_o = 3.0 torr   u = 0.69 km/sec
T_o = 86°K T_1 = 564°K
                         Mach number 4.3

Figure 50.   Shock profiles in neon

120

the differences in shock speeds. In terms of the spacial

thickness, these neon shocks are comparable to hydrogen

shocks.

Shock profiles in deuterium show a tail similar to

that of hydrogen. Several traces are shown in Fig. 51.

This is what should be expected since ultrasonic experiments[27]

indicate that the rotational relaxation times for deuterium

should be comparable to those for hydrogen.

2. Errors

Initial pressures of 1.0 to 8.0 torr are measured with

a di-butyl pthylate manometer. Using a low power microscope

it is possible to measure to an accuracy of $\pm$ 0.01 torr.

The error from this source is insignificant. Also negligible

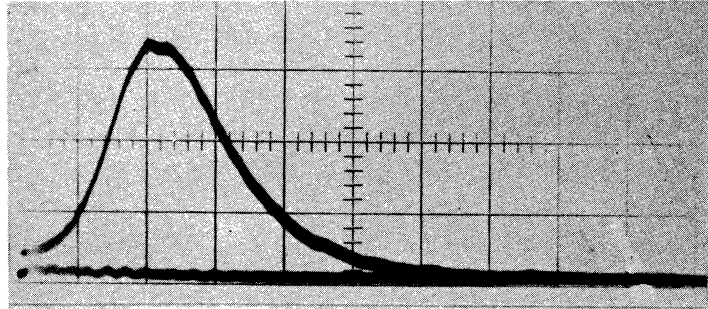are the effects of the $\pm$ 1°K temperature measurement errors

and non-uniformities. Research grade hydrogen is used and

leak rates into the vacuum system are less than 2 microns

per minute. It is not believed that impurities contribute

to the scatter of the experimental points. Since the

collision numbers for rotational excitation are always less

than 500, impurities would have to be greater than about

one part per thousand for any effect to be seen. The rise

and fall times of the electronic circuits were calculated

and measured to be less than 0.02 microseconds, as stated

in Chapter III. Thus errors from this source are also small.

DEUTERIUM

$$P_o = 2.2 \text{ torr}$$
$$T_o = 85^\circ K \qquad 0.2\mu s/\text{division}$$
$$T_1 = 346^\circ K$$
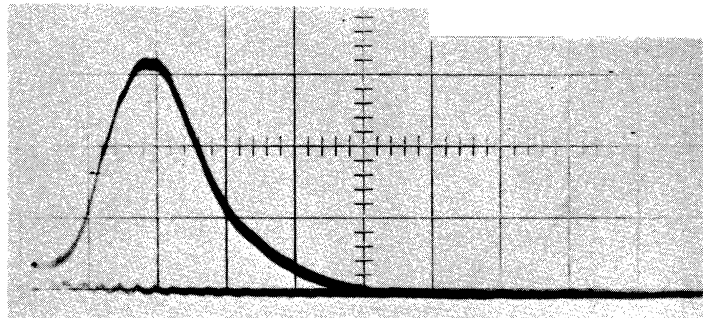
DEUTERIUM

$$P_o = 3.0 \text{ torr}$$
$$T_o = 87^\circ K \qquad 0.2\mu s/\text{division}$$
$$T_1 = 281^\circ K$$

Figure 51. Shock profiles in deuterium

The largest uncertainties are probably introduced through the diffraction of the monochromatic laser light from the shock and the necessity of making measurements very close to the shock. It is not always possible to determine accurately the point at which the shock image leaves the photomultiplier slit and the relaxation tail begins. Additionally, it is believed that some shots show evidence of boundary layer effects and shock curvature which cause a disturbance behind the shock. It is noteworthy that the scatter of the experimental points is not very large for shocks with low final temperatures. For these temperatures, laboratory relaxation times are longer due to the smaller value of the density ratio, and the shock curvature is less pronounced due to the higher initial pressures used.

The actual temperature of the gas during the relaxation process is always higher than the final equilibrium temperature T_1. The temperature of the gas before any rotational relaxation has taken place is called T_1''. Values of T_1'' compared to T_1 are shown in Figs. 47 and 48. Errors introduced by ignoring this temperature non-uniformity are small compared to other errors in the experiment.

3. Summary of Related Experiments

There have been a number of shock wave experiments carried out by Donald F. Hornig and co-workers[28, 29] concerning the measurement of shock thicknesses in hydrogen, argon, nitrogen, carbon monoxide, and other gases. For high initial pressures, the shock thickness is on the order of a wavelength of light. The measurement of the reflectivity of a beam of light obliquely incident on the shock, as a function of the angle of reflection, allowed the evaluation of the thickness of a shock. It was possible to determine the shock thickness, for most gases used, to be between 2 and 25 mean free paths. For hydrogen, however, the shocks were much thicker. The absolute thickness could not be determined by this method. These measurements for hydrogen implied a **lower limit** for relaxation times of 1.1×10^{-8} seconds or, more than 150 collisions. No other shock tube measurements of rotational relaxation times have been made.

In 1945, Arthur Kantrowitz[30] developed a method of measuring relaxation times in gases using an impact tube. In 1947, Paul W. Huber and Arthur Kantrowitz[31] used this method to measure the rotational relaxation times of hydrogen. A stream of high pressure gas from a flared orifice in a chamber is directed against a small impact tube connected to a manometer. If the flow is slow enough that the internal degrees of freedom are always in equilibrium with the translational degrees of freedom during the

recompression process, then the impact tube pressure is the same as that of the chamber. If, however, the flow is so fast that the internal degrees of freedom cannot follow the translational degrees of freedom during the recompression process at the front of the impact tube, then the measured pressure is lower than the chamber pressure. By varying the flow speed and measuring these pressure differences it was possible to measure the rotational relaxation times for hydrogen. Results were obtained for several temperatures and are shown in Fig. 52.[27]

Rotational relaxation has been the subject of numerous experiments in the ultrasonic absorption and dispersion of sound in hydrogen and deuterium. A. Van Itterbeek and collaborators[32, 33] (1938) were the first to observe the anomalous absorption of sound in hydrogen and deuterium due to a delay in the exchange of energy between the translational and the rotational degrees of freedom. Further experiments were done by Van Itterbeek[34, 35] in 1942 and 1951. Measurements were also made by E. S. Stewart and J. L. Stewart[36-38] (1946, 1948, and 1952), J. E. Rhodes[39] (1946) and others[27, 40]. These results are shown in Fig. 52.[27]

Theoretical calculations of rotational relaxation times have been made by P. Mariens[41] (1951), Robert Brout[42] (1954), and K. Takayanagi[43-46].
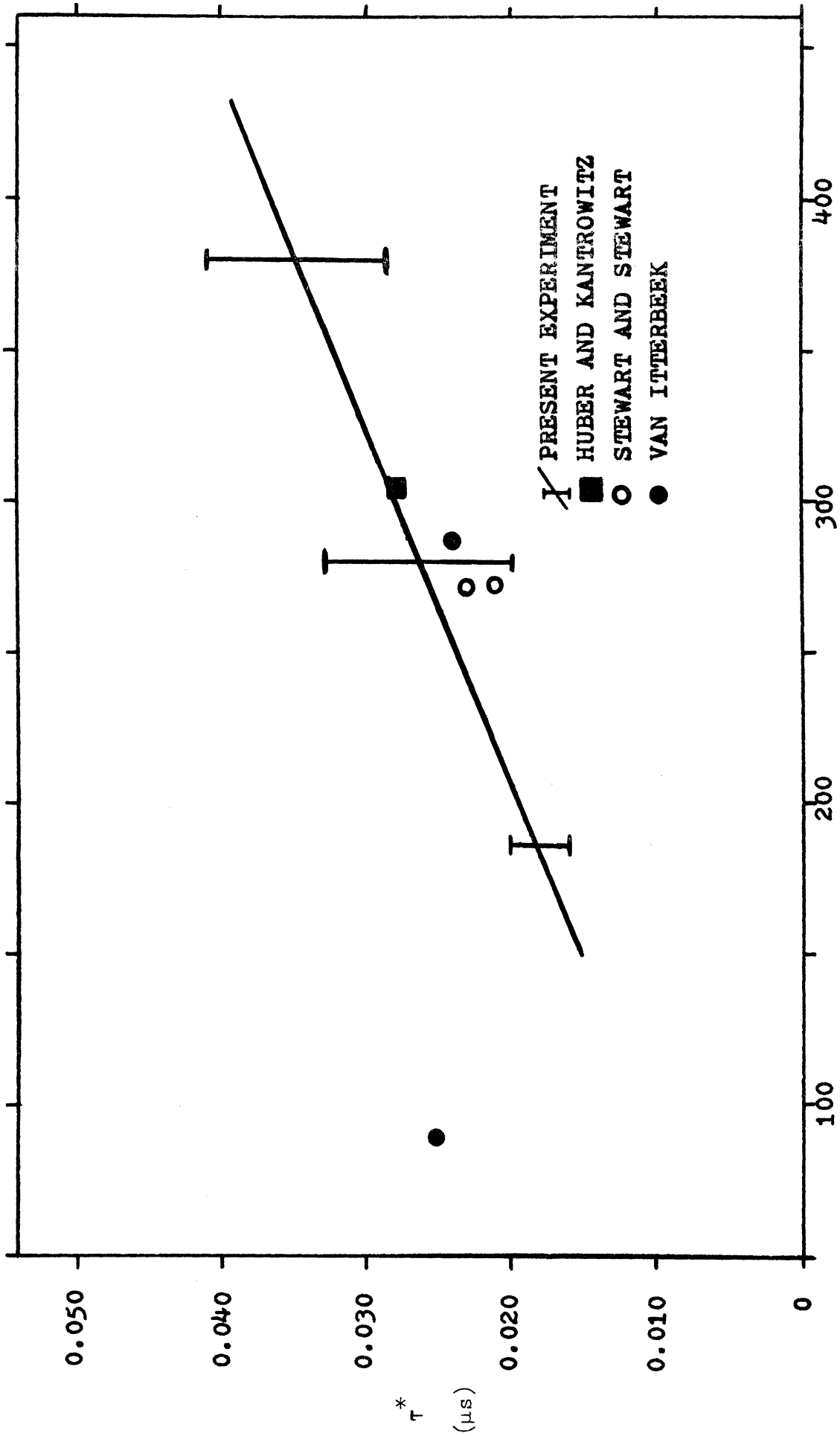
Figure 52. Comparison of mean values of this experiment with other experimental results

4. Conclusions

The asymmetry shown in the shock profiles is due to rotational relaxation phenomena. This is confirmed by the following observations:

(1) The decay of the photomultiplier signal is exponential.

(2) The expected inverse proportionality of relaxation times to pressure is observed.

(3) There is no asymmetry of the shock profiles for neon, argon, or helium.

(4) The measured relaxation times are consistent with those obtained by other methods.

Although the scatter of experimental points is too large to constitute an accurate measurement of relaxation times for higher temperatures, it is believed that the results for temperatures less than $200^\circ K$ are relatively precise. The measurements for higher temperatures are valuable in spite of the scatter of points since they provide a simple and direct confirmation of previous results.

No measurable difference between rotational relaxation times in parahydrogen and normal hydrogen has been observed. This is consistent with previous measurement results and theoretical predictions. There is an appreciable difference of up to 20% in laboratory relaxation times for these two gases due to the differences in their density ratios.

CHAPTER VI

SUGGESTIONS FOR FUTURE EXPERIMENTS

It is hoped that the Rankine-Hugoniot measurements will be extended to deuterium. The same general features are predicted as for hydrogen but at slightly lower temperatures. The curves for normal deuterium and orthodeuterium for $20^{\circ}K$ resemble those for normal hydrogen and parahydrogen at $30^{\circ}K$ initial temperatures.

Extensive rotational relaxation measurements should be carried out for deuterium, where relaxation times similar to those of hydrogen should be observable. This should also be done for hydrogen deuteride. It is interesting to note that no ultrasonic experiments have been carried out for hydrogen deuteride. There is no apparent reason why this has not been done.

If, as the experiment seems to indicate, a major source of error is the diffraction of light from the shock, the use of a white light source in the schlieren system may yield greatly improved experimental results. This should be tried.

Longer laboratory relaxation times can be observed if pressure ratios across the shock are low. For this reason it is believed that if this experiment were carried out with weak shocks at higher initial temperatures of perhaps $150^{\circ}K$, a more accurate determination of the relaxation times

could be made.

Rotational relaxation measurements should be extended to temperatures of perhaps $1000^{\circ}K$ or higher. The shock tube is admirably suited to this type of high temperature measurement. In this manner it would be possible to determine the relaxation times for the higher transitions such as $2 \rightarrow 4$ and $3 \rightarrow 5$. These values are not well known. Experimental and theoretical values are in conflict with each other.[40] The data analysis will be more difficult since hydrogen must then be considered as a three or four energy level gas.

There is a narrow beam laser-schlieren technique developed by Kiefer and Lutz[47] which is more sensitive than the one used in this experiment and avoids the problem of diffracted light from the shock front. Although the spacial resolution within a relaxation region is as good or better than that used in this experiment, it is not possible to work as close to the shock front. It is possible, however, that the increased sensitivity of the method might make up for this disadvantage.

There are a multitude of other experiments that should be performed with the cooled shock tube. Both the viscosity and the thermal conductivity of a gas decrease with decreasing temperature. At $77^{\circ}K$ they will be one third their magnitudes at room temperature. The theories of boundary layer formation and shock curvature can be tested under entirely new initial conditions. Shock thickness studies could also

be made. This should provide a very good check on the theories of these processes. The cooled shock tube has proven to be economical enough in operation to permit this to be done.

Vibrational relaxation measurements of certain gases can be extended to temperatures below $300^{\circ}K$ in the cryogenic shock tube. Some experiments of this nature have already been carried out at Cornell.

A liquid helium cooled shock tube has recently been constructed at the California Institute of Technology for the purpose of generating high mach number flows.[51] This indicates yet another application of the cryogenic shock tube.

REFERENCES

1. Laporte, O., Scientific American, December 1949, pp.14-19.

2. Courant, R. and Frederichs, K. O., Supersonic Flow and Shock Waves, Interscience, New York, 1948.

3. Kim, Y. W., "Ionized Mercury Gas in the Heated Shock Tube: The Measurement of Relaxation Times and Absolute Intensities", Ph. D. Thesis, Univ. of Mich. (1968).

4. Mautz, C. W., Geiger, F. W., and Epstein, H. T., "On the Investigation of Supersonic Flow Patterns by Means of the Shock Tube", Phys. Rev., 74, No. 12, 1872-1873, 1948.

5. Hollyer, Jr., R. N., Hunting, A. C., Laporte O., Schwarcz, E. H., and Turner, E. B., Phys. Rev. 87, 911, (1952).

6. Resler, E. L., Lin, Shao-Chi, and Kantrowitz, A., J. Appl. Phys. 23, 1390 (1952).

7. Penner, S. S., "The Determination of Absolute Intensities and f-Numbers from Shock Tube Studies", Technical Report 5, California Institute of Technology, Jet Propulsion Laboratory (1957).

8. Doherty, L. R. Ph. D. Thesis, Univ. of Mich. (1962).

9. Wilkerson, T. D. Ph. D. Thesis, Univ. of Mich. (1961).

10. Turner, E. B., Ph. D. Thesis, Univ. of Mich. (1956).

11. McLean, E. A. and Ramsden, S. A., Phys. Rev. 140, A1122 (1965).

12. Hill, R. A. and Gerardo, J. B., Phys. Rev. 162, 45 (1967).

13. Stupochenko, Ye. V., Losev, S. A., and Osipov, A. I., Relaxation in Shock Waves, Springer-Verlag, New York(1967).

14. Laporte, O., "High Temperature Shock Waves", Combustion and propulsion, Third AGARD Colloquium, Pergamon Press, New York, (1958).

15. Woolley, H., Scott, R. B., and Brickwedde, F. G.,
National Bureau of Standards, Research Paper RP1932,
Journal of Research of N. B. S., Volume 41, Nov. (1948).

16. Euken, A., Preuss. Akad. d. Wiss., p 141 (1912).

17. Hund, F., Z. f. Physik, Vol. 42, p. 93 (1927).

18. Dennison, D. M., Proc. Roy. Soc. A115, 483 (1927).

19. Lipsett, F. R., Rev. Sci. Inst. 37, 229 (1966).

20. Zipfel, C. L., Ph. D. Thesis, Univ. of Mich. (1969).

21. Hunting, A. C., Ph. D. Thesis, Univ. of Mich. (1961).

22. Wood, G. P., "Interferometer Methods", Part II of
Nelson, W. C., ed., "Optical methods for examining
the flow in high-speed wind tunnels", AGARDograph
No. 23, N.A.T.O. Advisory Group for Aero. Res. and
Dev., Paris (1956).

23. Ladenburg, R. W., et al, editors, Vol. 9 of High Speed
Aerodynamics and Jet Propulsion, Princeton University
Press, Princeton, New Jersey, p 26-46 (1954).

24. Koopman, D. W., Ph. D. Thesis, Univ. of Mich. (1963).

25. Roberts, J. R., Ph. D. Thesis, Univ. of Mich. (1964).

26. American Institute of Physics Handbook, Dwight E. Gray
Coordinating Editor, McGraw-Hill (1957).

27. Herzfeld, K. F. and Litovitz, T. A., Absorption and
Dispersion of Ultrasonic Waves, Academic Press, New
York and London (1959).

28. Hornig, D. F., Phys. Rev. 72, 179 (1947).

29. Greene, E. F. and Hornig, D. F., J. Chem. Phys.,
Vol. 21, No. 4, p 617 (1953).

30. Kantrowitz, A., J. Chem. Phys., Vol. 14, No. 3,
p 150 (1946).

31. Huber, P. W. and Kantrowitz, A., J. Chem. Phys. 15,
275 (1947).

32. Van Itterbeek, A. and Mariens, P., Physica 4, 609 (1937).

33. Van Itterbeek, A. and Thys, L., Physica 5 889 (1938).

34. Van Itterbeek, A. and Vermaelen, R., Physica 9, 345 (1942).

35. Van Itterbeek, A. and Verhaegen, Nature 167 478 (1951).

36. Stewart, E. S., Phys. Rev. 69, 632 (1946).

37. Stewart, J. L. and Stewart, E. S., J. Acoust. Soc. Am. 20, 585 (1948).

38. Stewart, E. S. and Stewart, J. L., J. Acoust. Soc. Am. 24, 194 (1952).

39. Rhodes, J. E., Phys. Rev. 70 91 (1946).

40. Bhatia, A. B., Ultrasonic Absorption, Oxford at the Clarendon Press, Oxford University Press (1967).

41. Mariens, P., Colloquium Over Ultrasonore Trillingen, International Conference on Ultrasonics, Brussels (1951).

42. Brout, R., J. Chem. Phys., Vol. 22, No. 5, p 934-939 (1954).

43. Takayanagi, K., Progr. Theor. Phys. 11, 557 (1954).

44. Takayanagi, K, Proc. Phys. Soc. London A 70 348 (1957).

45. Takayanagi, K, J. Phys. Soc. Japan 14, p 1458-59 (1959).

46. Takayanagi, K., Suppl. Prog. Theor. Phys., No. 25, p. 1 - 99 (1963).

47. Kiefer, J. H. and Lutz, R. W., Proc. 5th Int. Shock Tube Symposium, p. 369 (1965).

48. Shreffler, G. and Christian, R. H., J. Appl. Phys. 25, 324 (1954).

49. Farkas, A., Orthohydrogen, Parahydrogen, and Heavy Hydrogen, Cambridge at the University Press, Cambridge (1335).

50. Laporte, O. and Yoder, M. J., "Low Temperature Shock Waves in Molecular Hydrogen", Eighth International Shock Tube Symposium - - London (1971)

51. Liepmann, H. W., Private Communication